Spectroscopic Line Shapes of Electronic and Vibrational Excitations of Single-Atom and Single-Molecule Junctions

DISSERTATION

zur Erlangung des akademischen Grades
Doctor rerum naturalium (Dr. rer. nat.)

der Fakultät für Mathematik und Naturwissenschaften
der Technischen Universität Ilmenau

vorgelegt von
STEFAN MEIEROTT

Ilmenau 2017

urn:nbn:de:gbv:ilm1-2017000365

Eingereicht am 8. April 2017
Wissenschaftliche Aussprache am 31. August 2017

GUTACHTER

1. Prof. Dr. Jörg Kröger
2. Prof. Dr. Stefan Krischok
3. Prof. Dr. José Ignacio Pascual

Abstract

The Kondo effect and inelastic electron tunneling are important physical effects, that give rise to Fano-like line shapes in the current-voltage characteristics through single adatoms and admolecules. In this work a ultra-high vacuum low-temperature scanning tunneling microscope is optimized to make these features accessible in scanning tunneling spectroscopy. Following this, experiments are conducted.
First, the single-Co Kondo effect on Au(1 1 0) is examined. The amplitude of the peak-like Abrikosov-Suhl resonance is found anisotropically distributed across obliquely adsorbed adatoms. The anisotropic evolution is traced to the varying tip-substrate distance across the adatom.
Additionally, fitting of peaked Fano line-shapes is discussed. Characteristic properties of the Fano asymmetry parameter are extracted from experimental evidence and from simulations. An improved parameterization is suggested in order to reduce the parameter space for nonlinear optimization. An angular representation of the asymmetry parameter gives rise to the estimation of uncertainties using linear error propagation.
Second, inelastic tunneling spectroscopy at C_{60} molecules adsorbed to Pb surfaces is reported. By deliberately functionalizing the tunneling tip with single C_{60} molecules the electronic structure is tuned. Coincidently, vibrational line shapes are affected. The varying electronic structure at different adsorption sites on the Pb(1 1 1) surface affects vibrational line shapes likewise. Thus, a clear-cut correlation between vibrational line shapes and the electronic structure is derived. These findings represent an experimental proof to theoretical predictions about the contribution of resonant processes in inelastic tunneling spectroscopy.
Further, electronic transport through C_{60} on Pb(1 1 1) is examined for varying tip-molecule distance. The signature of the lowest unoccupied molecular orbital is found to shift towards the Fermi energy with decreasing tip-molecule distance. Vibrational line shapes are governed by the relative molecule position inside the junction, rather than the varying electronic structure. These observations stress the importance of the junction symmetry in inelastic electron tunneling.

Kurzfassung

Der Kondo-Effekt und inelastisches Elektronentunneln sind bedeutende Effekte in der Physik des Elektronentransports durch einzelne Atome und Moleküle. In den Ableitungen der Strom-Spannungs-Kennlinie treten charakteristische Fano-artige Linienformen auf. Um solche Signaturen zugänglich zu machen, wird in dieser Arbeit ein Ultrahochvakuum-Tieftemperatur-Rastertunnelmikroskop optimiert.
Anschließend wird der Kondo-Effekt an Co-Atomen auf der Au(1 1 0)-Oberfläche behandelt. Im Spektrum des differentiellen Leitwerts einzelner Co-Atome tritt eine Peak-förmige Signatur der Abrikosov-Suhl-Resonanz auf. An Co-Atomen auf Facettenplätzen der Au(1 1 0)-(1 × 2) rekonstruierten Oberfläche breitet sich diese Resonanz anisotrop aus. Die Anisotropie wird auf Variationen im Spitze-Substrat-Abstand zurückgeführt.
Weiterhin wird die Parameter-Schätzung verrauschter Fano-Linienformen anhand experimenteller und simulierter Daten diskutiert. Zur Linienanpassung nach der Methode der kleinsten Quadrate wird die Verwendung einer günstigeren Parameterisierung der Fano-Funktion nahegelegt. Zusätzlich ermöglicht eine Winkeldarstellung des Asymmetrie-Parameters die Schätzung der Unsicherheit nach Gauß'scher Fehlerfortpflanzung.
Der darauf folgende Teil der Arbeit widmet sich Tunnelspektren von C_{60}-Molekülen auf Pb-Oberflächen. Mittels gezielter Funktionalisierung der Tunnelspitze mit einzelnen C_{60}-Molekülen wird die elektronische Struktur eingestellt. Gleichzeitig ändern sich die Linienformen von Vibrationssignaturen. Ähnlichen Einfluss auf die Linienformen hat die elektronische Struktur unterschiedlich adsorbierter Moleküle auf der Pb(1 1 1) Oberfläche. Ein quantitativer Zusammenhang zwischen elektronischer Struktur und Vibrationssignaturen wird ermittelt. Die Ergebnisse sind ein experimenteller Nachweis theoretischer Vorhersagen zu resonanten Tunnelprozessen in inelastischem Elektronentunneln.
Im Anschluss wird der elektronische Transport abhängig vom Probe-Spitze-Abstand untersucht. Bei Annäherung der Tunnelspitze verschiebt die Signatur des niedrigsten unbesetzten Molekülorbitals zu niedrigeren Energien. Vibrationssignaturen werden vor allem durch die relative Position des Moleküls zwischen den Elektroden bestimmt. Diese Beobachtungen untermauern die Bedeutung der Kontaktsymmetrie beim inelastischen Elektronentunneln.

CONTENTS

1 INTRODUCTION

THE advent of the scanning tunneling microscope (STM) gave a fresh impetus to solid state physics, which lasts to the present day [1]. In fact, surface science is inconceivable without this remarkable technique. In the broad range of modern characterization methods, like photoemission spectroscopy [2], infrared and Raman spectroscopy [3], or electron energy loss spectroscopy [4, 5], the STM stands out for imaging direct space with atomic resolution and spectroscopy with μeV energy resolution. It thus offers the unique chance to examine the electronic properties of single atoms and single molecules. Measurements may be carried out in a vast electrical conductance range. Current I and the voltage V across the tunneling junction can be controlled over several orders of magnitude, down to pA and μV. Moreover, atomic manipulation techniques deepen the understanding of the involved physics.

An extremely well optimized microscope extends the scope of the STM by far. Achieving great stability of the junction geometry permits access to faint signatures of exciting physical effects, like inelastic electron tunneling (IET). Additionally, the operation at very low temperatures increases energy resolution and gives rise to a broad range of physics, containing superconductivity [6], Majorana fermions [7], skyrmions [8], the Tomonaga-Luttinger liquid [9], or the Kondo effect in nanostructures [10, 11].

This work focuses on two physical phenomena: the single-atom Kondo effect and inelastic electron tunneling. In scanning tunneling spectroscopy these effects give rise to characteristic line shapes, including dip-like, peak-like, and asymmetric signatures.

The Kondo effect is one of the most important correlation effects in solid state physics. Conduction electrons of a non-magnetic metal host scatter at magnetic impurities, which

leads to the formation of a characteristic Kondo resonance at the Fermi level [12]. In a tunneling experiment at magnetic adsorbates this resonance manifests itself as a Fano function in the differential conductance spectrum. Single Co adatoms at noble metal surfaces are well studied adsorbates. On most surfaces dip-like [13–15] or asymmetric [13, 16] line shapes have been reported, while on few systems a peak was found [17–19]. All of these surfaces are either flat or show some long-range corrugations from reconstructions. Few reports mention anisotropic spatial variations of the amplitude of the Kondo feature [20, 21], which were led back to the electronic structure of the surface. However, a detailed analysis of the spatial evolution of the Kondo amplitude on a strongly reconstructed surface is missing so far. Besides electronic effects, the tip-substrate distance was theoretically predicted to affect the evolution of the resonance amplitude in the differential conductance $\mathrm{d}I/\mathrm{d}V$ [22]. Corresponding topographic effects can be expected in tunneling experiments, since the tip-substrate distance varies across an adsorbate at constant feedback loop parameters.

The increasing number of reported peak-like Kondo features [17–19] urges questions about their analysis. Estimating uncertainties for the asymmetry parameter q is specifically challenging for peaks. While a dip implies $q = 0$, a peak can correspond to either $q = +\infty$ or $q = -\infty$. Given the inevitable scattering of experimental data peaks are connected with large and strongly asymmetric uncertainty margins of the asymmetry parameter. Moreover, fitting with the conventional parameterization of the Fano function depends on the chosen set of initially guessed parameters. The required nonlinear optimization in a three-dimensional parameter space makes it difficult to judge the uniqueness of fit results. A thorough discussion of peaked Fano line shapes is vital to understand and to overcome these obstacles.

Fano-like line shapes are also found in inelastic electron tunneling spectroscopy (IETS) of single molecules. The corresponding structures in $\mathrm{d}^2I/\mathrm{d}V^2$ spectra can be reduced to interactions of electrons with molecular vibrations of energy $\hbar\omega$. Inelastic scattering opens

an additional conduction channel, which gives rise to the formation of peaks at positive voltages. However, higher order scattering processes result in more complex features. The exact line shape depends on the electronic properties of the system [23]. At energetic proximity between vibrational energies and a molecular resonance (on-resonant regime) dip-like and asymmetric features are expected. C_{60} molecules adsorbed to the Pb(1 1 1) surface constitute a promising system to observe these effects. At many C_{60}-metal systems few vibrational modes were reported [24, 25]. However, for C_{60} on Pb(1 1 1) features of all H_g modes were found [24, 26]. Additionally, the lowest unoccupied molecular orbital (LUMO) is partially filled, thus lies energetically close to C_{60} vibrational energies [26, 27]. Moreover, the LUMO energy varies depending on the adsorption position [27].
To examine the potential impact of the tuneling tip on vibrational features STM manipulation techniques offer an appealing option. Deliberate manipulation of C_{60} molecules has been demonstrated previously [28, 29]. Accordingly, C_{60} on Pb(1 1 1) is the ideal candidate for examining the impact of molecular resonances on the shape of vibrational features.

Most IETS experiments are carried out in a single electron transport regime. A wealth of molecule-surface systems has been studied in tunneling [30–36] or in contact regime [37–39]. The transition between both conductance regimes has been investigated scarcely [26, 40, 41]. For C_{60} on Pb(1 1 1) off-resonant IET data was published previously in contact as well as in tunneling regime [26]. However, for on-resonant vibrational features experimental evidence has been missing to date. Line shapes may be affected by the probable LUMO shift towards the Fermi level, which was observed previously for C_{60} on Cu(1 1 1) [42]. However, for a molecule centered between the leads theories predict solely peaks at positive voltages [43, 44]. Thus, exciting effects can be expected in the crossover between tunneling and contact regime.

Despite considerable previous work about the Kondo effect and IETS, several characteristics remain uncovered prior to this work. The following questions will be discussed in the present thesis:

(I) How does the Kondo amplitude evolve on a strongly corrugated surface?

(II) Is there a better way to estimate the line shape parameter of peaked Fano curves?

(III) Can C_{60} vibrational line shapes be tuned by electronic properties?

(IV) How does the geometry of the tunneling junction affect C_{60} vibrational features?

In order to clarify these questions experiments with an ultra-high vacuum low-temperature scanning tunneling microscope (UHV-LT-STM) were performed. The results are presented in the following.

Chapter 2 briefly describes the experimental principles, and the methods used for sample preparation. In **Chapter 3** structural improvements of an existing UHV-LT-STM are presented. Signal quality was significantly increased while keeping the base temperature very low. These characteristics enable experiments targeting exciting physical phenomena, like the Kondo effect at single atoms and inelastic tunneling spectroscopy.

Chapter 4 discusses the spectroscopic manifestation of the Kondo effect at single Co adatoms on the Au(1 1 0) surface. Contrary to most reports about Co adatoms on noble metal surfaces [13, 14, 16] a peak-like feature is found at zero voltage. Moreover, the amplitude is distributed anisotropically across the adatom, which is explained by a topographic effect.

Chapter 5 analyzes fitting of the highly symmetric peak-like line shapes atop Co adatoms on Au(1 1 0). An improved parameterization is chosen, which enables optimization in a reduced parameter space. The presence of a global minimum in the sum of squared residuals and thus the independence of start parameters may conveniently be identified in a two-dimensional plot. Further, an angular representation of the Fano parameter is suggested, which enables linear error propagation and reliable determination of uncertainty margins.

Chapter 6 addresses inelastic electron tunneling at single C_{60} molecules. Molecules adsorbed to the Pb(1 1 1) surface as well as C_{60}-functionalized tunneling tips are studied. The respective other electrode was a bare Pb surface. Depending on the overlap of orbital and vibrational spectral ranges different spectroscopic line shapes of molecular vibrational

quanta are observed. By adsorbing molecules to the tip in different adsorption configurations the energy range covered by the LUMO resonance is tuned. Concomitantly, the line shapes of different vibrational modes are affected. The reported observations represent an experimental proof to theoretical predictions on the contribution from resonant processes to inelastic electron tunneling.

Chapter 7 elaborates remaining questions of C_{60} vibrational features on Pb(1 1 1). The connection between the electronic structure and vibrational features in IETS is substantiated at differently adsorbed molecules on the Pb(1 1 1) surface. Decreasing the tip-surface distance removes the dependence of IET features on energetic properties. When contact between the leads is formed, all observable signatures are measured as peaks. The observed behavior is led back to the relative molecule position inside the junction.

With these examinations the thesis intends to contribute to a better understanding of the Kondo effect at single atoms, and of the physics of inelastic electron tunneling. Maybe, this work even excites curiosity about topographic effects in Kondo physics, awakes enthusiasm for archetypal IETS model systems, or helps others analyzing their data.

2 Principles and Preparation

THE STM combines a variety of appealing properties, which can be used for characterization of structures at the nanoscale. High spatial and energy resolution give insights into the physics of single atoms and single molecules. Mapping significant physical parameters, like the density of electronic states, provides access to their spatial propagation. Moreover, manipulation techniques extend the scope of the instrument. The most important aspects of the STM are presented in this section, with a focus on the topic of this thesis. Following this, methods of sample preparation are described.

2.1 Scanning Tunneling Microscopy

The STM is based on the quantum mechanical tunneling effect. An electrical current I is measured, which flows across a nanometer-sized tunneling junction. The junction is formed between a sharp needle (the tip) and a sample of interest. Figure 2.1 shows a sketch of an elastic tunneling process, that contributes to the tunneling current. An electron may travel across the insulating vacuum barrier between sample and tip because of its considerable probability of presence at the other side. When a voltage V is applied[1] across the barrier the electric potential can be modeled with a trapezoidal shape [45–47]. Coincidently, Fermi energies of sample $E_{\mathrm{F,s}}$ and tip $E_{\mathrm{F,t}}$ are energetically shifted against each other. Electrons from occupied states at the electrode with higher Fermi energy gain access to empty states at the other side. The tunneling current scales with the amount of accessible initial (initially occupied) and final (initially empty) states. It may be expressed

[1] Throughout this work the bias voltage is applied to the sample, *i.e.* the tip is connected to the ground. For convenience, zero energy is set to the Fermi energy of the sample.

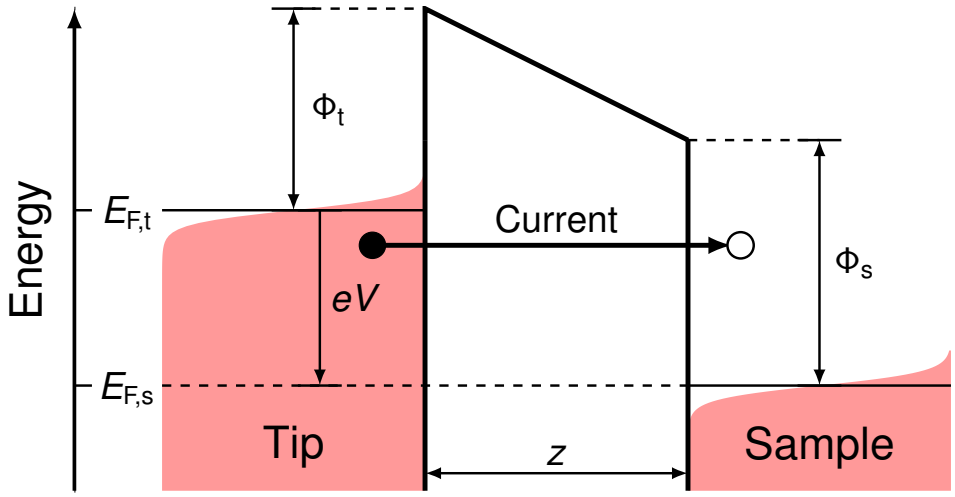

Figure 2.1 Sketch of an elastic tunneling process as applied in a STM at finite temperatures. Tip (left electrode) and sample (right electrode) are separated by a distance z. The work functions of tip (Φ_t) and sample (Φ_s) define the height of the vacuum insulating barrier. Electrons reside in occupied states (red shaded areas) mostly below the Fermi energies of the tip ($E_{F,t}$) and the sample ($E_{F,s}$). The applied bias voltage eV shifts the Fermi energies against each other. An electron in the tip (black dot) may tunnel through the vacuum barrier into an empty state (white dot) of the sample. Initial and final state exhibit the same energy. The tunneling current results from many similar events.

as [48]

$$I = \frac{4\pi e}{\hbar} \int_{-\infty}^{\infty} \rho_s(E)\rho_t(E-eV)\mathscr{T}(E,V,z)[\mathrm{f}(E-eV,T)-\mathrm{f}(E,T)]\,dE. \tag{2.1}$$

Here, ρ_t and ρ_s are the local densities of states of the tip and the sample, respectively. $\hbar$ is Planck's constant divided by 2π and e is the elementary charge. $\mathrm{f}(E) = [1+\exp(\beta(E-E_F))]^{-1}$ denotes the Fermi function, which is dependent on the temperature T through $\beta = (k_\mathrm{B}T)^{-1}$ (k_B: Boltzmann constant). The transmission factor $\mathscr{T}$ describes the decay of the evanescent electron waves into the vacuum. Since $\mathscr{T}$ is exponentially dependent on the tip-sample separation z (see below) the STM offers high vertical resolution. This fact can be used for the acquisition of topographic maps. The tip scans laterally across the surface, driven by a picometer-precise piezo actuator. Simultaneously, the vertical position is controlled using a feedback loop, which keeps the current constant. The vertical displacement of the tip is monitored as a function of the lateral position. The resulting

map combines topographic and electronic properties of the surface, because z (through $\mathscr{T}$) as well as ρ_s enter the expression for the current.
Electronic properties can be explicitly addressed in recordings of the derivative of the current [Eq. (2.1)] with respect to the bias voltage. $\mathrm{d}I/\mathrm{d}V$ is approximately proportional to ρ_s at the position of the tunneling tip,

$$\frac{\mathrm{d}I}{\mathrm{d}V} \propto \rho_s(eV), \tag{2.2}$$

assuming constant ρ_t, zero temperature and energy independent transmission factor The derivatives of the current are readily measured using a lock-in amplifier. A sinusoidal signal with amplitude V_{mod} and frequency f_{mod} is added to the bias voltage. The lock-in amplifier multiplies the current response by the modulation signal. After passing the result through a low-pass filter a voltage proportional to optionally $\mathrm{d}I/\mathrm{d}V$ or $\mathrm{d}^2I/\mathrm{d}V^2$ is extracted. With this technique high-resolution spectra of ρ_s can be acquired. The bias voltage is sweeped through a desired voltage range, while recording $\mathrm{d}I/\mathrm{d}V$. To ensure constant tip-sample height the feedback loop is deactivated.

Transmission Factor

The transmission factor in a trapezoidal tunneling barrier is given by the Wentzel-Kramers-Brillouin approximation [49]

$$\mathscr{T}(E,V,z) = \exp\left(-2z\sqrt{\frac{m_{\mathrm{e}}}{\hbar^2}\left(\Phi_{\mathrm{s}} + \Phi_{\mathrm{t}} + eV - 2E\right)}\right) \tag{2.3}$$

where m_{e} is the electron mass. For small tunneling voltages the work functions of the sample and the tip exceed eV by far. In this case eV is neglected and the transmission factor can be approximately treated as energy independent. Moreover, an averaged work function may be used, given by $\Phi = (\Phi_{\mathrm{t}} + \Phi_{\mathrm{s}})/2$. The transmission factor can then be

expressed as

$$\mathscr{T}(z) = \exp\left(-\frac{2z}{\lambda}\right), \tag{2.4}$$

where $\lambda = \hbar/\sqrt{2m_e\Phi}$ is the decay length of electron states at the Fermi level. For typical metal work functions around 4–5 eV the decay length yields $\lambda \approx 0.9\,\text{Å}$. In more complex systems, tunneling electrons may stem from different kinds of electronic states. Here, the transmission factor of conduction electrons may be explicitly expressed in terms of a tip-substrate coupling parameter t_c, where $\mathscr{T} = {t_c}^2$ [22]. Tunneling into more closely bound orbitals yields lower decay lengths, *e.g* into a Co adatom adsorbed to a noble metal surface $\lambda_{\text{Co}} \approx 0.75\,\text{Å}$ [22].

Inelastic Electron tunneling

Interactions of electrons with molecular vibrations can give rise to features in the current-voltage curve. Figure 2.2(a) shows the sketch of a possible scenario. An incident electron loses energy to a molecular vibration quantum. Since energies of the initial and final electronic state differ, the transmission is called inelastic tunneling. As follows from the Pauli principle, these processes predominantly occur for $|eV|$ exceeding the energy of the excited quantum $\hbar\omega$. At this energy the amount of accessible final states increases abruptly. Therefore, the current-voltage curve shows sudden slope variations at $V = \pm\hbar\omega/e$ [Fig. 2.2(b)], which is equivalent to step-like increases in the differential conductance spectrum [Fig. 2.2(c)]. Accordingly, in $\mathrm{d}^2I/\mathrm{d}V^2$ a dip is found at $V = -\hbar\omega/e$ and a peak is present at $V = +\hbar\omega/e$ [Fig. 2.2(d)].

However, a vibrational quantum can be re-absorbed [Fig. 2.3(a)]. In this case the initial and the final electronic state exhibit the same energies. Accordingly, these processes contribute to the elastic channel. Interference [43] with the regular elastic channel [Fig. 2.1] leads to more complex structure in the current-voltage curve [Fig. 2.3(b)]. The corresponding differential conductance spectrum [Fig. 2.3(c)] shows step-like decreases and logarithmic singularities at $V = \pm\hbar\omega/e$. Accordingly, dip-like (peak-like) to asymmetric

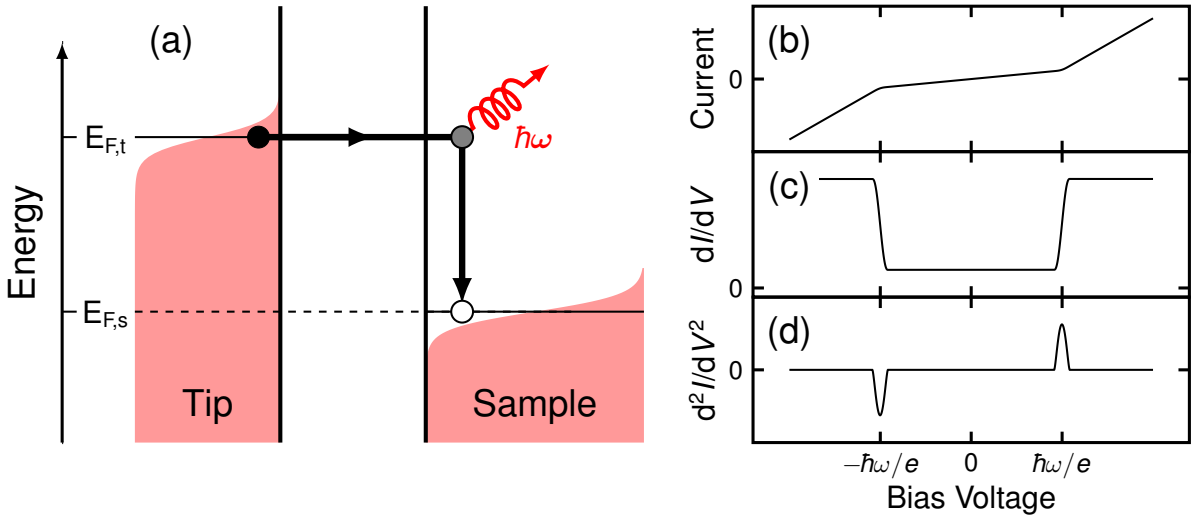

Figure 2.2 (a) Sketch of an inelastic tunneling process. An incident electron (black dot) at the Fermi level of the tip tunnels into empty states of the sample. By exiting a vibrational quantum $\hbar\omega$ (curled arrow) the electron is transferred to an unoccupied state at the Fermi level of the sample (white dot). The intermediate state is shown as gray dot. **(b)** Exemplary current-voltage curve involving the process shown in (a). **(c)** Corresponding dI/dV and **(d)** d^2I/dV^2 spectra. Characteristic features emerge at $V = \pm\hbar\omega/e$. Broadening mechanisms are considered.

features are present in the d^2I/dV^2 spectrum at $V = \pm\hbar\omega/e$ [Fig. 2.3(d)]. The mechanisms controlling the probability of the discussed processes depend on the energetic and structural properties of the junction. To analyze vibrational features in practice d^2I/dV^2 spectra are acquired and normalized with the corresponding dI/dV spectrum.

Broadening Mechanisms

Features in tunneling spectra are essentially broadened by temperature, lock-in modulation, and fluctuations of the bias voltage. To simulate a measured spectrum S a spectrum S_{theory} is considered, assuming zero temperature and perfectly clean bias voltage free from modulation and external disturbances. S_{theory} may be a model for the local density of states, or may describe spectral manifestations of vibration-mediated electron transitions. Next, convolution of the S_{theory} with characteristic broadening functions for thermal broadening χ_{therm}, modulation broadening χ_{mod} and optionally fluctuation broadening χ_{fluc} is

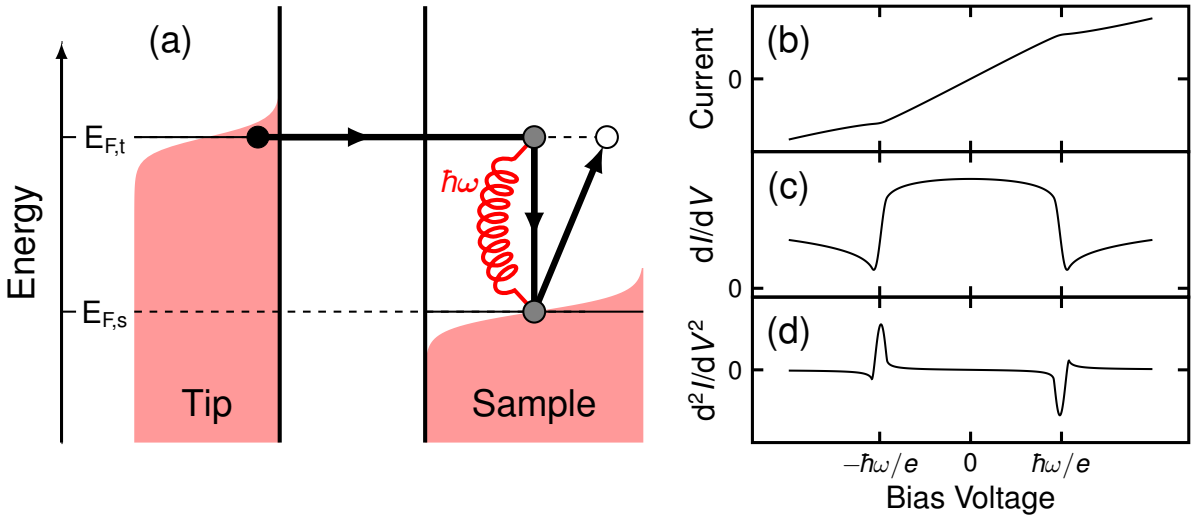

Figure 2.3 (a) Sketch of an elastic tunneling process involving the emission and reabsorption of a vibrational quantum $\hbar\omega$. An electron at the tip (black dot) tunnels into unoccupied states of the sample. A vibrational quantum (red curl) is emitted and reabsorbed. Initial and final state (white dot) exhibit the same energy. Intermediate states are shown as gray dots. **(b)** Exemplary current-voltage curve including processes shown in (a). **(c)** Corresponding $\mathrm{d}I/\mathrm{d}V$ and **(d)** $\mathrm{d}^2I/\mathrm{d}V^2$ spectra. Broadening mechanisms are considered.

performed:

$$S = S_{\mathrm{theory}} * \chi_{\mathrm{therm}} * \chi_{\mathrm{mod}} * \chi_{\mathrm{fluc}}. \tag{2.5}$$

The appropriate broadening functions are chosen according to the number of derivatives applied to the current ($\mathrm{d}I/\mathrm{d}V$ or $\mathrm{d}^2I/\mathrm{d}V^2$), and to the modeled spectroscopic features.
Thermal broadening results from the Fermi-Dirac statistics of the occupation of electron states. Occupied states are smeared about the Fermi energies, which is considered in Figs. 2.1, 2.2(a), and 2.3(a). $\mathrm{d}I/\mathrm{d}V$ spectra from simple elastic tunneling [Fig. 2.1] are given by the derivative of Eq. (2.1) with respect to the voltage. Assuming constant density of states of the tip the result yields a convolution of ρ_s with the derivative of the Fermi function $\chi_{\mathrm{therm},1}$.
Inelastic features are broadened according to the occupation statistics at both electrodes [50]. For example, the electronic transition shown in Fig. 2.2(a) comprises tip states at $E_{\mathrm{f,t}}$

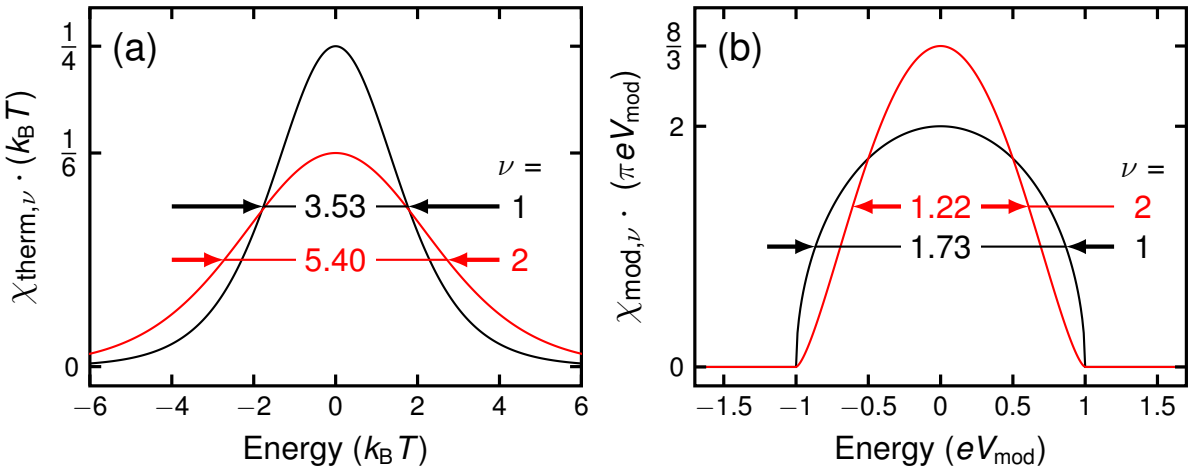

Figure 2.4 (a) Thermal broadening functions $\chi_{\mathrm{therm},\nu}$ for $\mathrm{d}I/\mathrm{d}V$ spectra ($\nu = 1$, black curve) and for vibrational features in $\mathrm{d}^2I/\mathrm{d}V^2$ spectra ($\nu = 2$, red curve) . Full width at half maximum values are given for each curve. **(b)** Lock-in broadening functions $\chi_{\mathrm{mod},\nu}$ for $\mathrm{d}I/\mathrm{d}V$ spectra ($\nu = 1$, black curve) and for $\mathrm{d}^2I/\mathrm{d}V^2$ spectra ($\nu = 2$, red curve)

and sample states at $E_{\mathrm{f,s}}$. In the proximity of these energies similar transitions can occur at finite temperatures. The onset of inelastic tunneling is thus smeared about $V = \hbar\omega/e$ [51, 52].

The broadening functions $\chi_{\mathrm{therm},\nu}$ for $\mathrm{d}I/\mathrm{d}V$ spectra ($\nu = 1$) from simple elastic processes [Fig. 2.1] and for vibrational features in $\mathrm{d}^2I/\mathrm{d}V^2$ spectra ($\nu = 2$) [Figs. 2.2, 2.3] are given by[2] [48, 51, 52]

$$\chi_{\mathrm{therm},1}(E) = \frac{\beta}{4}\cosh^{-2}\left(\frac{\beta E}{2}\right) \tag{2.6}$$

$$\chi_{\mathrm{therm},2}(E) = \beta\exp(\beta E)\cdot\frac{\beta E + 2 + (\beta E - 2)\exp(\beta E)}{(\exp(\beta E) - 1)^3} \tag{2.7}$$

Making use of the lock-in technique is accompanied with modulating the bias voltage. Usually, a sinusoidal signal with an amplitude V_{mod} is added to V. Accordingly, the lock-in

[2] On superconducting substrates slightly differing vibrational line shapes were observed, and were explained with a more complicated model [52]. However, due to the marginal impact of this effect, strong modulation broadening, and for convenience, this work exclusively uses Eq. (2.7) to model vibrational line shapes.

response probes the natural spectrum in the energy range $eV \pm eV_{\mathrm{mod}}$. The corresponding broadening functions $\chi_{\mathrm{mod},\nu}$ for first ($\nu = 1$) and second ($\nu = 2$) derivative spectra read [52]

$$\chi_{\mathrm{mod},1}(E) = \mathrm{Re}\left(\frac{2}{\pi e V_{\mathrm{mod}}} \frac{\sqrt{eV_{\mathrm{mod}}^2 - E^2}}{eV_{\mathrm{mod}}} \right) \tag{2.8}$$

$$\chi_{\mathrm{mod},2}(E) = \mathrm{Re}\left(\frac{8}{3\pi e V_{\mathrm{mod}}} \left(\frac{\sqrt{eV_{\mathrm{mod}}^2 - E^2}}{eV_{\mathrm{mod}}} \right)^3 \right) \tag{2.9}$$

Plots of the functions $\chi_{\mathrm{mod},\nu}$ and $\chi_{\mathrm{therm},\nu}$ are shown in Figs. 2.4(a),(b).

The third mechanism contributing to the measured line width stems from random electrical disturbances of the bias voltage. The broadening function for $\mathrm{d}I/\mathrm{d}V$ spectra can be assumed as a normalized Gaussian function with a standard deviation of the root mean square of the bias voltage fluctuations σ_{V} [53]. The effect of voltage noise is indistinguishable from temperature broadening in I-V-characteristics. Thus, an effective temperature of the instrument may be defined as $T_{\mathrm{eff}} = \sqrt{T^2 + 3(e\sigma_{\mathrm{V}}/(k_{\mathrm{B}}\pi)^2}$ [53]. In an excellently optimized instrument this type of broadening can be neglected for most experiments. However, in spectra of the superconducting gap fluctuation broadening may be considered.

Manipulation

Using the apex of the tunneling tip an STM offers the possibility to manipulate structures at a nanometer scale. Manipulation techniques have been used previously in a wide range of applications, which include building chains of single adatoms [54], modification of the chemical structure of an adsorbed molecule [55], and functionalizing the STM tip apex with molecules [28]. Two distinct manipulation techniques can be distinguished: lateral and vertical manipulation.

In lateral manipulation an adsorbate is moved parallel to the surface. The relevant forces, that cause adsorbate movement, originate in the strong electric field (field-assisted diffu-

sion) and in the chemical binding force (sliding process) between the tip and the adsorbate [56]. Field-assisted diffusion can often be used in tunneling regime. Dependent on dipole moment and polarizability of the adsorbate the inhomogeneous electric field may cause a potential energy gradient. The potential energy gradient causes the adsorbate to move towards the minimum of the local energy landscape. Application of the sliding process requires a closer tip-adsorbate distance. Here, the tip is first positioned atop the adsorbate, then it is moved towards the surface to form a partial chemical bond with the adsorbate. The tip is subsequently moved across the surface to the requested place. Finally, the tip is brought back to a larger tip-sample distance. Ideally, the adatom is left adsorbed to the surface, below the tip [56].

Vertical manipulation processes include transfer-on-contact, field evaporation and electromigration. For transfer-on-contact the tip is pushed into chemical contact with the adsorbate. In this case similar binding energies to the surface and to the tip may be present. Upon increasing the tip-sample distance the adsorbate can be left adsorbed to the tip, depending on the electronic and geometric structure of the sample and the tip. The other vertical manipulation techniques rely on the application of voltage pulses (field evaporation) and the flow of electrical current between the electrodes (electromigration) [56].

The Kondo Effect

In pure metals decreasing temperature is usually connected with decreasing resistivity, since electrons may travel through the less-vibrating crystal more easily. Some metals, like Pb, even exhibit zero resistivity below a critical temperature, as superconductivity evolves. In noble metals a finite minimum resistivity is found at zero temperature due to inevitable defects and embedded impurities [57]. However, when magnetic impurities, such as Co, are diluted in a non-magnetic metal host resistivity was found to exhibit a minimum at a characteristic finite temperature T_K [58]. This is the macroscopic manifestation of the Kondo effect. The reason of this transport anomaly was traced to the impact of spin flip scattering of conduction electrons with the impurities [59]. A simple model may illustrate the spin flip mechanism at a single impurity [60]. A single orbital state is assumed that

can be empty, or filled with one or two electrons. In the ground state the level is occupied by one electron, well below the Fermi level. Adding a second electron raises the orbital energy well above the Fermi level due to the Coulomb repulsion. Real processes, that add a conduction electron or empty the level into the Fermi sea, are thus highly unlikely. However, virtual processes may provide such excitations, according to the energy-time uncertainty principle. Consequently, the initial energy state is restored after a very short time. In a spin degenerate system the electron spins (and the impurity spin) may have flipped after the process [12]. Concomitantly, the local density of states (LDOS) is modified [61]. Very close to the Fermi energy a new ground state is formed, which is called the Abrikosov-Suhl or Kondo resonance [61–64]. The emerging state may be conveniently studied at magnetic adsorbates with a scanning tunneling microscope. The STM is an ideal tool, since it combines extraordinarily high energy resolution with picometer-precise spatial resolution. Furthermore, the differential conductance is approximately proportional to the LDOS [Eq. (2.2)]. The LDOS correction due to the presence of the impurity is described by [12, 22, 61]

$$\rho_s(E) \propto \frac{(q+\varepsilon)^2}{1+\varepsilon^2} \tag{2.10}$$

where $\varepsilon = (E - E_0)/\Gamma$. E_0 characterizes the energy of the resonance. Γ measures half-width at half-maximum and accounts for the average spin flip time $\tau = h/\Gamma$, where h is Planck's constant [61]. Moreover, it connects the locally observed resonance with the macroscopic Kondo temperature through $k_B T_K = \Gamma$ [12]. The asymmetry parameter q describes the line shape of the resonance. For $q = 0$ a dip is present, while $q = \pm\infty$ corresponds to a peak. Asymmetric line shapes are obtained for $q = \pm 1$. Very close to the impurity the line shape is determined by the interference of tunneling electrons paths [22]. Three different possible paths can be distinguished. First, electrons travel into the unperturbed substrate states beneath the adsorbate. Second, electrons may tunnel into substrate states, travel through the surface and finally hop into the adsorbate. And third, electrons travel directly into the electronic levels of the impurity. The exact line shape is challenging to predict since the whole electronic structure of the surface as well as hybridization terms enter the

description of q [22].

The amplitude of the Fano curve $A \propto 1+q^2$ describes the spatial extent of the perturbation of the metal electron states due to the presence of the adatom. The present thesis focuses on the line shape and amplitude obtained at single Co atoms. Kondo physics has excellently been reviewed in, *e.g.*, Refs. [12, 57].

Electronic and Vibrational Properties of C_{60} molecules

Buckminsterfullerene C_{60} is a hollow, pseudospherical carbon allotrope. The molecule is know to be extremely stable [65], very stiff [29, 66] and highly polarizable [67]. In alkali intercalated bulk C_{60} superconductivity was observed at low temperatures [68, 69]. The reason was traced to interactions between conduction electrons in C_{60} orbitals and intra-molecular Jahn-Teller type vibrations [70]. Vibrational energies lie below 200 meV and are well studied by infrared [71–73] and Raman spectroscopy [71, 74, 75], photoemission spectroscopy [76], neutron inelastic scattering [77], energy electron loss spectroscopy [78], and inelastic tunneling spectroscopy [26, 79, 80]. The adsorption onto a metal surface has almost no effect on the vibrational modes and the shape of the molecular orbitals [24, 74]. The lowest unoccupied orbital (LUMO) is localized at the C-pentagons of the C_{60} cage. The rotational orientation of the molecule can therefore readily be inferred from topographic images of an admolecule [81]. Electronic level energies differ depending on the reactivity of the surface [81]. On Pb(1 1 1) the LUMO is found just above the Fermi level [27], close to the energy range of the vibrational modes. Interestingly, this energetic proximity enhances vibrational feature intensities in IETS [26]. The present work makes contact with these findings and gives further insight in effects arising from electron-vibration coupling.

2.2 Sample Preparation

Experiments were carried out using Au(1 1 0) and Pb(1 1 1) single crystals. The hat-shaped cut and mechanically polished samples were ordered[3] with an orientation accuracy of 0.4°, a roughness depth of 30 nm and a purity of 99,999%. Immediately after receipt each sample was fixed onto a sample holder and inserted into the vacuum chamber.

Cleaning of Metal Surfaces

Samples were moved to a home-built manipulator prior to cleaning. Samples were cleaned by repeated cycles of Ar^+ bombardment and annealing. High purity (99,999%) Ar gas[4] was ionized by Penning discharge [82] in an ion source (ISE 5, Omicron). The charged ions were accelerated using a voltage of 1.2 kV. By setting the partial pressure to $\approx 3 \cdot 10^{-4}$ Pa the sample current was kept at $\approx$ 15 µA for approximately 15 min. Subsequently, the sample was annealed with an adjacent filament for about 15 min to restore the surface order. During annealing the sample temperature was kept at ≈700 K (Au(1 1 0)) or ≈550 K (Pb(1 1 1)). Temperatures below the melting point of Pb were ensured by previous calibration of the filament current with a Pb wire attached to a sample holder. After $5-10$ sputtering and annealing cycles a sample was transferred to the STM for characterization. Well cleaned samples were identified by few defects and large terraces. Onto such samples single atoms and molecules were deposited.

Single Atom Deposition

Before depositing single Co atoms the sample was cleaned and transferred into the STM. The sample rested, until the base temperature of $\approx$ 6 K was reached. A Co rod[5] was heated by electron impact in an electron beam evaporator (EFM 3, Omicron). Electrons were emitted from a hot filament and accelerated by a voltage of 800 V. A built-in ammeter was used to monitor the flux of ionized Co atoms. The flux was controlled by variation of the

[3] MatecK GmbH, Im Langenbroich 20, D-52428 Juelich
[4] Air Liquide Deutschland GmbH, Hans-Günther-Sohl-Strasse 5, D-40235 Düsseldorf
[5] MatecK GmbH, Im Langenbroich 20, D-52428 Juelich, diameter 2 mm, purity 99.99%

filament current, and by the distance between the filament and the Co rod. The Co rod had been thoroughly degassed to reduce the amount of concomitantly adsorbed hydrogen [83, 84]. After achieving a stable flux of 10 nA, the shutter of the evaporator was opened. The gaseous Co was directed onto the sample through openings in the radiation shields of the cryostat. The openings and the sample were aligned by finely tuning the STM position through screws at the vibration damping system at the cryostat top. During evaporation the flux of ionized Co atoms arriving at the sample was monitored with a transimpedance amplifier, attached to the bias voltage input. The sample temperature rose to $\approx 8\,\mathrm{K}$. After deposition for $\approx 120\,\mathrm{s}$ the shutter and the shield openings were closed. The sample was left to rest and to cool down until the base temperature was reached. Subsequently, the prepared sample was characterized in the STM.

Molecule Deposition

C_{60} molecules[6] were evaporated using a home-built evaporator. The evaporator is composed of a Ta crucible and a commercially available resistively heated UHV button heater[7]. Prior to molecule evaporation the empty heater was extensively degassed for several minutes with a current of 2.4 A, which is equivalent to a temperature of $\approx$ 1200K. After reestablishing room temperature the evaporator was brought out of the vacuum chamber and the Ta crucible was filled with C_{60} molecules. After re-inserting the evaporator into UHV the molecules were degassed at a current of 1 A, *i.e.* $\approx 500\,\mathrm{K}$, for 12 h. Prior to deposition of C_{60} molecules the Pb(1 1 1) sample was transferred to a home-built manipulator and cleaned. The sample was turned away from the C_{60} evaporator and left to rest, in order to assume room temperature. The molecule evaporator was heated with a current of $\approx 1.2\,\mathrm{A}$ for approx 30 min. A quartz balance was used to monitor the flow of molecules. After a steady flow was reached the sample was turned towards the opening of the molecule evaporator for $\approx 5\,\mathrm{s}$. Finally, the evaporator was turned off. The sample was transferred into the STM for analysis. Large and homogeneous hexagonal C_{60} islands were desired.

[6] Institute for Chemistry and Biotechnology, Ilmenau University of Technology, D-98684 Ilmenau, purity 99.99%

[7] HeatWave Labs, Inc., 195 Aviation Way, Suite 100, Watsonville, CA 95076, USA

2.3 Summary of Experimental Procedures

A STM is available, operating in ultra-high vacuum (10^{-9} Pa) and at 6 K. Au(1 1 0) and Pb(1 1 1) crystals were cleaned by Ar^+ bombardment and annealing. Single Co atoms were deposited at $\approx$ 8 K from an electron beam evaporator through openings of the radiation shield of the cryostat. Prior to deposition the Co rod had been thoroughly degassed to reduce the amount of concomitantly adsorbed hydrogen [83, 84]. The deposition of C_{60} (purity: 99.99 %) was performed by exposing the Pb(1 1 1) surface at room temperature to a flux of C_{60} molecules sublimated from a heated Ta crucible. Topographic STM images were recorded at constant current with the bias voltage applied to the sample. Constant-height spectra of dI/dV were acquired by modulating the bias voltage and measuring the current response with a lock-in amplifier. I-V-curves were acquired simultaneously to convert the lock-in output in SI units. To facilitate comparison with model calculations d^2I/dV^2 data were divided by dI/dV, obtained from numerical integration of d^2I/dV^2.

3 Optimization of a Scanning Tunneling Microscope

Scanning tunneling microscopes are designed to conduct a wealth of physical experiments. Basic requirements for a STM include acquisition of real space surface topography [85] and spectroscopy of molecular orbital signatures [55]. More advanced experiments may demand single atom manipulation [56], controlled contacting of single molecules [86], or examination of molecular vibrational signatures [26]. To enable these experiments a well decoupled microscope is advantageous. Due to its working principle the STM is highly sensitive to disturbances in the setup environment. Mechanical vibrations modify the tunneling current by variation of the tunneling junction. Electrical disturbances are introduced by coupling, and from thermal and triboelectric effects. However, an excellent design configuration overcomes environmental influences and enables topographic and spectroscopic high resolution. Appropriate methods include mechanical vibration damping, electrical shielding, and elaborate grounding.

Since physical effects like superconductivity emerge at low temperatures, a well cooled STM considerably extends the experimental scope. Connected to a bath cryostat, the instrument's base temperature is kept low by installation of heat sinks, while minimizing heat introduction. The required structural enhancements are attained by well chosen materials and by appropriate dimensioning of the deployed components.

The STM setup optimized herein is a home-built ultra high vacuum system, initially constructed in earlier works [87, 88]. The microscope was proven to function appropriately at temperatures of liquid nitrogen ($T = 80$ K), using the example of the Ag(1 1 1) Shockley surface state [88]. The following section describes the route towards precise measurements at liquid helium temperatures. In particular, previously published inelastic features

[26] were made accessible. Moreover, previously unknown spectroscopic details were detected. The optimized setup exhibits improved current stability, lower bias voltage noise, and almost identical base temperature.

3.1 Optimized Setup

The experimental setup consists of two vacuum chambers. Samples are prepared in the preparation chamber; characterization is performed in the analysis chamber. The scanning tunneling microscope is housed in the analysis chamber at the bottom of a liquid helium cryostat. Surrounding shields, held at low temperatures, screen thermal radiation. Details about the vacuum system, scanning functionality and sample movement have been described elsewhere [87, 88]. In this section the focus is on the structural changes that led to an excellently tuned instrument. Specifically, additional damping, thermal connection to the liquid helium bath, and reconstruction of the cabling are discussed.

Figure 3.1 shows the core part of the final setup. On top of the STM a copper ring part was attached, which is kept up by three vertical copper rods. During measurements, the STM is suspended on three springs (Gutekunst, Material Inconel X-750). The springs are attached with hooks to the top of the STM and to the bottom of the liquid helium cryostat. For cooling, the STM may be pushed down into contact with the inner shield. The mechanism is driven by a stainless steel hollow rod, attached to a linear motion vacuum feedthrough (Huntington L-2111) at the cryostat top. A rod guidance at the cryostat neck pipe was finely tuned to move freely and was lubricated with MoS_2 powder.

Thin cables with stainless steel conductors connect electrical vacuum feedthroughs at the top of the cryostat with plugs (2× Caburn C9-VCS/VCP) at the bottom. In particular, coaxial cables (Janis Mini-Coax) are used for tip, scanner piezo, and sample connections. Temperature diode and coarse approach are connected via single stranded wires (Caburn KAP4K-014). On top of the 20 K shield and at the bottom of the cryostat cables are clamped with copper slices to the cryostat. The outer cable insulation of coaxial cables was stripped at the clamp site, which ensured grounded and well cooled shields. The insulation jackets

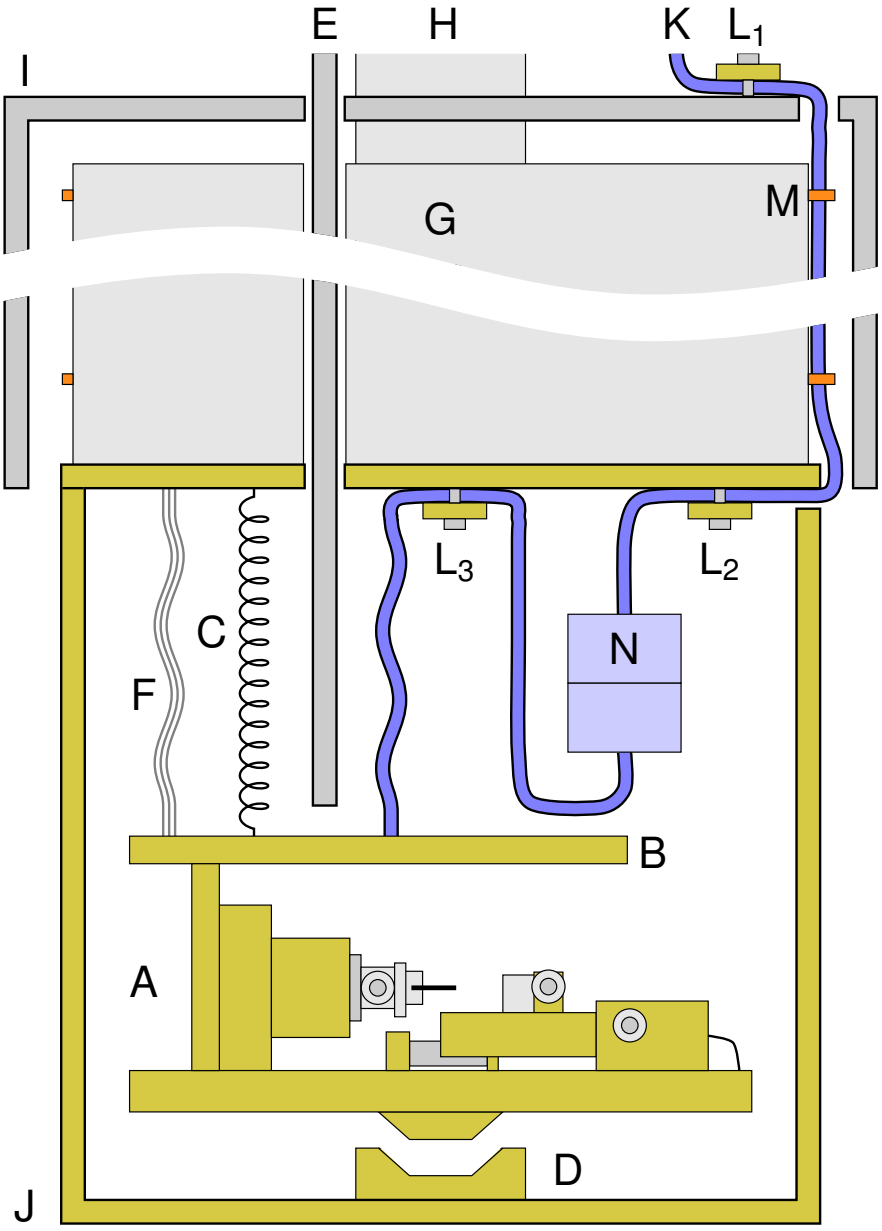

Figure 3.1 Sketch of the core part of the optimized experimental setup. The STM (A) is terminated by a copper ring part (B) on top. The microscope is suspended on springs (C). For cooling down, the STM may be pushed down into a tapered blind hole (D), using a stainless steel rod (E). Ag wires (F) provide thermal conduction to the liquid helium dewar (G), which is filled through the cryostat neck pipe (H). Introduction of heat by thermal radiation is minimized through surrounding shields held at 20 K (I) and 4 K (J). Cables (K) are fixed via clamps (L_1–L_3) and thin copper wires (M) at various positions. The plugs (N) facilitate maintenance.

of single stranded wires were kept. At the clamps for these cables electrical insulation was enhanced by sapphire plates and thin polyimide foil. All cables were led along the outer wall of the liquid helium cryostat, where they were fixed with thin copper wires. The copper wires were wrapped horizontally around the cryostat, spaced at distances of approximately 3 cm.

The cabling between plugs and microscope was retained, since their materials offer high thermal conductivity. Clamps were installed on top of the STM and at the bottom of the cryostat. Additional thin Ag wires (Advent Research Materials, diameter 0.05 mm, purity 99.99%) ensured well thermal linking of the STM to the liquid helium bath. The described changes were deployed to enable the resolution of faint spectroscopic features while keeping a low base temperature.

Resolution of Spectroscopic Features

In order to extract spectral information, the tunneling current and its derivatives are recorded as a function of the applied bias voltage. The current I is measured with a transimpedance amplifier (Femto DLPCA-200), which is located at the cryostat top. The amplifier outputs a voltage proportional to I. Derivatives of the current are extracted using a lock-in amplifier (Stanford Research Systems, SR830-DSP). The output is a voltage proportional to either $\mathrm{d}I/\mathrm{d}V$ or $\mathrm{d}^2I/\mathrm{d}V^2$. Best results are obtained with signals exhibiting low alternating voltage root mean square values and low power spectral densities. Such signals facilitate the resolution of faint spectroscopic features, crucial to recent experimental work. Mechanical disturbances were effectively reduced by suspending the microscope on springs. Attenuation of electrical disturbances was accomplished by RC low pass filters (cutoff frequency 10 kHz), applied at all high voltage inputs at the cryostat top. The bias voltage input was low-pass filtered, too (cutoff frequency 1 kHz or 10 kHz, according to the lock-in modulation frequency). Bias voltage fluctuations were further attenuated by application of a voltage divider, adjusted, that the required voltage range was covered. Cables at ambient conditions were wrapped into grounded Al foil, which provided additional electrical shielding. The choice of shielded coaxial cables for tunneling circuit and piezo signals

decreased capacitive coupling between the channels. During measurements, inputs for the temperature diode and coarse approach were grounded at the vacuum feedthrough. Finally, idle instruments were turned off.

The effect of these modifications may be visualized by comparing measurements of C_{60} vibrational features in IET spectra acquired before and after the upgrade. Figure 3.2(a) shows normalized IET spectra gained with a Pb covered W tip atop a C_{60} molecule adsorbed to the Pb(1 1 1) surface. Prior to optimization solely a broad background is visible, which corresponds to the C_{60}-LUMO signature. The improved instrument resolves several inelastic features through reduced scattering of the data. Corresponding background subtracted spectra shown in Fig. 3.2(b) deliver a faint hint for presence of the $H_g(7)$ mode (175 meV) before refinement. However, the optimized experiment resolves clear features. Voltages at these specific structures match the well-known energies of C_{60} vibrational modes [see Chapter 6].

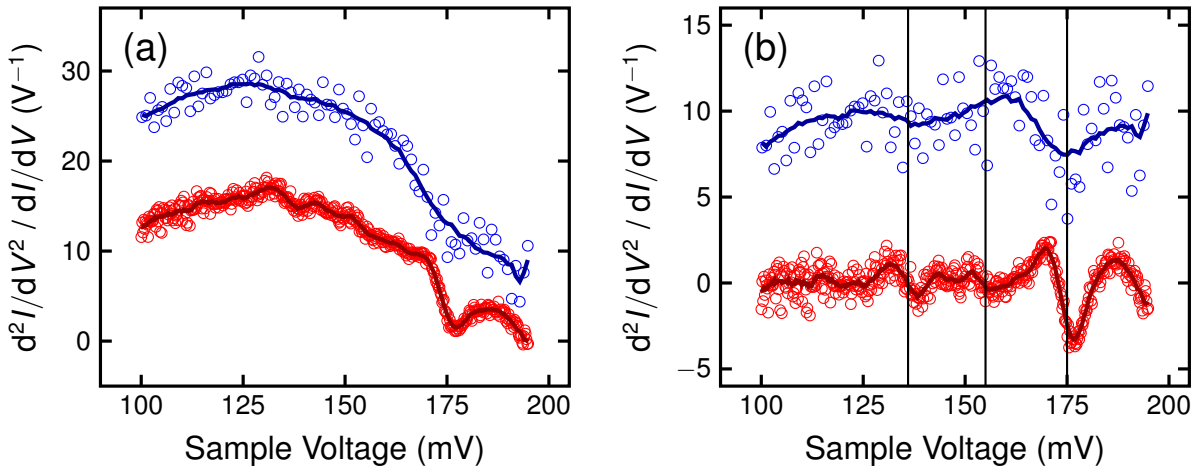

Figure 3.2 (a) IET spectra acquired atop a C_{60} molecule embedded in the hexagonal monolayer before (blue circles) and after (red circles) the optimization of the instrument. Solid lines show smoothed data to emphasize spectral features. Feedback loop was opened at (before) 0.1 nA, 200 mV, bias modulation amplitude $V_{\mathrm{mod}} = 8.5$ mV at $f_{\mathrm{mod}} = 444$ Hz and (after) 1 nA, 210 mV, $V_{\mathrm{mod}} = 4.2$ mV at $f_{\mathrm{mod}} = 946$ Hz. **(b)** Background subtracted spectra from (a). After optimization random disturbances of the spectral features are significantly reduced, revealing vibrational signatures of H_g modes at 136, 155 and 175 meV (vertical lines). Spectra have been offset for clarity.

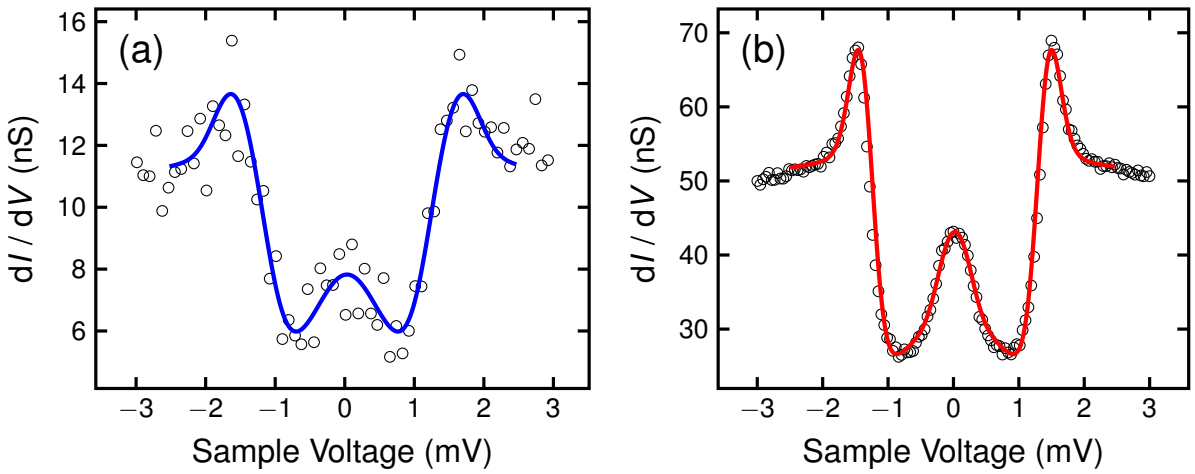

Figure 3.3 dI/dV spectra (circles) acquired with a superconducting Pb coated W tip atop the pristine Pb(1 1 1) surface **(a)** before and **(b)** after the optimization. Feedback loop was opened at (a) 20 mV, 1 nA, voltage modulation amplitude $V_{\mathrm{mod}} = 0.1\,\mathrm{mV}$ at $f_{\mathrm{mod}} = 314\,\mathrm{Hz}$ and (b) 40 mV, 0.1 nA, voltage modulation amplitude $V_{\mathrm{mod}} = 0.42\,\mathrm{mV}$ at $f_{\mathrm{mod}} = 3.2\,\mathrm{kHz}$, respectively. Solid lines indicate least-squares fits to the experimental data.

Base Temperature

After suspending the microscope body on springs heat conduction to the liquid helium reservoir was re-established. To maintain a low base temperature, highly thermoconductive silver wires (10^2–10^4 W/(m · K)[89]) were attached between the STM body and the liquid helium cryostat bottom. Additionally, well thermoconductive signal cables were clamped to the cryostat bottom and to the microscope. Introduction of heat is minimized by utilizing thin stainless steel cables, connecting room temperature and 4 K parts. In order to reach the base temperature quickly, the rod is used to push the microscope down into contact with the shield. During the cool down procedure materials shrink according to their thermal expansion coefficient. Therefore, the rod position is readjusted several times. After establishing an equilibrium temperature, the microscope body may be reset to the free-hanging state.

The base temperature was measured using the superconducting gap in the density of states present in a low cooled Pb sample. Figure 3.3 shows dI/dV-spectra acquired with a superconducting Pb coated W tip atop the pristine Pb(1 1 1) surface. Prior to optimization [Fig. 3.3(a)] the fit [Appendix A.1] yields a temperature of 6.1 K for both, sample and tip.

The standard deviation of the bias voltage fluctuations was approximated 0.218 mV, which amounts to a minimum effective temperature of $T_{\text{eff}} = 6.26\,\text{K}$ [see Chapter 2]. After instrumental refinement [Fig. 3.3(b)] temperatures for one electrode $T = 6.0\,\text{K}$ and $T = 6.6\,\text{K}$ for the other lead are extracted, averaging at $T = 6.3\,\text{K}$. The standard deviation of the bias voltage fluctuations was 0.158 mV, which leads to a minimum effective temperature of 6.38 K. Note, significant lowering of signal fluctuations in the $\mathrm{d}I/\mathrm{d}V$ spectra is obtained after setup improvement, consistent with IET data shown above.

Further Optimization Results

Implementation of cables with low thermal conductivity facilitates long cryostat standing times. A filling of the 4 l inner cryostat typically lasts 39 h. The average helium consumption therefore amounts to 100 ml/h, equal to commercially available instruments[1]. Intriguingly, the helium consumption is dependent on the filling level. At low filling levels, the specified optimal helium consumption (80 ml/h) is approximately reached (85 ml/h). The remaining standing time is derived in Appendix A.2.

Further effort was expended to improve vacuum quality and base pressure. Ion pumps in both vacuum chambers were exchanged. A final base pressure of $1.12 \cdot 10^{-9}\,\text{Pa}$ was achieved after baking the instrument appropriately. Finally, important properties of the instrument are summarized in Table 3.1.

Specifications	
Base temperature	6.3 K
Effective temperature	6.38 K
Energy resolution	1.9 meV
LHe hold time	39 h
LHe consumption	0.1 l/h
Base pressure	$1.12 \cdot 10^{-9}$ Pa

Table 3.1 Important properties of the optimized setup. Energy resolution is estimated from $\Delta E = 3.5 k_{\text{B}} T_{\text{eff}}$ [Eq. (2.6)].

[1] SPECS JT-STM: 100 ml/h

Publications

The described setup enables state-of-the-art experiments. Up to now, four peer-reviewed publications were issued, which report experimental data obtained at the instrument. The publications are listed hereafter.

* S. Meierott, T. Hotz, N. Néel, and J. Kröger, *Asymmetry parameter of peaked Fano line shapes*, Rev. Sci. Instr. **87**, 103901 (2016)

* S. Meierott, N. Néel, and J. Kröger, *Spectroscopic Line Shapes of Vibrational Quanta in the Presence of Molecular Resonances*, J. Phys. Chem. Lett. **7**, 2388-2393 (2016)

* S. Meierott, N. Néel, and J. Kröger, *Kondo effect of single Co atoms on Au(110)*, Phys. Rev. B **91**, 201111 (2015)

* T. Kreuch, S. Meierott, N. Néel, W. J. D. Beenken, and J. Kröger, *Atom-by-Atom Dehalogenation of a Porphyrin Molecule Adsorbed on Ag(111)*, J. Phys. Chem. C **118**, 30162–30169 (2014)

3.2 Conclusions

Structural enhancement of an existing ultra high vacuum and low temperature STM setup was conducted successfully. Measurements show, significant signal improvement was gained at the expense of a temperature increase by less than 5%. The presented microscope provides a reliable setup for experimental work in a vast field of physics, proven by various published experiments. Released publications comprise examination of molecular electronic states with single atom manipulation [55], the single-atom Kondo effect [90, 91] as well as faint inelastic vibrational signatures [92]. In particular, the instrumental improvement made low-intensity IET features accessible, and revealed previously unknown spectroscopic details [92]. Through accomplishing very low temperatures, experiments in a superconducting environment are feasible. Additionally, the cryostat standing time of 39 h enables two weeks of experiments with a commercially common liquid helium vessel (100 l). Low base pressures $< 10^{-8}$ Pa ensure excellent sample quality. Further instrument improvement may tackle the energy resolution obtained with a superconducting tip. The broadening from radio frequency noise may be eliminated by improved filtering.

4 KONDO EFFECT OF SINGLE CO ATOMS ON AU(110)

THE Kondo effect is one of the key electron correlation phenomena in solid-state physics. It describes the spin-flip scattering of the conduction electrons of a non-magnetic metal from an embedded or adsorbed magnetic impurity, which results in the screening of the impurity's magnetic moment [59]. At low temperatures a many-body non-magnetic singlet ground state is formed around the Fermi level of the metal. Its spectroscopic signature is referred to as the Kondo [59] or the Abrikosov-Suhl [62–64] resonance. The resonance width is proportional to $k_B T_K$ with k_B the Boltzmann constant and T_K the Kondo temperature.

Since the first observations of the single-atom Kondo effect in scanning tunneling spectroscopy (STS) experiments [10, 11] a wealth of STS data has been published for a variety of Kondo atoms on different metal surfaces [12]. An important issue of Kondo physics is the spatial extension of the polarized conduction electrons since it may provide the size of the so-called Kondo cloud. To unravel the spatial evolution of the Kondo effect the dependence of the Kondo amplitude on the distance to the magnetic impurity has been analyzed. The Kondo amplitude describes the spatial extent of the perturbation of the metal electron states at the Fermi energy E_F due to the presence of a Kondo impurity. In a pioneering work on Co atoms adsorbed to Cu(1 0 0) and Cu(1 1 1) [13] the position dependence of the Kondo amplitude was experimentally determined. In these experiments on flat surfaces the Kondo amplitude was demonstrated to isotropically decay around the Co atoms within ≈ 1 nm, [13] which reflects a rather common length scale for magnetic impurities adsorbed

on various surfaces [12]. Recently, long-range Kondo signatures were reported for Co and Fe atoms residing several atomic layers below the Cu(1 0 0) surface [93, 94]. Anisotropic Kondo amplitude distributions obtained on narrow terraces of the Ag(1 1 1) surface were ascribed to the electronic structure of the surface [20]. While experimental reports on the spatial variation of the single-atom Kondo amplitude are scarce [13, 20, 21, 93–95] many theoretical works on this topic are available, *e.g.*, Refs. [22, 61, 96–99].

Here we report STS data obtained from single Co atoms on Au(1 1 0). To date, a Kondo lattice fabricated from O_2 molecules on Au(1 1 0) [100] has been reported, which, however is not related to single-impurity Kondo physics as reported here. Also, the Au(1 1 0) surface exhibits a (1×2) reconstruction where every second Au row is missing in $\langle 0\,0\,1 \rangle$ directions. Since the (1 1 1) facets adjacent to each missing row offer oblique adsorption sites the Kondo effect may be analyzed in an anisotropic environment. We show that Co atoms residing at facet sites and within the missing rows exhibit zero-bias peaks in spectra of the differential conductance ($\mathrm{d}I/\mathrm{d}V$). These peaks are attributed to the spectroscopic signature of the single-Co Kondo effect on Au(1 1 0). Spatially resolved $\mathrm{d}I/\mathrm{d}V$ spectra acquired across Co atoms adsorbed to facet sites unveil different evolutions of the Kondo amplitude parallel and perpendicular to the missing-row direction. This observation is attributed to the different variations of tip-substrate distances in the two directions and highlights the importance of topographic effects in the spatial dependence of the Kondo effect.

4.1 Adsorption and Kondo Peaks

After deposition of Co on Au(1 1 0) typical STM images of Co-covered Au(1 1 0) appear as shown in Fig. 4.1. The bright and dark parallel lines represent the characteristic missing-row reconstruction of Au(1 1 0). Only a few Co atoms are visible at the low coverages used in the experiments. Four Co atoms are indicated by arrows in Fig. 4.1. Co atoms residing at facet sites are imaged as circular protrusions [Fig. 4.2(a)] whose center is ≈ 0.1 nm off a Au atom row [bright parallel lines in Figs. 4.2(a),(b)] of the (1×2)-reconstructed Au(1 1 0) surface. Such Co atoms have readily been moved to the missing row [dark lines

Figure 4.1 Constant-current STM image of Au(1 1 0)-(1 × 2) with adsorbed Co atoms at low coverage (50 × 28 nm^2, 1 nA, 50 mV). Arrows indicate single Co atoms adsorbed to facet sites. *This figure was reproduced [90] with permission from APS.*

in Figs. 4.2(a),(b)] by applying a voltage pulse atop the Co center (0.2–1 V, 1 nA) [see Appendix B.1]. Co atoms adsorbed in the missing row of the reconstruction exhibit a similar apparent height as Au(1 1 0) atomic rows [Fig. 4.2(b)] at the chosen bias voltage.[1] According to these STM images we suggest the adsorption configurations depicted in Fig. 4.2(c). Co atoms adsorbed to the (1 1 1) facets adjacent to a missing row occupy a threefold coordinated site, while within the missing row Co atoms are coordinated by five nearest Au atoms. These suggested adsorption sites are supported by manipulation experiments [see Appendix B.1], and by previous calculations, which revealed minimum adsorption energies for these sites [102]. In addition, simulated STM images of Co atoms residing at the aforementioned sites are in accordance with experimental data [102]. Below, Co atoms adsorbed on facet and missing-row sites will be referred to as f-Co and mr-Co atoms, respectively. In dI/dV spectra acquired atop the center of f-Co and mr-Co atoms a zero-bias peak is observed [Figs. 4.3(a), (b)].[2] We attribute this peak to the spectroscopic signature

[1] Depending on the tip conditions, apparent heights of mr-Co atoms varied by ≈ 10 pm.

[2] Prior to spectroscopy on Co atoms dI/dV spectra had been acquired on clean Au(1 1 0). Only those tips were used for further analysis of the Kondo signature that showed featureless Au(1 1 0) spectra in the relevant voltage range.

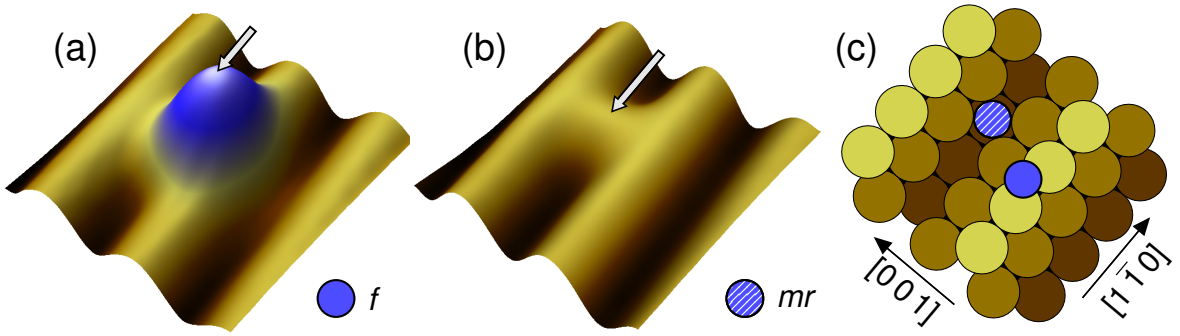

Figure 4.2 (a),(b) Pseudo-three-dimensional representations of STM images ($2 \times 2\,\mathrm{nm}^2$, 1 nA, 50 mV) of a single Co atom (indicated by the arrow) adsorbed to (a) a facet site and (b) in a missing row of Au(1 1 0). The color scale ranges from 0 pm (black) to 173 pm. STM data were processed using Gwyddion [101]. **(c)** Sketch of the suggested Co adsorption geometries. A Co atom residing at a facet (f, solid) site is coordinated by three Au atoms (larger solid circles). A Co atom adsorbed in the missing row (mr, hatched) has five nearest Au neighbors. Crystallographic directions are indicated. *This figure was reproduced [90] with permission from APS.*

of the Kondo effect, *i.e.*, to the Abrikosov-Suhl resonance. This assignment is in accordance with findings for Co on Cu(1 1 0), where the single-Co Kondo effect is represented by a peak at zero bias, too [17].

Before discussing the line shape of the resonance in more detail we comment on possible hydrogen-induced effects, which in ultrahigh-vacuum and low-temperature experiments play a crucial role [12, 83, 84, 103–107]. All STM images of f-Co and mr-Co atoms appear as the data sets depicted in Fig. 4.1 and Figs. 4.2(a), (b), *i.e.*, no evidence for additional species is available. Previously, the presence of H on surfaces was inferred from H complexes of the transition-metal atom, which exhibited different apparent heights in STM images [12, 83, 84, 103–107]. In addition, the H complexes could be interconverted by suitable tunneling parameters, which was not observed in our case. Therefore, a contamination of Co atoms with H can be excluded. Single Kondo atoms scarcely exhibit a symmetric peak shape of the Abrikosov-Suhl resonance, which has only been reported for Co on Cu(1 1 0) [17], on an ultra-thin Cu_2N film on Cu(1 0 0) [18] and on graphene-covered Ru(0001) [19] so far. It has been argued that a high density of Co 3d states at E_F may be related to the appearance of the Abrikosov-Suhl resonance as a peak in $\mathrm{d}I/\mathrm{d}V$

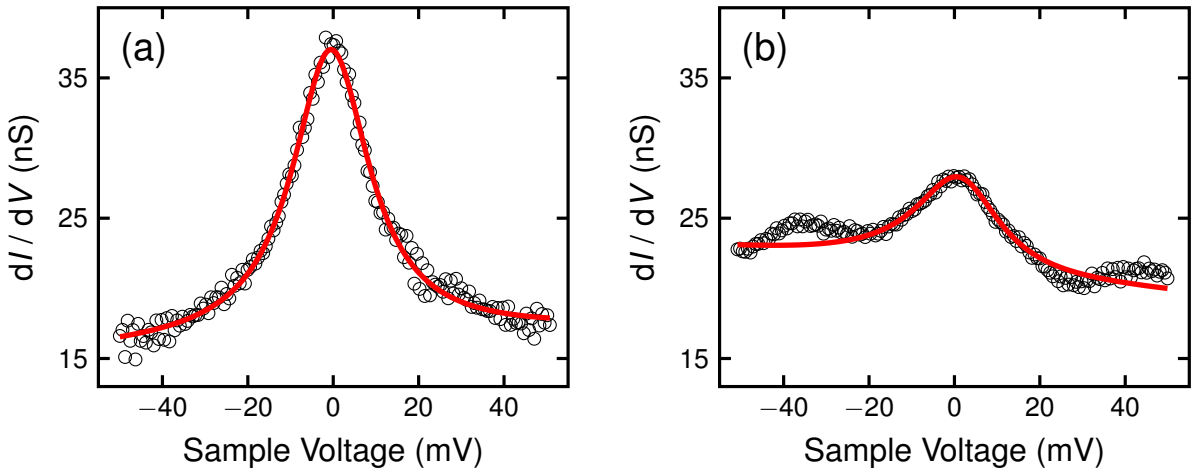

Figure 4.3 Spectra of $\mathrm{d}I/\mathrm{d}V$ acquired atop a Co atom adsorbed to **(a)** the facet site and **(b)** in the missing row. Experimental data appear as circles. The full lines represent fits of $F(V)$ [Eq. (4.1)] to experimental data with Fano fit parameters at the facet site (a) $T_\mathrm{K} = 127\,\mathrm{K}$, $q = -22.0$, $\varepsilon_\mathrm{AS} = -0.5\,\mathrm{mV}$ and in the missing row (b) $T_\mathrm{K} = 141\,\mathrm{K}$, $q = -11.3$, $\varepsilon_\mathrm{AS} = 1.8\,\mathrm{mV}$. Prior to spectroscopy the feedback loop was disabled at 1 nA, 50 mV. The modulation was set to $V_\mathrm{mod} = 4.2\,\mathrm{mV}$, $f_\mathrm{mod} = 6.2\,\mathrm{kHz}$. *This figure was reproduced [90] with permission from APS.*

spectra [17]. For, *e.g.*, Co on Cu(1 0 0) and Cu(1 1 1) the crystal field splitting is responsible for a depletion of Co 3*d* resonances at E_F and the Abrikosov-Suhl resonance appears as an asymmetric Fano line and as a dip in $\mathrm{d}I/\mathrm{d}V$ spectra, respectively [17]. To compare the Abrikosov-Suhl resonances of the two Co adsorption species quantitatively, experimental data were fit by

$$F(V) = af(V) + bV + c \tag{4.1}$$

with fit parameters a, b, c, and the Fano function $f(V) = [q + \varepsilon(V)]^2/[1 + \varepsilon(V)^2]$ (V: sample voltage). The Fano function contains the asymmetry factor q, which measures, the coupling of tunneling electrons to states of the magnetic impurity and to the electronic continuum of the substrate [see below]. The parameter $\varepsilon(V) = (\mathrm{e}V - E_0)/\Gamma$ contains the energy of the Abrikosov-Suhl resonance E_0 and its half width at half maximum $\Gamma = k_\mathrm{B}T_\mathrm{K}$. These quantities, *i.e.* q, E_0, and Γ, are additional fit parameters. The fit results are shown as

full lines in Figs. 4.3(a), (b).[3] For f-Co and mr-Co atoms we obtained $T_K = (120 \pm 11)$ K, and $T_K = (147 \pm 29)$ K, respectively.[4] Within the uncertainty margin an unambiguous trend towards higher T_K with higher coordination as reported previously [13, 109] cannot be identified. In general, the Kondo temperature depends in a more complex way on the hybridization with non-magnetic atoms [54, 110–113]. Compared to Kondo temperatures of Co on other noble-metal surfaces, *i.e.*, 70 K on Au(1 1 1) [11], 54 K on Cu(1 1 1) and 88 K on Cu(1 0 0) [13], 92 K on Ag(1 1 1) [14], the T_K values obtained here are relatively high. An increased T_K may be related to a high density of states at the Fermi energy, $\rho_c(E_F)$, since $T_K \propto \exp(-|J\rho_c(E_F)|^{-1})$ [114]. J is the exchange interaction energy of conduction electrons and Co 3d resonances. In Ref. [17] the calculated density of states projected on Co 3d orbitals at E_F was higher on Cu(1 1 0) than on Cu(1 0 0) and Cu(1 1 1), which may explain the high $T_K = 125$ K for Co on Cu(1 1 0) [17].

The large values of $|q|$ (see Sec. 4.2) reflect the nearly symmetric line shape of the resonance, which for $|q| \gg 1$ becomes a Lorentzian function. It has been discussed on general grounds that a large negative value of q, *i.e.*, a symmetric peak shape of the Abrikosov-Suhl resonance, may be expected for sp-like substrate bands [96]. The size and sign of q may be altered by additionally considering matrix elements describing the hybridization between the impurity and the substrate [96].

[3] For f-Co atoms the entire voltage range from −50 mV to 50 mV was used for the fit. In the case of mr-Co atoms a reduced voltage range from ≈ -20 mV to ≈ 20 mV had to be applied due to the onset of sidebands at $\approx \pm 30$ mV. These features may be due to vibrational excitations of the single Co atom [108] and does not belong to the Kondo signature.

[4] Broadening of the Abrikosov-Suhl resonance due to the temperature (6 K) and the bias voltage modulation (4.2 mV) are considered. The values for T_K are arithmetic averages over fit parameters obtained from dI/dV spectra acquired with different tips and on different days. Uncertainty margins are given for a confidence level of 95%.

4.2 Topographic Effect

Spatially resolved $\mathrm{d}I/\mathrm{d}V$ spectroscopy was performed across f-Co atoms [Figs. 4.4(a)–(c)]. Prior to spectroscopy the feedback loop had been disabled at the same tunneling parameters for each spectrum. In contrast to previous experiments on flat surfaces [13] we find an anisotropic variation of the Abrikosov-Suhl resonance for f-Co atoms. To see the anisotropy most clearly the amplitude, $A_{\mathrm{exp}} = a(1+q^2)$, has been extracted from $\mathrm{d}I/\mathrm{d}V$ spectra acquired along [0 0 1] [Fig. 4.4(d)] and [1 $\bar{1}$ 0] [Fig. 4.4(e)] directions across the Co atoms. The spatial evolution of A_{exp} differs significantly along [0 0 1] and [1 $\bar{1}$ 0]. Along [0 0 1], *i.e.*, perpendicular to the missing-row direction, A_{exp} evolves asymmetrically with respect to the Co topographic maximum, which is set to 0 nm [vertical dashed lines in Figs. 4.4(d)—(g)]. The distance between the maximum of the Kondo amplitude and the topographic maximum of the Co atom is ≈ 0.2 nm. In [1 $\bar{1}$ 0] directions, *i.e.*, parallel to the missing-row direction, the Kondo amplitude and the topographic data evolve symmetrically with respect to the Co topographic maximum. For mr-Co atoms A_{exp} evolves symmetrically along both directions, *i.e.*, the maximum Kondo amplitude and the Co topographic maximum coincide [see Appendix B.2]. Figure 4.5(a) shows the variation of q as a function of the lateral distance r to the Co atom at $r = 0$ nm.[5] The data follow approximately a Gaussian profile (full line) along all investigated directions [Fig. 4.5(b)]. Negative q were previously reported for Co on Au(1 1 1) [16], for Co on Ag films on Au(1 1 1) [115], and for Co on Cu(1 1 0)-(1×2)O [17]. Γ and E_0 show no particular location dependence. To understand the spatial variation of A_{exp} we express the prefactor a in Eq. (4.1) as $a(r) = a_0(r)t_{\mathrm{c}}^2$ [16, 22, 61, 97]. Here, $a_0(r)$ describes the dependence of a on the lateral distance r to the magnetic impurity at $r = 0$, which we approximated as a Gaussian profile close to the Kondo atom [13]. The tip-substrate coupling parameter, t_{c}, is the wave-vector independent part of the tip-substrate matrix element [22]. It depends exponentially on the tip-Au(1 1 0) distance, $t_{\mathrm{c}} \propto \exp(-\Delta z/\lambda)$. Here, $\Delta z = z_{\mathrm{Co}} - z_{\mathrm{Au}}$ is given by the difference

[5] The uncertainty margins become larger with increasing $|q|$. For $q < -20$ spectroscopic data were equally well fit with even lower asymmetry factors. An analysis of these observations revealed, fitting based on an improved parameterization [see Sec. 5.3] is advantageous. With this method we were able to extract fit parameters and uncertainty margins at more positions. The results are shown in Appendix B.3.

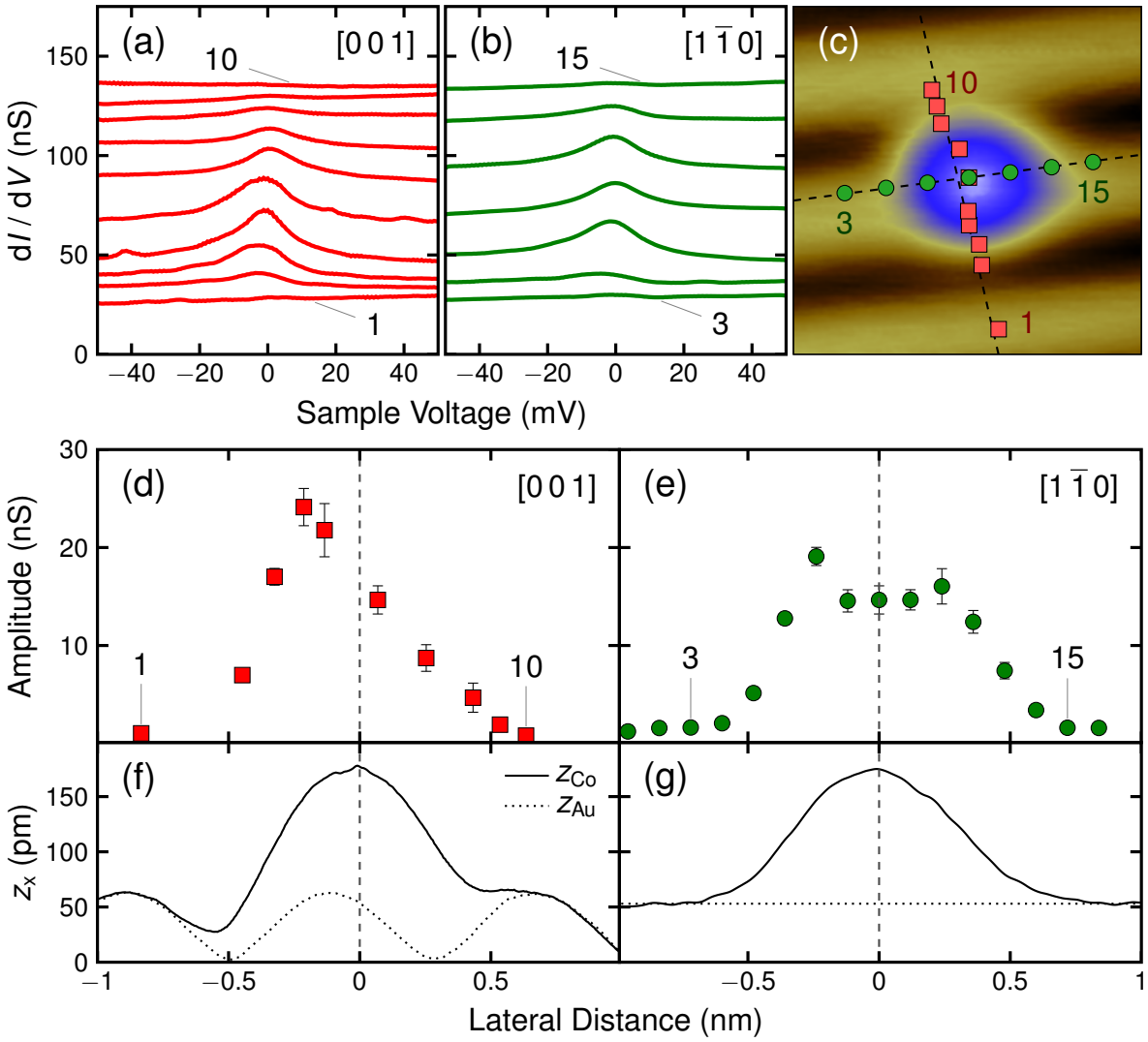

Figure 4.4 (a) Set of $\mathrm{d}I/\mathrm{d}V$ spectra acquired across a single f-Co atom along [0 0 1]. The individual spectra are numbered according to the position at which they were recorded, as indicated in (c). Prior to spectroscopy the feedback had been disabled at 1 nA, 50 mV for each spectrum. The modulation was set to 4.2 mV, 6.2 kHz. **(b)** Like (a) along [1 $\bar{1}$ 0]. **(c)** STM image of a single Co atom adsorbed to a facet site of Au(1 1 0) (1 nA, 50 mV, $2 \times 2\,\mathrm{nm}^2$). Dashed lines indicate directions along which $\mathrm{d}I/\mathrm{d}V$ spectra in (a), (b) were acquired. Numbers 1–10 along [0 0 1] and 3–15 along [1 $\bar{1}$ 0] correspond to the labeling of spectra in (a) and (b), respectively. **(d)**, **(e)** Amplitude, $A_{\mathrm{exp}} = a(1+q^2)$, extracted from fits of $F(V)$ [Eq. (4.1)] to $\mathrm{d}I/\mathrm{d}V$ data depicted in (a), (b). **(f)**, **(g)** Cross-sectional profiles of Co, z_{Co}, adsorbed to a facet site along [0 0 1] (f) and [1 $\bar{1}$ 0] (g) depicted as full lines. Dotted lines show cross-sectional profiles of clean Au(1 1 0), z_{Au}, along [0 0 1], [1 $\bar{1}$ 0] at the same bias voltage as z_{Co}. The vertical dashed lines indicate the positions of topography maxima. *This figure was reproduced [90] with permission from APS.*

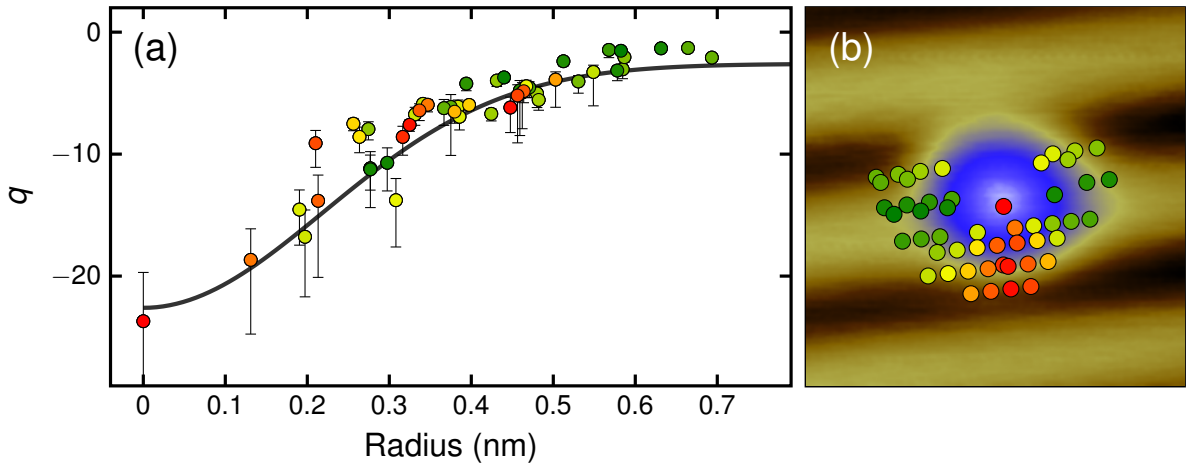

Figure 4.5 (a) Asymmetry parameter q (dots) extracted from fits of $F(V)$ [Eq. (4.1)] to $\mathrm{d}I/\mathrm{d}V$ spectra acquired at positions indicated in (b). **(b)** Topographic map of a f-Co adatom (1 nA, 50 mV, $2 \times 2\,\mathrm{nm}^2$) with dots indicating positions of $\mathrm{d}I/\mathrm{d}V$ spectra from which asymmetry parameters in (a) were extracted. *This figure was reproduced [90] with permission from APS.*

of topographic profiles recorded across Co atoms [z_{Co}, full lines in Figs. 4.4(f), (g)] and across clean Au(1 1 0) [z_{Au}, dotted lines in Figs. 4.4(f), (g)]. Parameter λ is the vacuum decay length for conduction electron states of the substrate [22]. The asymmetry parameter reads $q = (t_{\mathrm{a}} + p t_{\mathrm{c}} \Lambda)/(p t_{\mathrm{c}})$ with t_{a} the tip-adsorbate coupling, Λ a dimensionless quantity related to the real part of the unperturbed substrate Green function and p a parameter containing the substrate density of states and the adsorbate-substrate hybridization matrix element [22]. A simplification is obtained by assuming $|t_{\mathrm{a}}| \ll |p t_{\mathrm{c}} \Lambda|$, *i.e.*, the contribution from direct tunneling into the adsorbate electronic levels is low. It has been argued that at typical tip-sample distances in STM experiments direct tunneling through impurity d states is negligible owing to their strong localization at the impurity site [22, 61, 96]. As a consequence of this assumption the asymmetry factor reads $q = \Lambda(r)$. Since $|\Lambda| = |q| > 1$ for Co on Au(1 1 0) we may use $1 + \Lambda^2 \approx \Lambda^2$. In the vicinity of the Kondo atom ($r \leq 1\,\mathrm{nm}$) $\Lambda(r)$ as well as $a_0(r)$ may be approximated by a Gaussian function.[6] With these settings

[6] The general spatial evolution of $\Lambda(r)$ for larger distances to the magnetic impurity is more complex. It exhibits oscillations with an exponentially damped amplitude [22]. At typical tip-sample distances in STM experiments the oscillations eventually disappear entirely. Only close to the impurity site a single peak remains that is approximated as a Gaussian here.

the expected amplitude of the Abrikosov-Suhl resonance reads

$$\begin{aligned} A(r) &= a_0(r) t_c^2 q^2 \\ &= \exp(-2\Delta z/\lambda) A_0 \exp(-r^2/(2s_0^2)) \end{aligned} \tag{4.2}$$

with fit parameters A_0 and s_0, which describe the height and the effective width of the product of two Gaussian functions, respectively. The vacuum decay length for conduction electrons was set to $\lambda = 0.09\,\mathrm{nm}$ [22]. In Eq. (4.2) the spatial dependence of a_0 and Λ is represented by a single Gaussian profile. For $\Lambda = q = 0$ the Gaussian profile of $a_0(r)$ must be considered and Eq. (4.2) has to be replaced by $A(r) = a_0(r)\exp(-2\Delta z/\lambda)$. From STM images acquired at the same voltage and current at which the feedback loop had been opened prior to $\mathrm{d}I/\mathrm{d}V$ spectroscopy Δz is obtained as the difference of adatom and substrate apparent heights [Figs. 4.4(f), (g)].

The results of the fits are presented as full lines for [0 0 1] [Fig.4.6(a)] and [1 $\bar{1}$ 0] [Fig. 4.6(b)] directions across f-Co atoms. The spatial evolutions of A_{exp} [dots in Figs. 4.6(a), (b)] are reproduced. In particular, the asymmetry of A_{exp} with respect to the Co topographic center along [0 0 1] is observed in $A(r)$. From this analysis we infer that the topography of the surface may severely influence the apparent spatial evolution of the Kondo amplitude extracted from STS experiments. The tip-substrate coupling parameter, t_c, contains the variation of the tip-substrate distance and is crucial for an improved description of the distance dependence of the Kondo amplitude. Indeed, after dividing A_{exp} by t_c^2 [Fig. 4.6(c)] the normalized amplitude, A_{exp}/t_c^2, is virtually identical for [0 0 1] and [1 $\bar{1}$ 0] directions.

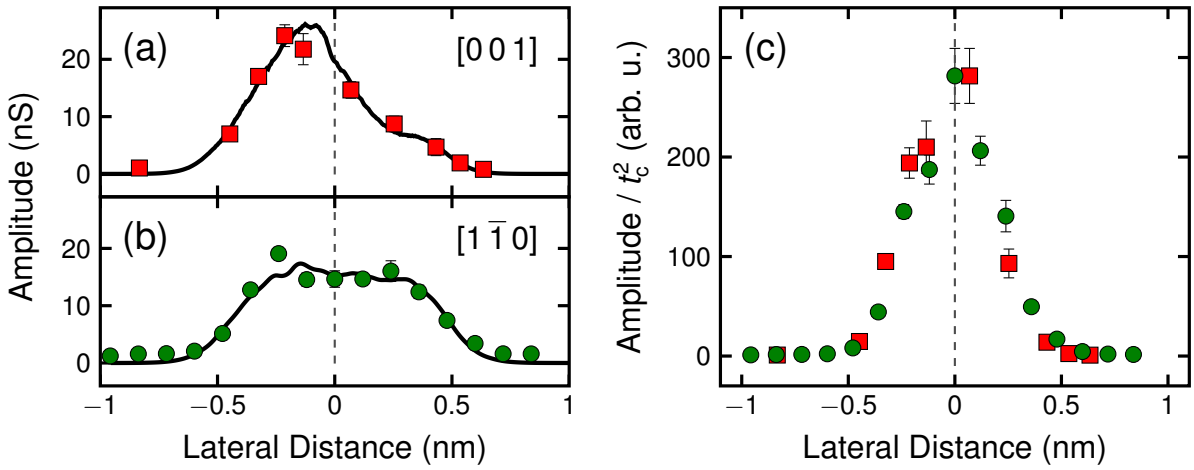

Figure 4.6 (a), **(b)** Experimental amplitudes, $A_{\mathrm{exp}} = a(1+q^2)$ (squares, dots), along indicated crystallographic directions together with fits (full lines) according to Eq. (4.2) for f-Co atoms on Au(1 1 0). **(c)** Normalized Kondo amplitude, A_{exp}/t_c^2, along [0 0 1] (squares) and [1 $\bar{1}$ 0] (dots). *This figure was reproduced [90] with permission from APS.*

4.3 Conclusions

Single Co atoms adsorbed to (1×2)-reconstructed Au(1 1 0) exhibit the Kondo effect, whose spectroscopic signature appears as a zero-bias peak in dI/dV spectra. The oblique adsorption geometry of Co at facet sites is reflected by the anisotropic evolution of the Kondo resonance amplitude in spatially resolved dI /dV spectra. This effect is due to variations of the tip-surface distance, which for an adequate interpretation of the spatial dependence of the Kondo amplitude have to be taken into account. The presented findings are relevant to investigations into the variations of the Kondo effect when tip-surface distances vary significantly, *e.g.*, for the spatially resolved Kondo effect across molecules.

5 Asymmetry Parameter of Peaked Fano Line Shapes

Reprinted (adapted) with permission from Review of Scientific Instruments 87, 103901 (2016). Mathematical support was provided by ***Thomas Hotz*** *from the Institute for Mathematics, Ilmenau University of Technology.*

FANO line shapes in spectroscopy are ubiquitous [116]. They generally occur when a discrete excitation couples to a continuum of states [117–120]. The resulting spectroscopic resonance profile exhibits a characteristic asymmetry. In the original optical absorption experiments with noble gases this asymmetry was traced to a competition between two excitation amplitudes [119]. One of these describes the direct excitation from a lower state to a discrete level embedded in a continuum, while the other considers the indirect excitation *via* the continuum to the discrete state [119]. This picture of the Fano model leads to its most basic form where quantum interference of two alternative excitation pathways occurs. Such interferences were reported for the ionization of atoms [119], Raman scattering [121], molecular spectroscopy [122, 123], infrared absorption reflection [124] and electron energy loss [125–128] spectroscopy, quantum transport [129], optical absorption in quantum wells [130] and light propagation in photonic devices [131, 132]. To quantify the relative contributions of these pathways to the interference Fano introduced the asymmetry parameter, q, as a measure for the ratio of transition probabilities to the discrete state and to the continuum [120]. For $|q| \to \infty$ the transition to the continuum is negligible. In this case the line shape of the resonance exhibits a Lorentzian profile. When $q \approx 1$, transitions to the discrete state and the continuum are of comparable probability and the resonance adopts an asymmetric profile. Zero asymmetry parameter leads to a

symmetric dip as the resonance line shape.

In solid state physics the Fano model was successfully applied to the description of the single-atom Kondo effect [10, 11]. The Kondo effect represents an important electron correlation phenomenon in solid state physics [114]. It describes the screening of localized magnetic moments by the continuum of conduction electrons [59]. Experiments with a scanning tunneling microscope (STM) unveiled the Kondo effect of single magnetic atoms adsorbed to surfaces [10, 11]. The spectroscopic signature of the Kondo effect — the Abrikosov-Suhl or Kondo resonance — appears with a Fano line shape in tunneling spectra of the differential conductance ($\mathrm{d}I/\mathrm{d}V$). Spin-conserving tunneling may occur directly from the tip to the continuum of the conduction electrons of the sample and *via* the Kondo resonance. The interference of tunneling electrons in these two paths leads to the characteristic Fano line shape. Since its first experimental observation [10, 11] the single-atom Kondo effect was reported for a wealth of magnetic atoms on different surfaces, as summarized in an excellent review article [12].

The resonance profile in $\mathrm{d}I/\mathrm{d}V$ spectra may be described by

$$F(E) = f(E) + bE + c \tag{5.1}$$

with the Fano function

$$f(a, q, \Gamma, E_0; E) = a\,\frac{[q + (E - E_0)/\Gamma]^2}{1 + [(E - E_0)/\Gamma]^2} \tag{5.2}$$

($E = eV$: energy of tunneling electrons with e the elementary charge and V the bias voltage, E_0: resonance energy, Γ: half width at half maximum). The quantity $A = a(1 + q^2)$ is generally referred to as the amplitude. The constants b, c are additional fit parameters, which take possible linear slopes (b) and offsets (c) into account. The extraction of the asymmetry parameter plays an important role since it describes the hybridization and the magnetic interaction of the Kondo atom with its environment [54, 109–113, 133–138]. Moreover, the asymmetry parameter has been predicted to reveal a faint oscillatory behavior with the lateral distance to the Kondo impurity [22, 61]. These oscillations may be

accompanied with alternating sign changes of q. This behavior reflects the perturbation of the conduction electron continuum by the presence of the Kondo atom [22]. Therefore, a reliable determination of the asymmetry parameter with clear accuracy margins is highly desirable.

However, fitting experimental data consisting of M data points (E_i, y_i) by nonlinear least-squares *via* minimization of the sum of squared residuals

$$\chi^2 = \sum_{i=1}^{M} |y_i - F(a, q, \Gamma, E_0, b, c; E_i)|^2 , \tag{5.3}$$

i. e., finding $\chi^2_{\mathrm{f}} = \min\limits_{a,q,\Gamma,E_0,b,c} \chi^2$, requires optimization in a six-dimensional parameter space (a, q, Γ, E_0, b, c), which, as exposed below, becomes particularly challenging for nearly symmetric and peak-like Fano resonances ($|q| \gg 1$).

In this article we concentrate on Abrikosov-Suhl resonances which exhibit a nearly symmetric and peaked Fano line profile in $\mathrm{d}I/\mathrm{d}V$ spectra. To date Fano line shapes of single-atom Kondo effects with exceptionally high q ($q > 10$) have been reported for Co adsorbed to Cu_2N on Cu(1 0 0) [18], Cu(1 1 0) [17], graphene-covered Ru(0 0 0 1) [19] and to Au(1 1 0) [90]. We show that in the case of such symmetric Fano line shapes the asymmetry parameter q may vary over orders of magnitude without degrading the fit of $F(a, q, \Gamma, E_0, b, c; E)$ [Eq. (5.1)] to the $\mathrm{d}I/\mathrm{d}V$ spectra. The combination of the symmetric line shape with the inevitable scattering of experimental data impedes the unambiguous extraction of the asymmetry parameter. An improved parameterization of the Fano function [Eq. (5.2)] is suggested in order to reduce the nonlinear part of the optimization to only two parameters. The reduced parameter space dimension also facilitates the visualization of the fit results in form of a two-dimensional plot of χ^2 [Eq. (5.3)]. Moreover, the reparameterized fit function removes the dependence on initially guessed fit parameters if a global minimum is present in this two-dimensional plot. In addition, while uncertainty margins of q that are estimated on the basis of linear error propagation are unreasonably high, an angular representation of the asymmetry parameter enables the specification of reliable uncertainty margins.

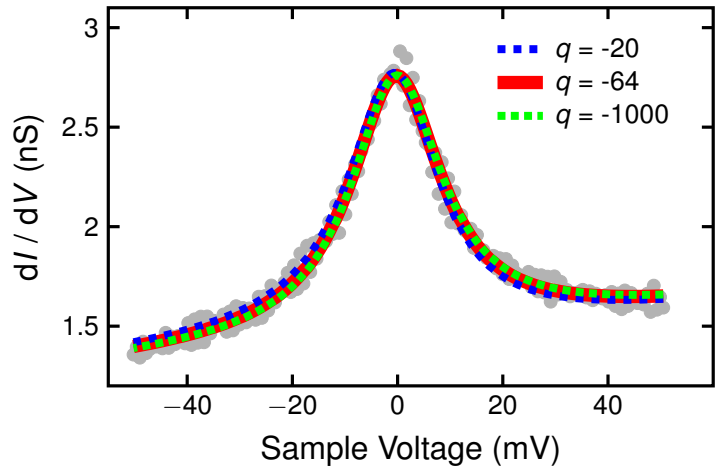

Figure 5.1 Spectrum of $\mathrm{d}I/\mathrm{d}V$ (dots) acquired atop a Co atom adsorbed to a facet site of the Au(1 1 0) reconstruction. The feedback loop had been disabled at 1 nA, 50 mV prior to data acquisition. The bias voltage modulation was set to $V_{\mathrm{mod}} = 4.2\,\mathrm{mV}$, $f_{\mathrm{mod}} = 6.2\,\mathrm{kHz}$. Full, dashed and dotted lines represent fits of $F(E = eV)$ [Eq. (5.1)] to the data with indicated asymmetry parameters q. *This figure was reproduced [91] with permission from AIP.*

5.1 Experimental Observation

Figure 5.1 shows a typical $\mathrm{d}I/\mathrm{d}V$ spectrum acquired atop a Co atom adsorbed to a facet of the Au(1 1 0) missing-row reconstruction [90]. The zero-bias resonance was previously attributed to the spectroscopic signature of the single-Co Kondo effect on Au(1 1 0) [90]. The experimental data (dots) were fit by $F(E = eV)$ [Eq. (5.1)] using a nonlinear least-squares algorithm [139, 140]. The result is depicted as a full line ($q = -64$). Importantly, fits with other asymmetry parameters, *i. e.*, $q = -20$ (dashed line) and $q = -1000$ (dotted line), led to results with an almost identical χ^2_{f}. Obviously, despite the order-of-magnitude variation of q the fit results are very similar. In particular, in the central bias voltage region, *i. e.*, $-10\,\mathrm{mV} \leq V \leq 10\,\mathrm{mV}$, the fits are virtually identical. At larger bias voltages ($|V| > 10\,\mathrm{mV}$) faint deviations of the fits become discernible. These findings are in contrast to the situation of asymmetric Fano profiles for which q was extracted with small uncertainty margins [13].

5.2 Simulations

To understand the experimental observations, Fano line shapes $f(a_g, q_g, \Gamma_g, E_{0g}; E)$ [Eq. (5.2)] with asymmetry parameters $q_g \geq 0$, width $\Gamma_g = 0.01$, peak position $E_{0g} = 0$ and amplitude $A_g = a_g(1 + q_g^2) = 1$ were numerically generated (solid line in Fig. 5.2(a)). The scattering of experimental data was mimicked by adding a random number from a normal distribution with zero mean value and standard deviation $\sigma = 0.05$ to the Fano line shape at each of the equidistantly spaced nodes E_i ($i = 1 \ldots 200$). Data sets based on the same Fano profile but different scattering were then fit by $F(a_f, q_f, \Gamma_f, E_{0f}, b_f, c_f; E)$ [Eq. (5.1)]. The nonlinear least-squares method [Eq. (5.3)] yielded parameter estimates $(a_f, q_f, \Gamma_f, E_{0f}, b_f, c_f)$. For all data sets the fit ranges ($-0.05 \leq E \leq 0.05$), the number of nodes and the start parameters were identical. The individual steps were implemented in a previously reported Monte-Carlo algorithm [141]. All variables in the simulations are dimensionless for convenience.

A histogram of parameters q_f obtained from fitting 1000 numerically generated Fano profiles with $q_g = 15$ and $\sigma = 0.05$ is shown in Fig. 5.2(b). The histogram of q_f clearly deviates from a normal distribution. Rather, the distribution of q_f is asymmetric. This result is consistent with the experimental observation shown in Fig. 5.1. For elevated values of $|q|$ equally good fit results may be obtained by even larger asymmetry parameters. The box plot in Fig. 5.2(c) likewise reflects the asymmetric histogram. The arithmetic mean is 16 (lozenge) and overestimates the true value of $q_g = 15$, while the most frequently observed value of 13 (dot) is lower than q_g. The median (horizontal line) coincides with the true value.

We found that the width of the histogram increased with increasing q_g. This variation is best seen in the collection of q_f histograms plotted in Fig. 5.2(d). While for $q_g \leq 5$ the fit parameters q_f reproduce the true values accurately, the width of histograms appreciably increases for $q_g > 5$. Consequently, the accuracy in determining q_g from fits of Eq. (5.1) to symmetric and peak-like Fano profiles progressively deteriorates with increasing q_g. Indeed, the standard deviation of q_f, $s(q_f)$, approximately varies as q_g^2 [Fig. 5.2(e)]. By contrast, the parameters Γ_f, E_{0f}, $A_f = a_f(1 + q_f^2)$ did not depend on q_g (not shown).

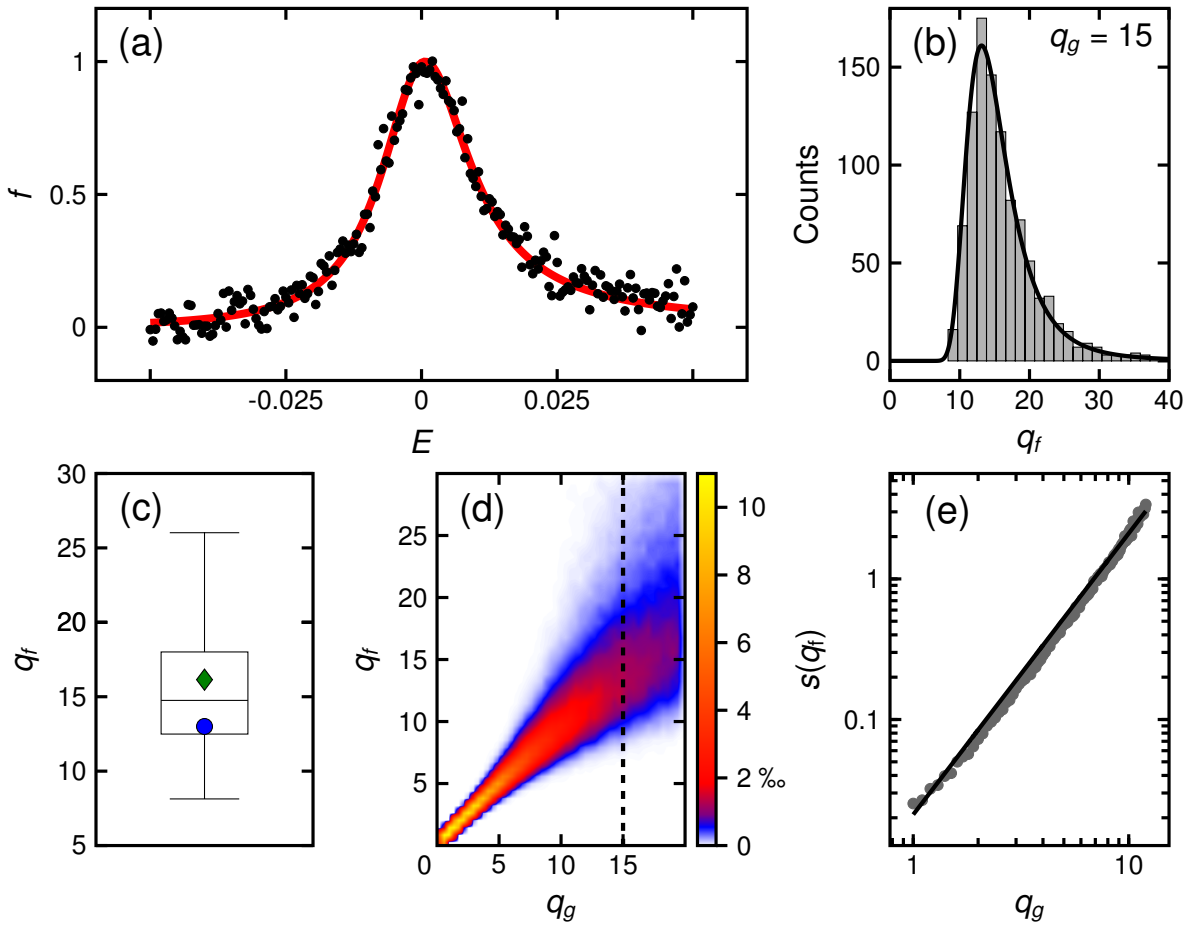

Figure 5.2 (a) Fano line shape f (solid line) obtained from numerically evaluating Eq. (5.2) at equidistantly spaced nodes E_i ($i = 1 \ldots 200$) with $a_g = 1/(1+q_g^2)$, $q_g = 15$, $\Gamma_g = 0.01$, and $E_{0g} = 0$. Scattering of experimental data is mimicked by adding a random number from a normal distribution (zero mean value, standard deviation $\sigma = 0.05$) to the Fano profile at each $E_i \in [-0.05, 0.05]$, which results in the data set depicted as dots in (a). **(b)** Histogram of extracted fit parameters q_f for $q_g = 15$. The full line results from the conversion of normal-distributed α_f to q_f [Eq. (5.7)]. **(c)** Box plot of q_f for $q_g = 15$. The true value (horizontal line inside the box), the mean value (lozenge) and the most probable value (dot) are indicated. **(d)** Collection of q_f histograms obtained from fits of $F(E)$ [Eq. (5.1)] to numerically generated data sets with $1 < q_g < 20$ and the other parameters as in (a). For each histogram 1000 individual fits were performed. **(e)** Logarithmic presentation of the standard deviation of q_f, $s(q_f)$, versus the asymmetry parameter q_g. The full line is a fit to the data, $s(q_f) \approx 0.02\, {q_g}^2$. *This figure was reproduced [91] with permission from AIP.*

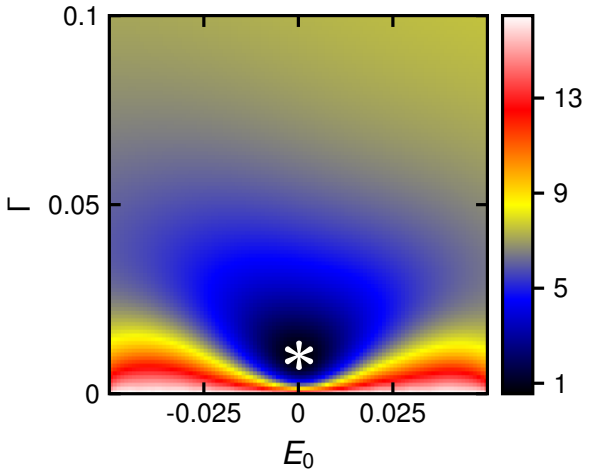

Figure 5.3 Map of χ^2 for a numerically generated spectrum ($a_g = 1/(1+q_g^2)$, $q_g = 15$, $E_{0g} = 0$, $\Gamma_g = 0.01$, and $\sigma = 0.05$) as a function of Γ and E_0. The asterisk indicates the position of the global minimum. The color scale ranges from black (minimum) to white (maximum). *This figure was reproduced [91] with permission from AIP.*

This is fortunate since these parameters contain information about the Kondo temperature, the Abrikosov-Suhl resonance energy and the spatial extension of the Kondo effect, respectively. We further observed that with increasing q_g the fits revealed a dependence on initially guessed fit parameters. Below an improved parameterization of the Fano function is suggested, which reduces the nonlinear part of the optimization to two parameters and is independent of start parameters.

5.3 Improved Parameterization

Equation (5.1) may equivalently be expressed as [142]

$$F(\varepsilon) = k\frac{1}{1+\varepsilon^2} + l\frac{\varepsilon}{1+\varepsilon^2} + m\varepsilon + n \tag{5.4}$$

with $\varepsilon = (E - E_0)/\Gamma$, $k = a(q^2-1)$, $l = 2qa$, $m = b\Gamma$, $n = a + bE_0 + c$. The new parameterization reveals a linear dependence on k, l, m, n, which is advantageous for the least-squares fit. Moreover, the optimization procedure may be performed at two levels,

i. e.,

$$\chi_{\mathrm{f}}^2 = \min_{\Gamma,E_0}\left[\min_{k,l,m,n}\sum_{i=1}^{M}|y_i - F(k,l,m,n,\Gamma,E_0;E_i)|^2\right]. \tag{5.5}$$

The outer nonlinear optimization step is performed in a two-dimensional (Γ, E_0) rather than in a three-dimensional (q, Γ, E_0) parameter space – the parameters (a, b, c) enter linearly into Eqs. (5.1), (5.2). For a given pair (Γ, E_0) the remaining parameters k, l, m, n are obtained by solving the inner linear least-squares problem [Appendix C.1]. Importantly, the resulting χ^2 may be visualized in a two-dimensional plot [Fig. 5.3], which helps to identify the optimum fit result as the global minimum of χ^2 (asterisk in Fig. 5.3). The presence of a global minimum reflects the independence of the fit routine of initially guessed parameters. Moreover, it is close to the true values Γ_{g} and $E_{0\mathrm{g}}$ used for the plot. For the specific pair (Γ, E_0) yielding the global minimum of χ_{f}^2 the fit parameters k_{f}, l_{f}, m_{f}, n_{f} can be extracted. Subsequently, the sought-after asymmetry parameter may be calculated from $q_{\mathrm{f}} = q(k_{\mathrm{f}}, l_{\mathrm{f}})$ with

$$q = \frac{k + \sqrt{k^2 + l^2}}{l}. \tag{5.6}$$

In the following we discuss the uncertainty margin of q, which according to Eq. (5.6) results from the uncertainty margins of k_{f} and l_{f} *via* error propagation. The desirable linear error propagation may be applied if in the Taylor expansion of q with respect to k and l the second-order term and higher-order terms are negligible compared to the first-order term. For $q = q(k,l)$ [Eq. (5.6)] this requirement is not fulfilled. However, for α defined as $\alpha = 2\tan^{-1}(q)$ or, equivalently,

$$q = \tan\left(\frac{\alpha}{2}\right) \tag{5.7}$$

the second-order term is minimized [Appendix C.2]. The transformation of q according to Eq. (5.7) enables a simple interpretation [Fig. 5.4(a)]. The parameters k, l of Fano functions with constant A describe a circle in the kl-plane with radius $A = \sqrt{k^2 + l^2}$. In the

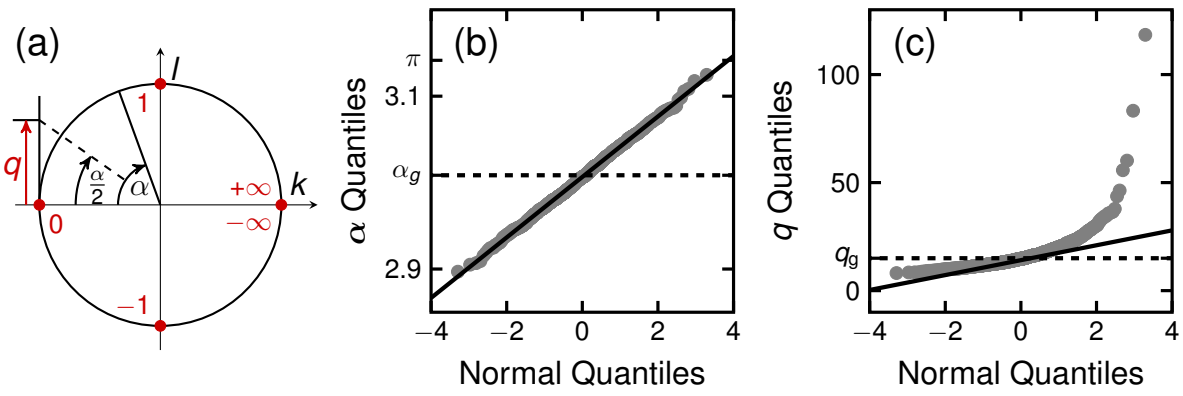

Figure 5.4 (a) Geometric interpretation of q and A in the kl-plane. In the kl-plane the amplitude, $A = \sqrt{k^2 + l^2}$, is the radius of a circle, while q appears as the opposite leg to the angle $\alpha/2$. Dots on the unit circle ($A = 1$) indicate specific values of q, *i. e.*, $q = 0$ for $\alpha = 0$, $q = \pm 1$ for $\alpha = \pm\pi/2$, $q = \pm\infty$ for $\alpha = \pm\pi$. **(b)** Quantile-quantile plot for α (dots) and a normal distribution (full line). α was calculated from q [Fig. 5.2(b)] according to Eq. (5.7). The normal distribution has mean value 3.006 and standard deviation 0.035. The dashed line indicates the true value α_g. **(c)** Same as (b) for q. The full line is a normal distribution with mean value 14.1 and standard deviation 3.45. *This figure was reproduced [91] with permission from AIP.*

special case of the unit circle, *i. e.*, $A = 1$, the asymmetry parameter q appears as the opposite leg to the angle $\alpha/2$. Therefore, we refer to Eq. (5.7) as the angular representation of q.

The quantile-quantile plot shown in Fig. 5.4(b) compares the distribution of $\alpha = 2\tan^{-1}(q)$ for the specific data set of Fig. 5.2(b). The α (dots) and the normal (full line) distributions virtually coincide. Therefore, linear error propagation applies very well for $\alpha(k,l)$, *i. e.*, also higher-order terms in the aforementioned Taylor expansion are negligible compared to the linear term. By contrast, the distribution of q deviates significantly from a normal distribution [Fig. 5.4(c)]. Consequently, we suggest to perform averaging and the determination of standard deviations in the angular representation of q. Corresponding values for q may then be obtained according to the transformation in Eq. (5.7). Figure 5.2(b) shows as a full line the result of this transformation from normal-distributed α to q [Appendix C.3]. The asymmetric histogram [Fig. 5.2(b)] is well reproduced, which corroborates the appropriateness of the transformation.

The standard error s_α of α was calculated *via* linear error propagation [Appendix C.4]. In

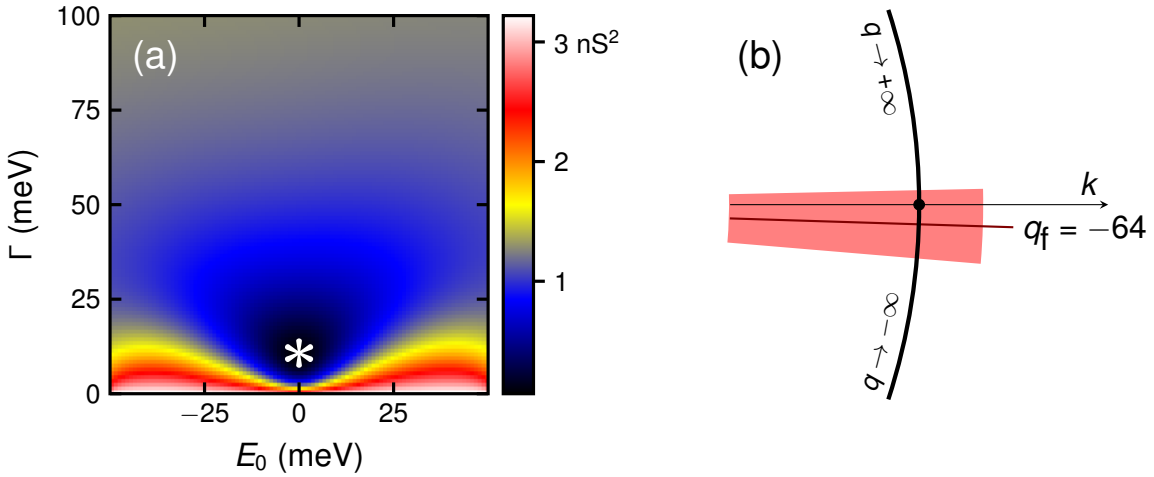

Figure 5.5 (a) Map of χ^2 for the experimental data shown in Fig. 5.1. A global minimum (asterisk) is obtained for $\Gamma = 10.5\,\text{meV}$ and $E_0 = 0\,\text{meV}$. **(b)** Intervals of α with a confidence level of 95 % are depicted as the shaded sector, *i. e.*, $3.142 \geq \alpha \geq \pi$ and $-\pi \leq \alpha \leq -3.079$. Corresponding asymmetry parameters read $q \geq 94$ and $q \leq -24$. *This figure was reproduced [91] with permission from AIP.*

68 % of all data sets we found that $\alpha - s_\alpha \leq \alpha_g \leq \alpha + s_\alpha$, with α_g the true value. Therefore, the proposed determination of uncertainty margins for α_f is reliable. By contrast, uncertainty margins for q, which are derived on the basis of linear error propagation do not reflect the probability distribution of q_f.

We have further tested the improved parameterization of the fit function, Eq. (5.4), and the transformation, Eq. (5.7), using the experimental data set shown in Fig. 5.1. According to Fig. 5.5 the two-dimensional map of χ^2 exhibits a global minimum for $\Gamma = 10.5\,\text{meV}$ and $E_0 = 0\,\text{meV}$. The resulting asymmetry parameter, Eq. (5.6), reads $q = -64$. The confidence interval for the extracted q may readily be calculated by determining the confidence interval of the normal-distributed α and subsequently returning *via* Eq. (5.7) to corresponding confidence levels of q. For a confidence level of 95 % we obtained a confidence region composed of the intervals $3.142 \geq \alpha \geq \pi$ and $-\pi \leq \alpha \leq -3.079$, which corresponds to $q \geq 94$ and $q \leq -24$, respectively. In this particular case the confidence interval contains $\alpha = \pm\pi$, and thus negative and positive asymmetry parameters.

Before concluding we mention that the presented fit algorithm is applicable to all Fano line shapes. Appendix C.5 shows experimental Kondo resonances with the asymmetry

parameter close to unity (asymmetric Fano line shape) and close to zero (symmetric dip).

5.4 Conclusions

Extracting the asymmetry parameter from symmetric and peak-like Fano line shapes is inherently related to considerable uncertainty. An improved parameterization of the Fano fit function enables the optimization and visualization of the sum of squared residuals in a two-dimensional parameter space. The existence of a global minimum in the sum of squared residuals results in the desired independence of start parameters. The sought-after asymmetry parameter is determined by the remaining linear fit parameters alone. An angular representation of the asymmetry parameter follows a normal distribution and enables the determination of uncertainty margins by linear error propagation. Therefore, we propose to, first, determine mean values and confidence regions in the angular representation and, second, convert these quantities back to the asymmetry parameter. This procedure enables the reliable assessment of the fit quality, the sign of the asymmetry parameter as well as the magnitude of error margins. The suggested fit algorithm is applicable to all types of Fano functions.

6 Spectroscopic Line Shapes of Vibrational Quanta in the Presence of Molecular Resonances

Reprinted (adapted) with permission from
The Journal of Physical Chemistry Letters 7, 2388 (2016).

IMAGING with atomic precision, performing spectroscopy of electronic and vibrational excitations with high energy resolution and manipulating matter at the single-atom level belong to the fascinating capabilities of a scanning tunneling microscope (STM). Combining these appealing properties in a single experiment enables the fabrication and examination of archetypical model systems. The impetus to the work presented here was unraveling the potential influence of the tip electronic structure on vibrational signatures in inelastic electron tunneling spectroscopy (IETS). Functionalization of the tip was previously demonstrated to profoundly influence imaging [143–146], spectroscopy of electronic states [147, 148], and magnetic contrast in spin-resolved scanning tunneling microscopy [149–152]. In contrast, the impact of the tip electronic structure on vibrational spectroscopy has scarcely been investigated to date. Various theories of selection rules have been developed [44, 153–155]. However, these theories consider the tip at best in terms of a coupling strength between tip and substrate [44]. The termination of a tip apex with a single CO molecule was included in a generalized transfer Hamiltonian method [156] to describe IETS experiments for CO on Cu(1 0 0) [157]. The calculations [156] showed that by explicitly considering the tip termination the observed inelastic tunneling

efficiencies [157] could be reproduced. Vibrational excitations of isolated CO on Cu(2 1 1) were likewise investigated [158]. Frustrated translational and rotational modes were observed using clean as well as CO-terminated tips. Only the energy of the translational mode shifted to higher energies upon using the CO tip. The energy of the rotational mode was not affected. In another experiment vibrational modes of CO and O_2 adsorbed on Ag(1 1 0) were observed in IET spectra when tips terminated by CO and C_2H_4 were used. These modes were absent in spectra acquired with bare tips [159]. An interpretation of these findings [158, 159] was not reported at that time. Only recently a theoretical study [160] addressed the role of the tip in the specific case of tips terminated by CO and C_2H_4. The emerging picture conveyed in this theoretical work [160] is the maximization of the excitation cross section by the overlap of transport channels with appropriate orbital symmetry. In a recent report the line shapes of CO vibrational modes exhibited an inversion symmetry upon transferring the molecule from the surface to the tip [34]. These findings were rationalized in terms of the difference in strength between the molecule-tip and the molecule-surface coupling [34]. The influence of the geometric tip apex structure on the IET signal strength of CO vibrations on Cu(1 1 1) was recently addressed in a combined STM and atomic force microscopy study [33].

For our investigations we used C_{60}-covered Pb(1 1 1) since all Jahn-Teller active H_g modes contribute to IET spectra, as previously shown [26]. In addition, the lowest unoccupied molecular orbital (LUMO) of C_{60} on Pb(111) covered an energy range that comprised the energies of several vibrational modes [24]. Moreover, individual C_{60} molecules were readily transferred from the surface to the tip, which enabled spectroscopy experiments with C_{60}-terminated tips. The main finding of our study is the marked influence of the LUMO on the line shape of those C_{60} vibrational quanta whose energies lie within the LUMO spectral range. By terminating the tip apex with a single C_{60} molecule exhibiting different adsorption configurations we were able to tune the LUMO energy. Concomitantly, the spectral ranges for vibrational modes with asymmetric line shapes were modified. These results were rationalized in terms of on-resonance and off-resonance tunneling in IETS as predicted theoretically [23, 161, 162]. The impact of molecular resonances on IETS was

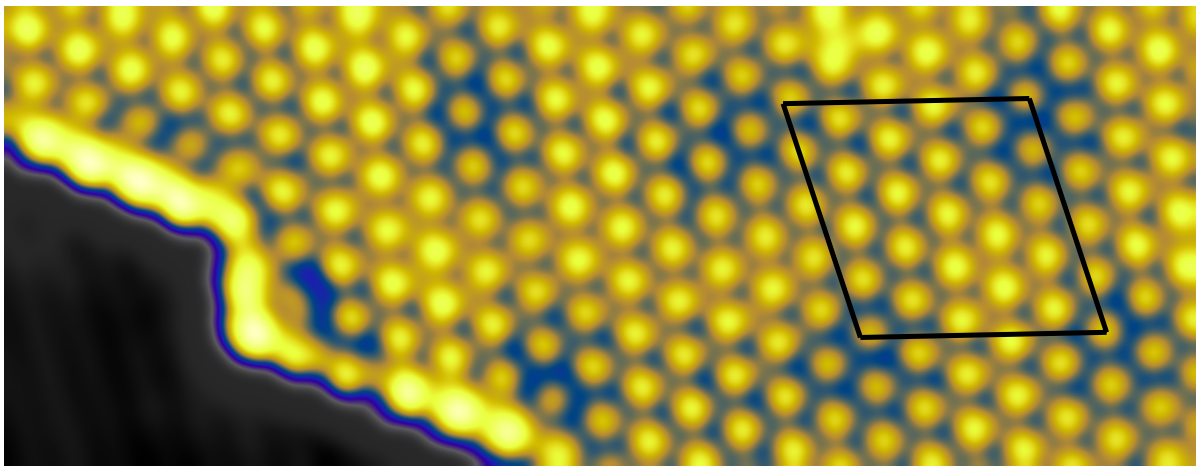

Figure 6.1 Overview STM image of Pb(1 1 1) with adsorbed C_{60} molecules in the submonolayer coverage range ($22 \times 8.5\,nm^2$, 100 mV, 100 pA). Individual C_{60} molecules appear as nearly circular protrusions at this scale and form a hexagonal ordered array. The black lines indicate the unit cell of a moiré lattice present on this surface [27]. *This figure was reproduced [92] with permission from ACS.*

reported from O_2 on Ag(1 1 0) [35]. However, orbital spectroscopic signatures in spectra of the differential conductance (dI/dV) were not presented in that report impeding a clear-cut correlation between affected vibrational excitations and molecular resonances. In subsequent theoretical works the Stoner-type splitting of the O_2 π_g resonance was demonstrated to lead to a partially filled state at the Fermi energy [163, 164], supporting the idea of the on-resonance condition described earlier [23, 161, 162]. In gated molecular junctions modifications of signal strengths and line shapes of vibrational modes were reported to depend on the gate voltage [165]. However, dI/dV spectroscopy of relevant molecular orbitals as well as images of the addressed molecule were not presented. Here, we combined electronic and vibrational spectroscopy in a single experiment, which enabled the unambiguous correlation between line shapes of molecular vibrations and resonant tunneling through orbital resonances.

6.1 Adsorption and Electronic Structure

Figure 6.1 shows an overview STM image of C_{60}-covered Pb(1 1 1). Adsorbed C_{60} molecules formed a hexagonal lattice with a nearest-neighbor distance of 1 nm. In addition, a moiré

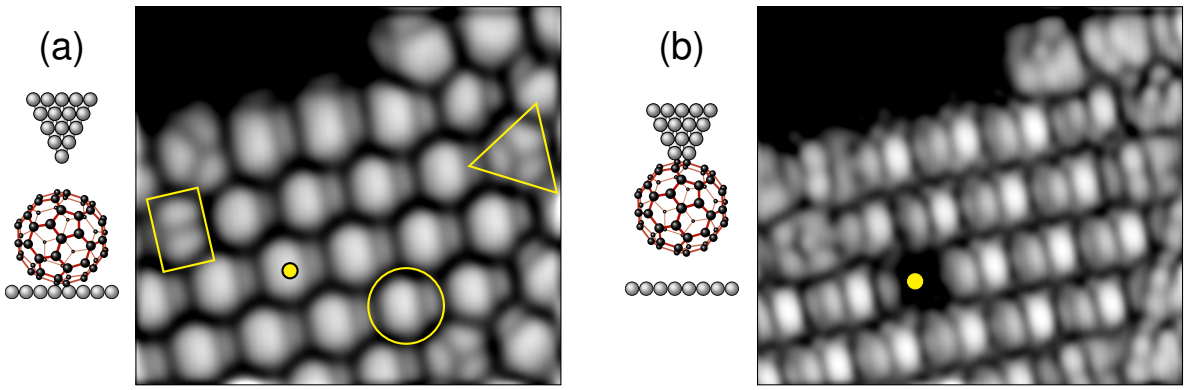

Figure 6.2 (a) Close-up view of a C_{60} island with molecules exposing a C-C bond between two C hexagons (rectangle), a C pentagon (circle), a C hexagon (triangle) towards the vacuum ($5.2 \times 6\,\mathrm{nm}^2$, 210 mV, 1 nA). The dot marks a C_{60} that was transferred to the tip. **(b)** Same as (a) after transferring the C_{60} indicated by the dot in (a) to the tip apex ($5.2 \times 6\,\mathrm{nm}^2$, 210 mV, 100 pA). STM images were processed in order to enhance submolecular contrast [101]. *This figure was reproduced [92] with permission from ACS.*

superstructure was visible with a periodicity of the moiré unit cell of 4.6 nm. The moiré lattice was rotated by $\approx 11^\circ$ with respect to the C_{60} array. Consequently, the observed moiré superstructure corresponds to one of the two previously reported higher-order commensurate structures [27]. A close-up view [Fig. 6.2(a)] shows the presence of C_{60} molecules with different structural motifs. The most frequently observed pattern at a bias voltage of 0.1 V was a nearly circular protrusion, which is due to the C_{60} LUMO centered at the C pentagons [166]. Therefore, these patterns indicated molecules with C pentagons pointing towards the tip, which are referred to as **5**-C_{60} in the following. Clover-like patterns were less frequently observed. They resulted from C hexagons (**6**-C_{60}) exposed to the vacuum [166]. Two adjacent protrusions signaled C_{60} molecules with a C-C bond between two C hexagons (**6** : **6**-C_{60}) oriented towards the vacuum [166].

Single **5**-C_{60} molecules were transferred from the surface to the tip by positioning the tip atop the center of the molecule and increasing the current to values beyond the contact range (on the order of 1 µA at a bias voltage of 200 mV). The successful transfer is illustrated by Figs. 6.2(a), (b). The molecule indicated by the dot [Fig. 6.2(a)] had been removed from the C_{60} array and transferred to the tip. In subsequent STM images acquired with the C_{60}-terminated tip more complex structural motifs of adsorbed molecules

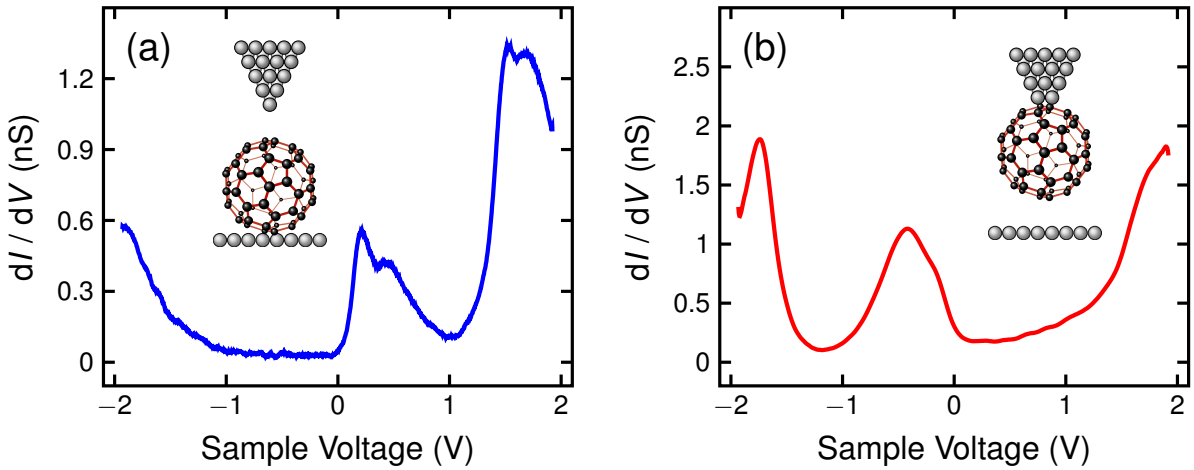

Figure 6.3 dI/dV spectra of tunneling junctions comprising **(a)** a Pb tip and a C_{60} molecule adsorbed on Pb(1 1 1), and **(b)** a C_{60}-terminated tip and bare Pb(1 1 1). Peaks correspond to spectroscopic signatures of molecular resonances (see text). All spectra were obtained after disabling the feedback loop at 2 V, 1 nA. The bias voltage was modulated using $V_{\mathrm{mod}} = 14$ mV and $f_{\mathrm{mod}} = 6.37$ kHz. *This figure was reproduced [92] with permission from ACS.*

appeared [Fig. 6.2(b)]. Comparing these data with calculations [167] the orientation of C_{60} at the tip apex was determined. In the case of Fig. 6.2(b) the apex was terminated by a **6** : **6**-C_{60} molecule.

Depending on the junction composition spectra of dI/dV characteristically changed [Figs. 6.3(a), (b)]. Spectra of adsorbed C_{60} acquired with a bare Pb tip revealed double-peak features at 0.2 V, 0.45 V and at 1.51 V, 1.68 V [Fig. 6.3(a)]. We assign these features to the spectroscopic signatures of the LUMO and the LUMO+1. The splitting may be due to the lifted threefold degeneracy upon adsorption on Pb(1 1 1), as suggested previously [27]. A typical spectrum acquired with a C_{60}-terminated tip on Pb(1 1 1) is presented in Fig. 6.3(b). The unoccupied C_{60} molecular orbitals now appeared at negative bias voltage, as expected [28, 168]. The aforementioned splitting of the LUMO and LUMO+1 for adsorbed C_{60} was less pronounced for the LUMO and nearly absent for the LUMO+1 for the apex molecule. In addition, depending on the C_{60} adsorption configuration at the tip apex, LUMO and LUMO+1 energies varied on the order of 100 meV.

6.2 Vibrational Features

Vibrational spectroscopy of the different junctions represents the main finding of this chapter [Figs. 6.4, 6.5]. Figure 6.4(a) shows a d^2I/dV^2 spectrum that was acquired with a bare Pb tip atop an adsorbed **5**-C_{60} molecule. In agreement with previously reported data [26] the spectrum reveals signatures of $H_g(1),\ldots,H_g(8)$ vibrational modes at 33, 52, 87, 96, 134, 155, 175, 195 mV (black triangles). Rather than a single peak at 67 mV [26] our spectra showed two clearly resolved peaks at 65 mV and 70 mV. These features are attributed to the signatures of, respectively, the $T_{1u}(1)$ and $T_{1u}(2)$ vibrational modes of C_{60} since previous reports revealed energies of 65–66 meV ($T_{1u}(1)$) and 70–73 meV ($T_{1u}(2)$) for these dipole-active modes [71, 74, 75, 80, 169]. Weak features at $\approx \pm 146$ mV may be assigned to the $T_{1u}(3)$ mode while a possible signature of the $T_{1u}(4)$ vibrational mode coincides with $H_g(7)$ [71]. T_{1u} vibrational features are indicated by red triangles. Additionally a faint signature at ±42 mV may be assigned to the hyper-Raman active $T_{3u}(1)$ mode (green triangle) whose energy was reported by inelastic neutron and electron scattering as well as by IETS of planar tunneling junctions in the range 37–44 meV [79, 80, 169].
In the following we concentrate on the line shape of specific signatures of C_{60} vibrational modes and their relation to the position of the LUMO. The LUMO-related spectroscopic feature of C_{60} molecules leading to d^2I/dV^2 spectra presented in Fig. 6.4(a) revealed its maximum at ≈ 180 mV [Fig. 6.4(b)]. The dip-like line profile of the $H_g(7)$ mode at 175 mV [Fig. 6.4(c)] deviates from the commonly observed peak structure, while the indentation at −175 mV [Fig. 6.4(d)] is in accordance with a purely inelastic process. The observation that the feature at 175 mV (−175 mV) lies within (outside) the spectral range of the LUMO, which is indicated by the gray shaded area in Figs. 6.4(a)–(c), hints at the electronic structure of the junction affecting the spectroscopic line shapes of the vibrational modes. At negative bias voltages the highest occupied molecular orbital (HOMO) occurred below −1 V and was thus well separated from the spectral range of C_{60} vibrational excitations.
These experimental observations are reminiscent of previous predictions [23, 161, 162]. In these theoretical works [23, 161, 162] electron tunneling from a tip to an adsorbed molecule was considered. The spectroscopic line shape of a vibrational mode with en-

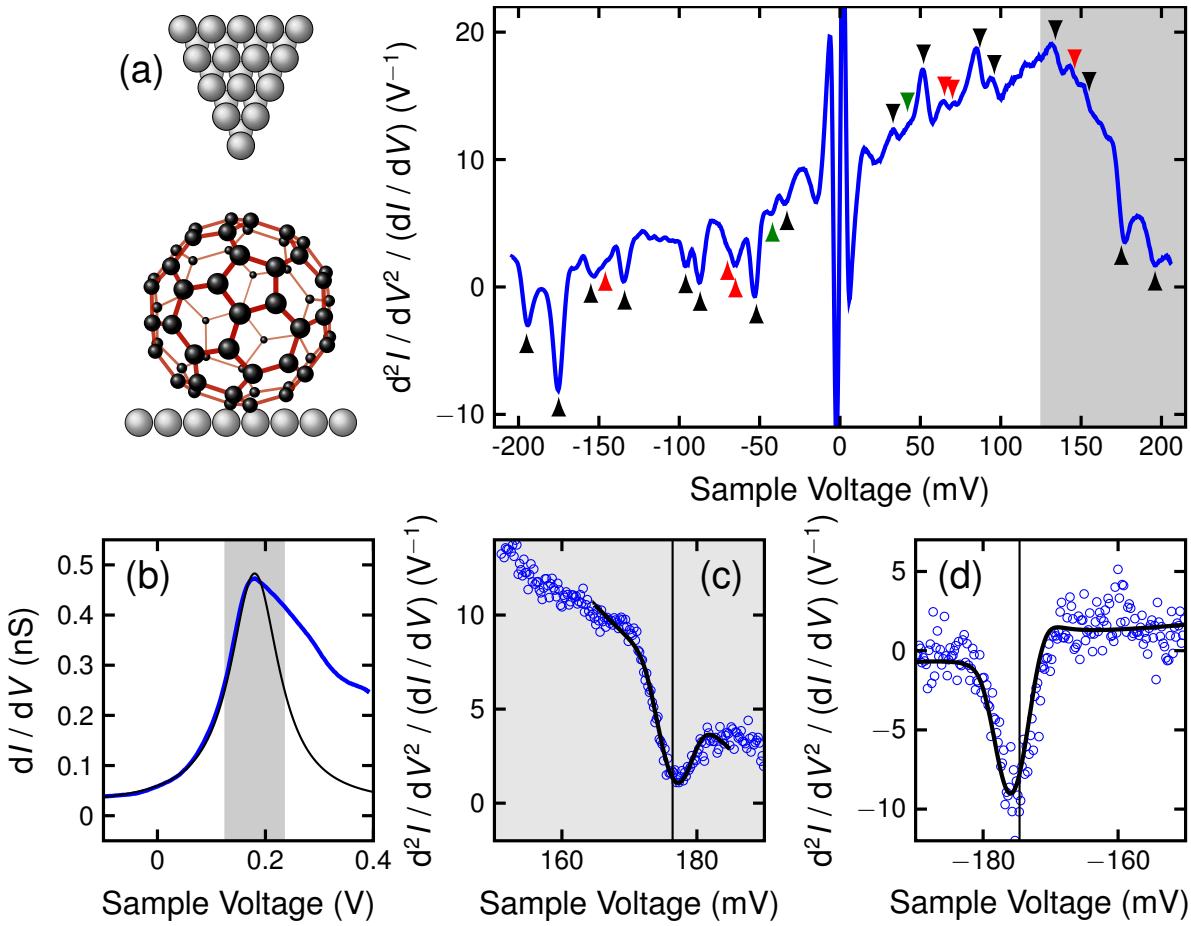

Figure 6.4 (a) Spectrum of $\mathrm{d}^2I/\mathrm{d}V^2\,/\,(\mathrm{d}I/\mathrm{d}V)$ acquired with a Pb tip atop the center of a **5**-C_{60} molecule embedded in a C_{60} island on Pb(1 1 1). The spectrum was composed of four individual spectra covering the voltage ranges $-200\,\mathrm{mV} \leq V \leq -100\,\mathrm{mV}$, $-100\,\mathrm{mV} \leq V \leq 0\,\mathrm{mV}$, $0\,\mathrm{mV} \leq V \leq 100\,\mathrm{mV}$, $100\,\mathrm{mV} \leq V \leq 200\,\mathrm{mV}$. The feedback loop had been disabled at, respectively, $-200\,\mathrm{mV}$, $-100\,\mathrm{mV}$, $100\,\mathrm{mV}$, $200\,\mathrm{mV}$ and 1 nA. The bias voltage was modulated using $V_{\mathrm{mod}} = 4.2\,\mathrm{mV}$ and $f_{\mathrm{mod}} = 950\,\mathrm{Hz}$. An offset between the spectra comprising 100 mV was compensated by a vertical shift of $1.9\,\mathrm{V}^{-1}$. Spectroscopic signatures of H_g, T_{1u}, T_{3u} vibrational modes are indicated by, respectively, black, red, green triangles. The feature centered at zero bias voltage is related to the Bardeen-Cooper-Schrieffer energy gap of Pb(1 1 1). The shaded area depicts parts of the LUMO spectral range. **(b)** $\mathrm{d}I/\mathrm{d}V$ spectrum (blue) of the same junction (feedback loop parameters: 2 V, 1 nA, modulation: $V_{\mathrm{mod}} = 14\,\mathrm{mV}$, $f_{\mathrm{mod}} = 6.37\,\mathrm{kHz}$).. The black line represents a Lorentzian describing the low-voltage part of the LUMO feature centered at 180 mV. The shaded area spans a voltage range defined by the full width at half maximum of the Lorentzian (110 mV). **(c), (d)** $\mathrm{d}^2I/\mathrm{d}V^2\,/\,(\mathrm{d}I/\mathrm{d}V)$ data (circles) of the $H_g(7)$ vibrational mode at positive (c) and negative (d) bias voltage. The full lines are fits to the data on the basis of Eq. (6.1). The vertical lines indicate the bias voltages corresponding to the vibrational energies extracted from the fit routine. *This figure was reproduced [92] with permission from ACS.*

ergy $\hbar\omega$ ($\hbar = h/2\pi$, h: Planck's constant) was demonstrated to depend on its vicinity to a molecular resonance with energy E_M and full width at half maximum (FWHM) Γ_M. For $|\hbar\omega - E_M| \gg \Gamma_M/2$ the vibrational mode was predicted to appear as a peak (dip) in d^2I/dV^2 spectra at positive (negative) bias voltage. This situation corresponds to the off-resonant condition and reflects the most commonly reported observations [24, 30, 170–173]. The on-resonance case is obtained for $|\hbar\omega - E_M| \approx \Gamma_M/2$ where the line shape was shown to adopt an asymmetric profile that gradually evolved into a dip at $\hbar\omega = E_M$. To understand these line shape variations, signals in IETS may be considered being due to electron tunneling in inelastic and elastic transport channels. The inelastic channel gives rise to a step-like increase of dI/dV at the threshold voltage $\pm\hbar\omega/e$ (e: elementary charge) and leads to the commonly observed dips and peaks in d^2I/dV^2 spectra at, respectively, the negative and positive threshold voltage. The elastic channel is influenced by the emission and re-absorption of virtual vibrations at $\pm\hbar\omega/e$ [153, 154], which leads to a step-like decrease in dI/dV and logarithmic terms [162]. The experimentally observed line shape in IET dI/dV spectra reflects then the superposition of step-like decreases and increases together with the influence of the logarithmic terms.

Describing the molecular resonance as a Lorentzian with energy E_M and width Γ_M the resulting (normalized and background-subtracted) dI/dV signal of the vibrational quantum at $\hbar\omega$ was calculated as [23, 161, 162]

$$\frac{dI}{dV} = 1 + u\,\frac{\left[(\hbar\omega - E_M)^2 - \left(\frac{\Gamma_M}{2}\right)^2\right]\Theta(eV - \hbar\omega) - (\hbar\omega - E_M)\frac{\Gamma_M}{\pi}\ln\left|\frac{eV-\hbar\omega}{\Delta}\right|}{\left[E_M^2 + \left(\frac{\Gamma_M}{2}\right)^2\right]\left[(\hbar\omega - E_M)^2 + \left(\frac{\Gamma_M}{2}\right)^2\right]} \tag{6.1}$$

with u containing information about the electron-phonon coupling parameter, Θ the Heaviside step function and $\Delta \ll \Gamma_M$ a cutoff energy.

The effect of the LUMO on the line shapes of vibrational excitations was most clearly observed for the $H_g(7)$ mode shown in Figs. 6.4(c), (d). To this end the low-voltage region of the LUMO was described by a Lorentzian centered at 180 mV and with a FWHM of 110 mV (black line in Fig. 6.4(b)). The full lines in Figs. 6.4(c), (d) are fits of the numerical derivative of Eq. (6.1) convoluted with thermal and instrumental broadening functions

to the experimental data. Details of the fit routine are described in Appendix D.1. The vibrational energy extracted from the fit was $\hbar\omega = 175 \pm 1\,\mathrm{meV}$, which is in excellent agreement with our $\mathrm{d}^2I/\mathrm{d}V^2$ spectra and a previous report [26]. Consistently with the theoretical prediction [23, 161] the spectroscopic signature of the $H_g(7)$ mode adopted a dip-like line shape for voltages well within the spectral range of the C_{60} LUMO (shaded areas in Figs. 6.4(a)–(c)). For negative voltages,*i. e.*, outside the LUMO spectral range, the expected off-resonant indentation was obtained. The line shapes of the remaining vibrational modes were equally well described by Eq. (6.1). A transition from a dip-like to a peak-like line shape *via* an asymmetric line shape was observed with increasing separation from the LUMO energy. In Appendix D.2 spectral data and fit results are presented for the remaining vibrational modes.

6.3 Tuning Line Shapes by Tip Functionalization

Additional experiments were conducted in order to corroborate the mechanism proposed in Sec. 6.2. To this end the tunneling junctions were tailored by single-molecule manipulation. Figure 6.5(a) shows two vibrational spectra acquired with C_{60}-terminated tips on bare Pb(1 1 1). In addition to the vibrational signatures of adsorbed C_{60} [Fig. 6.4(a)] a faint signal appears at 81 mV, which may be related to the previously reported $T_{3u}(2)$ mode [80]. The different spectra (*A*, *B*) resulted from different adsorption configurations of C_{60} at the tip apex, which was likewise reflected by the different LUMO positions in $\mathrm{d}I/\mathrm{d}V$ spectra (spectra A', B' in Fig. 6.5(b)). It was previously shown that the LUMO energy of C_{60} depends on the molecule-substrate interaction [174], the surface orientation [175] as well as on the molecular adsorption orientation [81, 176]. Importantly, by variation of the C_{60} adsorption geometry the overlap of the LUMO spectroscopic signature and the vibrational energy range was altered. The tip configuration leading to spectrum *A* [Fig. 6.5(a)] gave rise to a LUMO signature whose low-energy tail revealed overlap with vibrational energies ($\mathrm{d}I/\mathrm{d}V$ spectrum labeled A' in Fig 6.5(b)). In contrast, tips leading to spectrum *B* exhibited significantly less overlap of the LUMO with the energy range of C_{60} vibrational

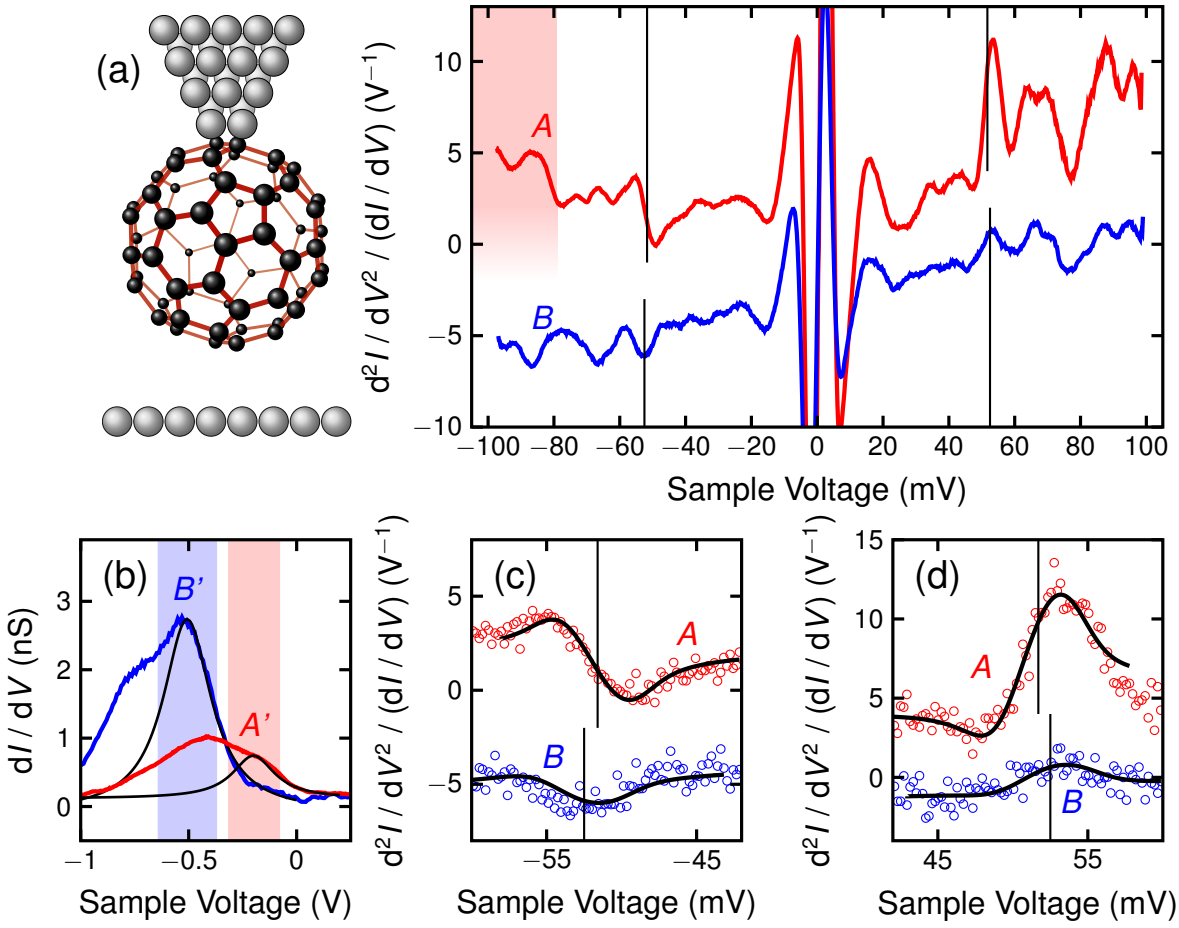

Figure 6.5 (a) Spectra of $\mathrm{d}^2I/\mathrm{d}V^2\,/\,(\mathrm{d}I/\mathrm{d}V)$ acquired with C_{60}-terminated Pb tips above bare Pb(1 1 1). Spectrum *A* was composed of two individual spectra covering the voltage ranges $-100\,\mathrm{mV} \leq V \leq 0\,\mathrm{mV}$, $0\,\mathrm{mV} \leq V \leq 100\,\mathrm{mV}$. The feedback loop had been disabled at, respectively, $-100\,\mathrm{mV}$, 100 mV and 1 nA. For spectrum *B* the feedback loop hat been disabled at $-100\,\mathrm{mV}$, 1 nA. The bias voltage was modulated using $V_{\mathrm{mod}} = 4.2\,\mathrm{mV}$ and $f_{\mathrm{mod}} = 950\,\mathrm{Hz}$. Spectra *A* and *B* result from tips with different C_{60} adsorption configurations at the apex, which are likewise reflected by different LUMO energies. Vibrational signatures whose spectroscopic line shapes are analyzed are indicated by vertical lines. The shaded areas depict parts of the LUMO spectral range. **(b)** $\mathrm{d}I/\mathrm{d}V$ spectra (blue and red lines) of the same junctions (feedback loop parameters: 2 V, 1 nA, modulation: $V_{\mathrm{mod}} = 14\,\mathrm{mV}$, $f_{\mathrm{mod}} = 6.37\,\mathrm{kHz}$). Spectra A', B' correspond to spectra *A*, *B* in (a), respectively. The black lines represent Lorentzians describing the low-voltage part of the LUMO features centered at $-197\,\mathrm{mV}$ (A') and $-506\,\mathrm{mV}$ (B') with fwhm of 236 mV (*A*) and 270 mV (*B*). **(c), (d)** $\mathrm{d}^2I/\mathrm{d}V^2\,/\,(\mathrm{d}I/\mathrm{d}V)$ data (circles) of the $H_g(2)$ vibrational mode at negative (c) and positive (d) bias voltage acquired with the different C_{60}-terminated tips (*A*, *B*). The full lines are fits to the data on the basis of Eq. (6.1). The vertical lines indicate the bias voltages corresponding to the vibrational energies extracted from the fit routine. *This figure was reproduced [92] with permission from ACS.*

modes ($\mathrm{d}I/\mathrm{d}V$ spectrum labeled B' in Fig. 6.5(b)). At positive bias voltages no C_{60} orbital overlapped with the spectral range of vibrational modes [Fig. 6.3(b)].

To demonstrate the effect of the different overlap on the line shapes of vibrational signatures most clearly we discuss the example of the $H_g(2)$ mode appearing at ±52 mV. The line shapes of vibrational modes at ±65 mV, ±70 mV, ±87 mV were similarly affected. Spectral data of these modes and fits are presented in Appendix D.2. At −52 mV the $H_g(2)$ mode adopted an asymmetric line shape in spectrum A, while its spectroscopic profile was a virtually symmetric indentation in spectrum B [Fig. 6.5(c)]. The counterparts at 52 mV appeared with an almost symmetric peaked line shape in both spectra [Fig. 6.5(d)]. Fits (full lines in Figs. 6.5(c), (d)) based on Eq. (6.1) are in good agreement with the experimental data. Lorentzians centered at −197 mV with a FWHM of 236 mV for A' and centered at −506 mV with a FWHM of 270 mV for B' were used to describe the low-voltage range of the spectroscopic LUMO signatures A' and B' (black lines in Fig. 6.5(b)). In both cases the extracted vibrational energies were in good agreement with the experimental data ($\hbar\omega = 51.6$ meV for A' and $\hbar\omega = 52.5$ meV for B', vertical lines in Figs. 6.5(a), (c), (d)).

Before concluding we remark that the observed width of vibrational signatures mainly arose from the thermal and instrumental broadening. Moreover, no changes in the width were observed for resonant and off-resonant tunneling. In addition, in Eq. (6.1) the vibrational mode is characterized by its energy alone. Therefore, we were not able to infer changes in the peak widths. Clearcut statements on possible changes in the $\mathrm{d}^2I/\mathrm{d}V^2$ signal strengths due to resonant or off-resonant inelastic electron tunneling are impeded by the presence of a multitude of overlapping vibrational signatures together with strongly differing line shapes in the resonant and off-resonant cases.

6.4 Conclusions

In conclusion, spectroscopic line shapes of C_{60} vibrational modes are affected by C_{60} molecular orbitals. The overlap of vibrational and orbital energy ranges leads to deviations from the commonly observed dips and peaks in inelastic electron tunneling spectra. Rather, asymmetric line shapes and peak-to-dip conversions appear depending on the degree of overlap. The findings represent an experimental proof to the previously predicted impact of resonant tunneling on inelastic processes at the single-molecule level.

7 Impact of the Molecule Position on Vibrational Line Shapes

Inelastic features in current-voltage characteristics of single molecules have gained increasing attention in the past [33, 34, 36, 39, 177]. These signatures offer a promising route to chemical sensitivity of the scanning tunneling microscope (STM). Depending on the energetic structure and the geometry of the junction, the commonly acquired $\mathrm{d}^2I/\mathrm{d}V^2$ spectra exhibit peaks, dips or asymmetric line shapes. To understand the mechanisms behind the line shape, intensity, and energy of vibrational features, molecules have been studied in different transport regimes. Molecules were contacted between two metallic electrodes [37–39] and have been examined in tunneling experiments [30–36]. For most systems $\mathrm{d}^2I/\mathrm{d}V^2$ spectra exhibited characteristic antisymmetric pairs of respectively a peak at positive voltage and a dip at negative voltage for each vibrational energy [31–34]. These spectra can be rationalized in terms of opening of an inelastic channel due to the emission of a vibrational quantum [23, 44]. However, features were reversed for small molecules between Pt electrodes [177–179], in Au atomic chains [180] and at O_2 molecules adsorbed to the Ag(1 1 0) surface [35, 36]. Here peaks were present at negative voltages, while dips were found for positive voltages. Such observations may result from elastic backscattering due to the electronic structure of the junction [23, 35] or strong electrode-molecule coupling [44, 181]. Additionally, IET spectra were reported which exhibited all types of line shapes [92, 165, 182, 183]. In some of these experiments line shapes were deliberately modified by orbital gating [165], by adsorbing the molecule to a STM tip [92], and by approaching a STM tip [183].

To study the evolution between contact and tunneling IET spectra, distance-dependent measurements are a useful tool. However, reports showing IETS in both conductance

regimes are scarce [26, 40, 41]. An alkanethiol self-assembled monolayer on Au(1 1 1) was examined using a STM. IET spectra were essentially the same in both conductance regimes [40]. In another report STM-IETS measurements were carried out at single CO molecules adsorbed to the Cu(1 1 1) surface [41]. While a conductance increase lead to shifts of the vibrational energies, IET features always appeared as peaks at positive voltages [41]. Remarkably, IET spectra at C_{60} on Pb(1 1 1) showed signatures of all Jahn-Teller active H_g modes [26]. In the cited report line shapes were independent of conductance and showed peaks (dips) at positive (negative) voltages [26]. However, in the experiments shown in Secs. 6.2, 6.3 (published in Ref. [92]) tunneling regime spectra exhibited dip-like and asymmetric features as well. The line shapes were related to properties of the lowest unoccupied molecular orbital (LUMO). No experimental effort was undertaken to examine the reasons for differences between both reports. However, vibrational line shape variations across the surface can be expected, since the LUMO binding energy depends on the adsorption site [27]. The clear connection between the electronic structure and vibrational line shapes has been shown for tunneling spectra so far. An analysis of this phenomenon for high-conductance spectra is missing to date. In a previous report about C_{60} on Cu(1 1 1) the LUMO has been shown to shift towards the Fermi level at increasing conductance. A similar shift for C_{60} on Pb(1 1 1) could affect vibrational line shapes. However, theoretical predictions indicate symmetries of the junction composition to be crucial to vibrational line shapes [43, 44].

Here, we show site-dependent as well as tip height-dependent $\mathrm{d}I/\mathrm{d}V$ and $\mathrm{d}^2I/\mathrm{d}V^2$ spectra at C_{60} molecules adsorbed to a Pb(1 1 1) surface. The LUMO binding energy varies between C_{60} adsorption sites. Coincidently, vibrational line shapes in IETS are affected, similar to the results shown in Secs. 6.2, 6.3. When the tip is approached towards a C_{60} molecule the LUMO feature in $\mathrm{d}I/\mathrm{d}V$ spectra shifts towards lower energies. High-energy vibrational features at positive voltages undergo a dip-to-peak conversion between tunneling and contact regime. In contact all H_g vibrational signatures are present as peaks. By considering the C_{60} position inside the tunneling junction, a qualitative explanation of the experimental data is obtained.

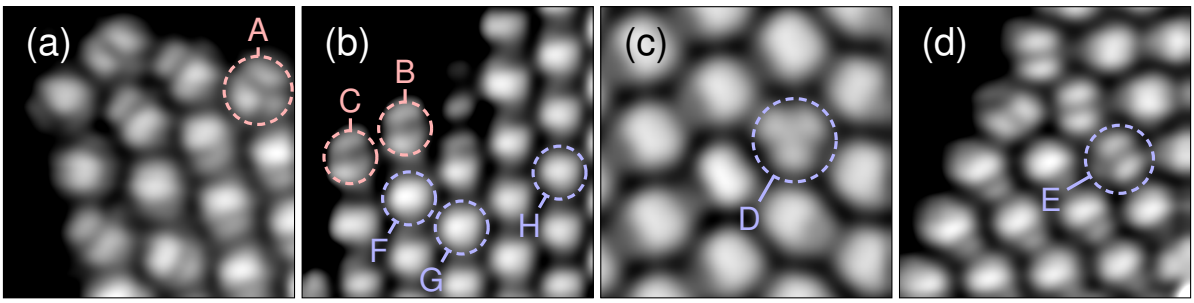

Figure 7.1 Constant-current topographic images across C_{60} monolayer islands. Feedback parameters were $I = 1$ nA and (a) $V = -170$ mV, (b)–(d) $V = 210$ mV. Image sizes are (a) $4 \times 4\,\mathrm{nm}^2$, (b) $5 \times 5\,\mathrm{nm}^2$, (c) $3.2 \times 3.2\,\mathrm{nm}^2$, and (d) $4.5 \times 4.5\,\mathrm{nm}^2$. Analyzed molecules are marked with dashed circles and named A–H. Molecules A–C (red) are adsorbed to a step edge, molecules D–H (blue) are adsorbed well on top of a terrace. C_{60} are adsorbed in various rotational states **5** (F–H), **6** (A, D), and **6** : **6** (C, B, E) [see text].

7.1 Adsorption Site

We first focus on the variation of $\mathrm{d}I/\mathrm{d}V$ and $\mathrm{d}^2I/\mathrm{d}V^2$ spectra depending on the C_{60} adsorption site. Figures 7.1(a)–(d) show topographic maps of C_{60} hexagonal monolayer islands. Molecules close to a step edge[1] (A–C) as well as molecules separated > 1 nm from steps (D–H) were examined. The molecules exhibited various C_{60} rotational orientations, where a C-pentagon (**5**-C_{60} molecules F, G, H), a C-hexagon (**6**-C_{60} molecules A, D), or a C-C bond (**6** : **6**-C_{60} molecules C, B, E) points towards the vacuum.

Constant height $\mathrm{d}I/\mathrm{d}V$ tunneling spectra were recorded atop each of the molecules [Fig. 7.2(a)]. Molecules adsorbed at a step edge exhibited higher energies of the low-energy LUMO peak (molecules A–C, red) than molecules atop a terrace (molecules D–H, blue). The molecular rotational state had some effect on the high-energy parts of the LUMO for C_{60} adsorbed to the terrace. **5**-C_{60} (molecules F–H) exhibited a strong peak at ≈ 200 meV and a less intense peak at ≈ 400 meV. At **6**-C_{60} and **6** : **6**-C_{60} both peaks were equally strong (molecules D, E).

Results shown in Secs. 6.2, 6.3 indicate a crucial connection between the rising edge of the low-energy LUMO (LE-LUMO) part and vibrational line shapes in additionally obtained $\mathrm{d}^2I/\mathrm{d}V^2$ spectra. Based on those investigations [Secs. 6.2, 6.3], we fit the rising edge of

[1] The C_{60} layer continues below the step. To resolve the LUMO structure of the molecule, the lower part of the layer is omitted in the image.

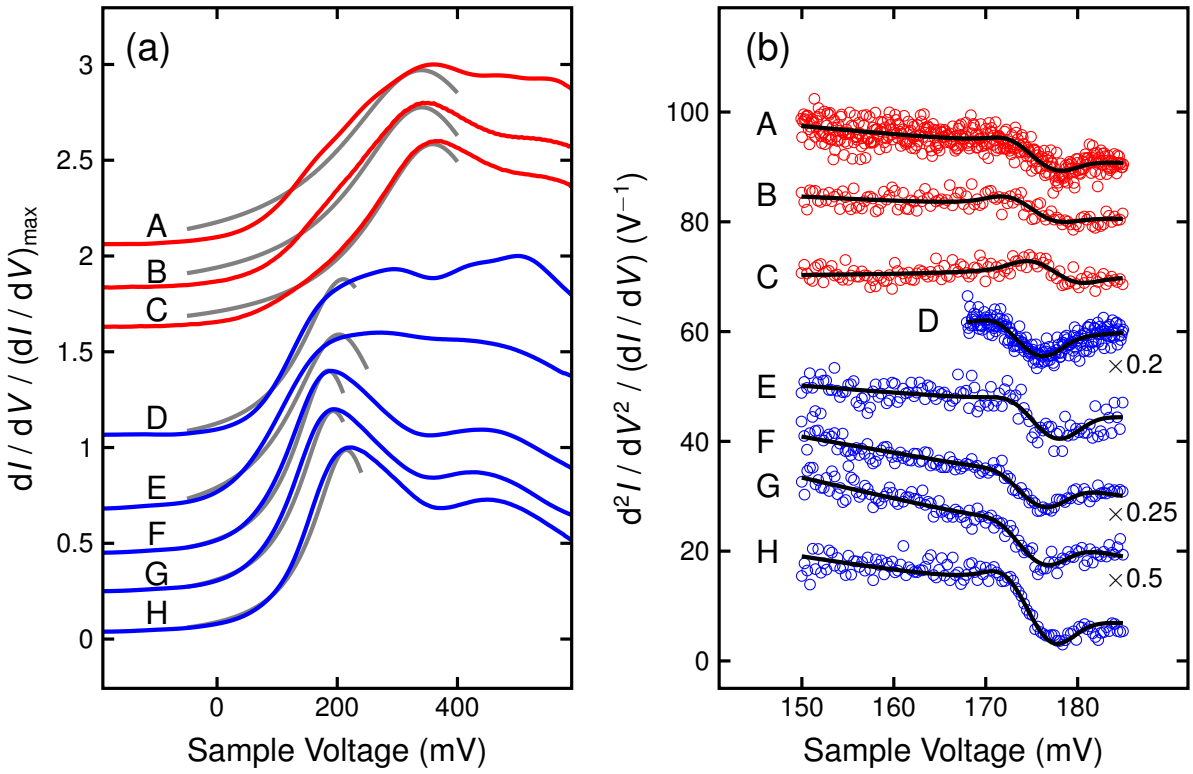

Figure 7.2 (a) dI/dV spectra (red, blue lines) atop molecules (A–H) shown in Fig. 7.1. Feedback loop was opened at 1 nA, and 600 mV (molecules A–D) or 210 mV (molecules E–H). The lock-in modulation amplitude was set to $V_{\mathrm{mod}} = 4.24$ mV with a modulation frequency $f_{\mathrm{mod}} = 3.2$ kHz. Gray lines indicate Lorentzian fits to the rising edge of the respective low-energy LUMO peak. Spectra were normalized to the respective maximum of each curve. **(b)** IET spectra (circles) recorded atop the same molecules (A–H). Prior to each spectrum the feedback loop was opened at 1 nA and 210 mV. The bias voltage was modulated with an amplitude $V_{\mathrm{mod}} = 4.24$ mV and frequency $f_{\mathrm{mod}} = 3.2$ kHz. Black lines show fits of the experimental data using Eq. (6.1) where Γ_{M} and E_{M} are taken from the Lorentzian fits of the respective dI/dV data shown in (a). Spectra were offset for clarity.

the LE-LUMO peak with a Lorentzian function. The fits yield the energy of the LE-LUMO maximum E_{M} and the full width at half maximum Γ_{M} of the LE-LUMO peak. Molecules adsorbed onto a terrace exhibited $E_{\mathrm{M}} \approx 200$ meV and 100 meV $< \Gamma_{\mathrm{M}} <$ 200 meV . Molecules at surface steps showed values at $E_{\mathrm{M}} \approx 350$ meV and 200 meV $< \Gamma_{\mathrm{M}} <$ 330 meV. The site-dependent LE-LUMO energies may be related to varying charge-transfer to the C_{60}[175] and to variations in the local screening properties [27]. For instance, higher molecule-surface distance has been related to higher-lying LUMO energies of C_{60} on Pb(1 1 1) [27]. For molecules A, B significant deviations were found between the fit and the experimental

Molecule	E_M (meV)	Γ_M (meV)	$\hbar\omega$ (meV)	Orientation	Site
A	340	321	174.4	**6**	s
B	341	279	174.9	**6** : **6**	s
C	359	255	177.3	**6** : **6**	s
D	210	172	174.8	**6**	t
E	203	199	177.1	**6** : **6**	t
F	185	137	175.9	**5**	t
G	193	137	175.6	**5**	t
H	215	135	175.6	**5**	t

Table 7.1 LE-LUMO Parameters E_M and Γ_M as extracted from fits of dI/dV data shown in Fig. 7.2(a) acquired atop C_{60} molecules (A–H) [Fig. 7.1]. Vibrational energies $\hbar\omega$ were extracted from fits of IETS data shown in Fig. 7.2(b) on the basis of Eq. (6.1). The rotational orientation and the adsorption site (s: at a step edge, t: well on top of a terrace) of each molecule are indicated.

data. The impact on fits of vibrational features in IET spectra is discussed below.

Atop each examined molecule constant height d^2I/dV^2 tunneling spectra were recorded [Fig. 7.2(b)]. The spectrum voltage range was chosen around the $H_g(7)$ mode signature (175 meV) for its high intensity and its expectable sensitivity to LUMO variations [see Sec. 6.3]. Vibrational features were fit on the basis of Eq. (6.1). Resulting fits nicely reproduce the experimental data [Fig. 7.2(b)]. Vibrational energies are extracted at $\hbar\omega = (175.7 \pm 1.5)$ meV. A list of E_M, Γ_M, and $\hbar\omega$ for each molecule is given in Table 7.1. It may be noted, deviations from a Lorentzian shape (molecules A, B) reduced the quality of the fit significantly [Appendix E.1]. In cases, where a Lorentzian well approximated the LE-LUMO part (molecules C–H) the experimental data was best fit with E_M, Γ_M.

In summary, the IETS line shape of the $H_g(7)$ mode of C_{60} on Pb(1 1 1) was essentially determined by the LE-LUMO parameters E_M, Γ_M, as extracted from dI/dV data. These parameters vary depending on the adsorption position. The shown results support the findings in Sec. 6.3 where LE-LUMO parameters were intentionally tuned by functionalizing the tunneling tip. Additionally, molecules adsorbed to a step edge exhibited peak-like IETS features of the $H_g(7)$ mode [molecules B, C, Figs. 7.1(b), 7.2(b)], as reported previously [26].

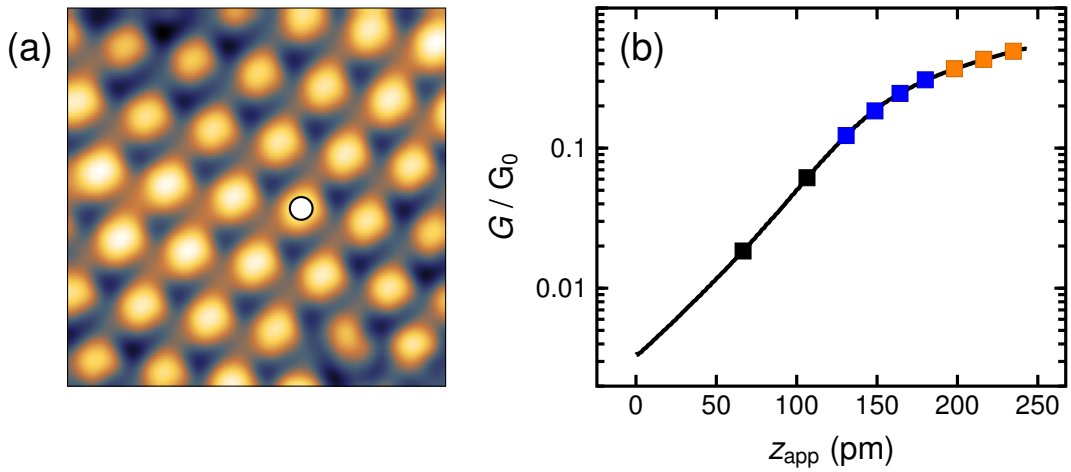

Figure 7.3 (a) Constant current topographic map of a C_{60} monolayer island on Pb(1 1 1) (1 nA, 210 mV, 4.7×4.7 nm^2). A **5**-C_{60}embedded within **5**-C_{60} molecules is studied (white dot). **(b)** Conductance across the junction G as the tip is approached z_{app} towards the molecule. $z_{app} = 0$ is defined by $I = 50$ nA, $V = 210$ mV. Squares mark conductances at which the feedback loop was disabled prior to the acquisition of dI/dV and d^2I/dV^2 spectra shown in Figs. 7.4, 7.5. Colors indicate the transport regimes tunneling (black), contact (orange) and intermediate (blue).

7.2 Junction Symmetry

In the following we discuss dI/dV and d^2I/dV^2 spectra atop a C_{60} molecule at varying tip-sample distance Figure 7.3(a) shows a topographic map of a hexagonal C_{60} layer. A **5**-C_{60} (white dot) embedded within the monolayer and well separated from a Pb(1 1 1) step edge was chosen for examination. The tip was held atop the molecule with the conductance yielding $\approx 0.02\,G_0$ ($G_0 \approx 77.5\,\mu$S). The tip was then pushed towards the sample [Fig. 7.3(b)], while the current though the junction was monitored. The bias voltage was kept constant. In tunneling regime[2] ($z_{app} < 120$ pm) the conductance $G = I/V$ increased exponentially with decreasing tip-sample distance. A similar, but weaker, exponential increase was found in contact regime ($z_{app} > 200$ pm). In the intermediate regime ($120\,\text{pm} < z_{app} < 200\,\text{pm}$) a smooth transition was measured, in accordance with previously published data [26].

[2]The tunneling regime and the contact regime were defined as those parts of the curve where linear functions well-described $\ln\left(G(z_{app})\right)$. The region in-between was ascribed to an intermediate regime, where the increased curvature impeded a linear description over distances > 50 pm.

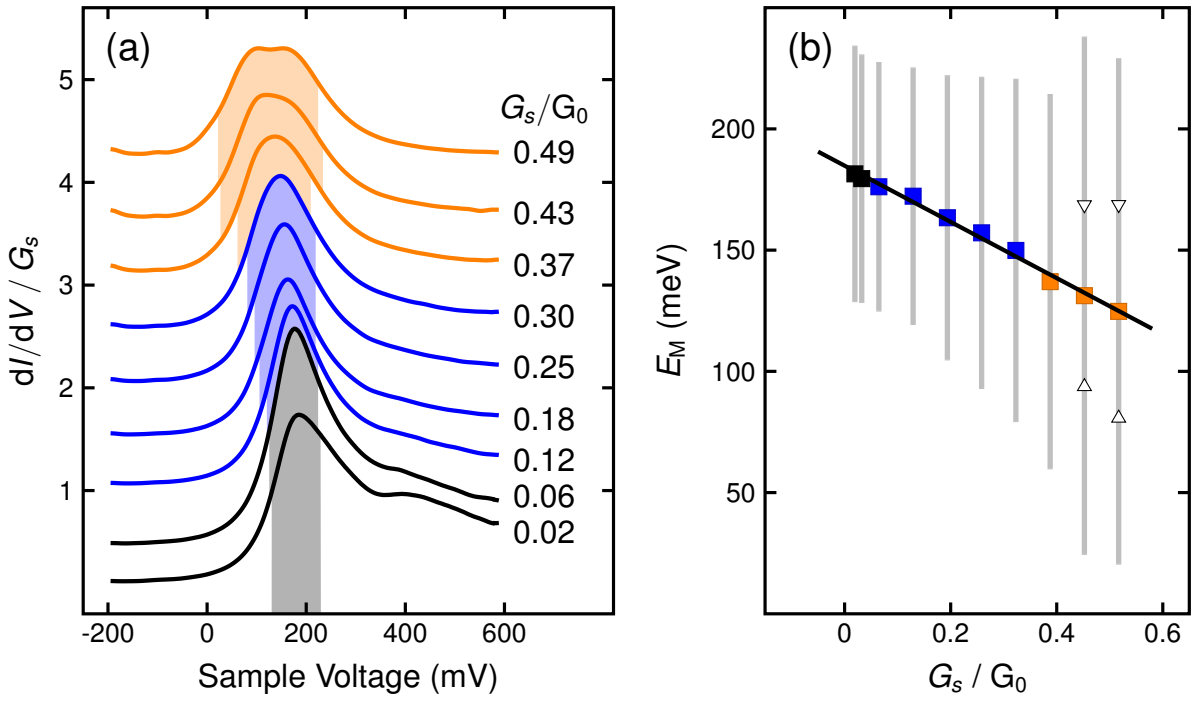

Figure 7.4 (a) dI/dV spectra (lines) acquired with the feedback loop disabled at the conductances indicated in Fig. 7.3(b). ($V = 210\,\mathrm{mV}$, $I = 0.3, 1 - 8\,\mu\mathrm{A}$, $V_{\mathrm{mod}} = 4.24\,\mathrm{mV}$, $f_{\mathrm{mod}} = 3.2\,\mathrm{kHz}$). The respective setpoint conductance is labeled to the right of each curve. Shaded areas indicate the respective voltage range which is covered by the low-energy LUMO part. Colors are chosen as in Fig. 7.3(b). Spectra were offset for clarity. **(b)** Energy of the low-energy LUMO peak (dots) as a function of the conductance at the instant of disabling the feedback loop prior to spectroscopy. In contact the peak splits [see (a)]; here dots denote the average of both peak energies (triangles). A fit to the data (solid line) suggests $E_{\mathrm{M}}/\mathrm{meV} \approx 185 - 159\,G_s/\mathrm{G}_0$. Vertical lines indicate the energy range covered by the lowest energy part of the LUMO as shown in (a).

Changing the tip-sample distance is accompanied by a variation of spectral features in dI/dV. Figure 7.4(a) shows dI/dV spectra at differing tip-sample distance. Prior to spectroscopy the feedback loop was disabled at the setpoint conductances G_s indicated in Fig. 7.3(b) (squares). Between the acquisition of spectra current-distance curves and topographic images were recorded to ensure constant tip and molecule conditions. In tunneling regime the previously reported [26, 92] two-peak feature (180 meV, 400 meV) is well resolved (lowest curve). Upon increasing G_s the 400 meV peak decreased in intensity, and vanished eventually. The peak's energy remained essentially constant [see Ap-

pendix E.2]. The energy of the low-energy LUMO peak E_M decreased linearly with increasing G_s [Fig. 7.4(b)]. The LE-LUMO width Γ_M increased upon approaching the molecule. The energy range between $E_M \pm \Gamma_M/2$ is shown as shaded areas in Fig. 7.4(a) and as vertical lines in Fig. 7.4(b). While the lower bound $E_M - \Gamma_M/2$ approached zero, the upper bound $E_M + \Gamma_M/2$ remained approximately constant for all setpoint conductances. In contact regime the low-energy peak splitted. The energy distance between both components increased with increasing conductance.

For tunneling data, splitting of the C_{60} LUMO was previously ascribed to the removal of the threefold degeneracy upon adsorption to the metal substrate [27, 175]. Splitting and energy of the LUMO depends on the substrate [175] and on the rotational orientation [174, 184]. Adsorbing the molecule to a second surface (the tip) may influence splitting and energy properties of the LUMO likewise. In a recent study the LUMO shift in distance-dependent spectroscopy of C_{60} on Cu(1 1 1) was led back to increasing hybridization between tip and molecule [42]. We thus tend to ascribe the observed LUMO shift to increasing hybridization as well. However, the interpretation of dI/dV data as a measure of the local density of states may only be valid in tunneling regime [42, 185]. Here, features in dI/dV spectra can readily be attributed to the signatures of molecular orbitals. At smaller tip-sample separation dI/dV data may be discussed in terms of transmission channels [42].[3]

Figure 7.5 shows background subtracted IET spectra recorded atop the same molecule [Fig. 7.3(a)]. The feedback loop was disabled at the same setpoint conductances as shown above [Fig. 7.3(b)]. The subtracted background was estimated from low-pass filtering of the original data [see Appendix E.3]. In-between spectrum acquisition topographic images and current-distance curves were recorded, which ensured stable conditions. In tunneling regime (black lines) peaks were found at low voltages. At energies covered by the LUMO (shaded area below the curves) vibrational features were present with asymmetric features or dip-like line shapes, as expected [see Sec. 6.2]. Features outside the LUMO spectral range (H_g(1)–(4) modes at 33 mV, 52 mV, 87 mV, and 96 mV) retained their peak-like

[3] Despite these concerns we refer to the spectral feature as to the LUMO signature in all conductance regimes.

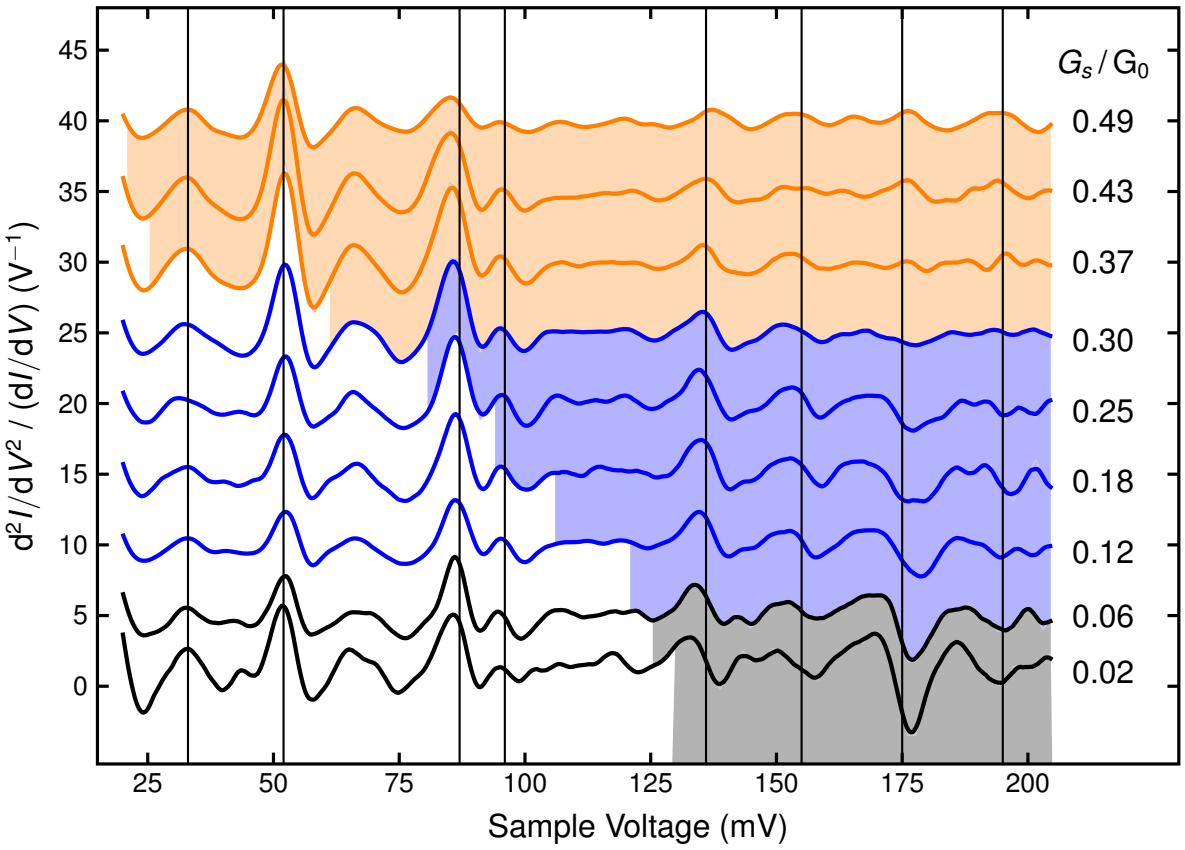

Figure 7.5 Background subtracted $d^2I/dV^2/(dI/dV)$ spectra (solid lines) acquired with the feedback loop disabled at the conductances G_s indicated in Fig. 7.3(b). The respective conductance is labeled to the right of each curve. Acquisition parameters and shaded areas are the same as in Fig. 7.4(a). Vertical lines indicate energies of all H_g modes. Spectra were offset for clarity.

appearance for any tip-sample distance. The feature ascribed to the $H_g(5)$ mode (136 mV) gradually converted from an asymmetric line shape in tunneling regime towards a peak in contact regime. Signatures attributed to the $H_g(6)$–(8) modes (155 mV, 175 mV, and 195 mV) underwent a conversion from dips to peaks upon approaching the tip. In contrast to the $H_g(1)$–(5) modes intensities of these features changed drastically. When entering contact range ($G_s = 0.3\,G_0$) features vanished completely. The features re-emerged as peaks when G_s was further increased. For $H_g(7)$,(8) modes dip-like line shapes were retained at all setpoint conductances in the tunneling and intermediate regime. At 155 mV ($H_g(6)$) a conversion *via* asymmetric line shapes is visible. The spectra acquired at negative voltage showed solely dips in contact as well as in tunneling regime, thus were essentially the

same [see Appendix E.4].

In contact regime line widths average at FWHM = 6.7 meV, which is slightly larger than 5.9 meV in tunneling regime. Tunneling line widths are well explained by thermal and modulation broadening. However, line widths in contact regime require explanation by additional mechanisms. The most important broadening mechanism is the vibration decay *via* electron-hole pair generation [24]. In contact regime vibrations may decay through additional electronic states at the tip. Thus, considerable life-time decrease can be expected, which causes increased line width broadening.

The H_g vibrational features[4] were found at the same energies for all examined IET spectra. In previous IET experiments vibrational energies shifted at varying electrode distance [41, 179, 186–188]. Such shifts have been reported for small molecules like CO and H_2 between metal electrodes [41, 179] as well as for more complex molecules [186–188]. The effect was ascribed to the perturbation of the electronic and structural properties of the junction [38, 41, 187]. Vibrational shifts due to the electric field in the junction are expected to be small for C_{60} molecules. The sample bias voltage causes an electric field between tip and sample. This can be important, considering CO vibrational energies vary on the order of 10 meV at the presence of external charges [189] or dipole moments [190]. However, the C_{60} cage modes are expected to change by less than 1 meV for electric fields up to 0.5 V/Å [191] (here $\approx$ 0.3 V/Å). Shifts due to changing intra-molecular forces at decreasing tip-sample distance may be small as well. Previously, transverse modes shifted in analogy to the pitch of a guitar string, when it is tuned [177, 179, 187]. In a string the frequency is determined by its length and the tension. The C_{60} cage is typically much stiffer than the leads, as revealed by DFT calculations [29]. Any deformation of the junction at contact [see Fig. 7.3] can thus be ascribed to the deformation of the Pb surfaces and the electrode-C_{60} bonds. Therefore, C-C bond lengths in the C_{60} cage can be assumed to stay rather constant. The tension may be compared to a pressure put on the C_{60} cage. IR measurements of bulk C_{60} under external pressure revealed only small changes (< 0.1 meV/kbar) of vibrational energies [192]. Consequently, only small variations of

[4] The changing line shape of the signatures for H_g(6)–(8) modes impedes sufficiently accurate determination of the vibrational energy at positive voltages. However, no shifts are found in negative voltage range.

vibrational energies at tip approach are expected, which is in accordance with the experimental results.

For high setpoint conductances the findings seem in contradiction with the results obtained in tunneling regime. As the LUMO shifts towards zero at increasing G_s low-energy IET features ($H_g(1)$–(4)) are expected to convert from peaks into dips [see Secs. 6.2, 6.3, 7.1]. However, for these modes peaks are observed at all tip-sample distances. The removal of the connection between vibrational line shapes and the electronic structure is remarkable. Despite considerable concerns about the interpretation of $\mathrm{d}I/\mathrm{d}V$ data in contact regime [see above], we expect additional mechanisms to exceed the influence of the electronic structure. This expectation is supported by the evolution of vibrational features at 155–195 meV, which undergo a dip-to-peak conversion between tunneling and contact regime. At a certain tip-sample distance the features vanish completely. These characteristics may result from changing IETS propensities, varying transmission probabilities, and vanishing elastic processes.

To explain line shapes in all conductance regimes we consider the relative position of the molecule with respect to the electrodes. Vibrational line shapes have been predicted to depend on the symmetry of the junction [43, 44, 181]. In the theory applied above asymmetric and dip-like features were explained by contributions from an additional elastic channel [23]. The channel was assigned to the emission and re-absorption of vibrational quanta. Such processes have been predicted to vanish for a molecule centered between the electrodes [43]. In this case purely peaks are expected in IET spectra at positive voltages. We approach these symmetry considerations by switching vibration-mediated elastic processes on and off, depending on the molecule position. In the (modified) expression for the vibration-related differential conductance correction [compare with Eq.(6.1)] elastic contributions [Appendix E.5] are weighed with an additional parameter η. The corresponding expression for the normalized differential conductance at positive voltages reads

$$\frac{\mathrm{d}I}{\mathrm{d}V} = 1+u\,\frac{\left[(\hbar\omega-E_\mathrm{M})^2+\left(\frac{\Gamma_\mathrm{M}}{2}\right)^2-2\eta\left(\frac{\Gamma_\mathrm{M}}{2}\right)^2\right]\Theta(eV-\hbar\omega)-\eta(\hbar\omega-E_\mathrm{M})\frac{\Gamma_\mathrm{M}}{\pi}\ln\left|\frac{eV-\hbar\omega}{\Delta}\right|}{\left[E_\mathrm{M}^2+\left(\frac{\Gamma_\mathrm{M}}{2}\right)^2\right]\left[(\hbar\omega-E_\mathrm{M})^2+\left(\frac{\Gamma_\mathrm{M}}{2}\right)^2\right]}. \quad (7.1)$$

η may be interpreted as a measure for the probability of elastic reflections. Some electrons entering the tunneling barrier are reflected due to interaction with a molecular vibration. These reflections result from the statistics of the many-electron system [43]. The probability of the reflections depends on the location of the molecule, since electronic states exponentially decay into the vacuum [43]. Further, the reflection matrix elements for tip and sample states may cancel out in case the molecule is centered between the leads [43]. For $\eta = 1$ the molecule is adsorbed to one lead only, and the expression is equal to Eq. (6.1). A symmetric junction with the molecule coupled equally to both electrodes is reflected by $\eta = 0$. Here, solely inelastic currents contribute to the vibrational feature, yielding a step increase. By varying η between these values we turn elastic contributions from two-step processes on and off.

Figure 7.6 shows simulated $\mathrm{d}^2I/\mathrm{d}V^2$ curves for varying η. Results from Eq. (7.1) for each considered vibrational mode were added. The outcome was numerically differentiated and broadened by convolution with appropriate functions for thermal and instrumental broadening [51, 52]. For simplicity the LUMO parameters of the molecule were kept constant at $E_\mathrm{M} = 180\,\mathrm{meV}$ and $\Gamma_\mathrm{M} = 100\,\mathrm{meV}$. The results show remarkable similarities with the experimental data shown in Fig. 7.5(e). In a symmetric junction ($\eta = 0$) peaks are obtained for all vibrational energies. An asymmetric junction ($\eta = 1$) yields dips and asymmetric line shapes for $\mathrm{H_g}(5)$–(8) modes. Notably, these features exhibit minimal intensities for $\eta = 0.5$. Further, vibrational features for $\mathrm{H_g}(1)$–(4) modes are essentially independent from the assumed molecule position. Consequently, the molecule location inside the junction may be considered an important factor in the evolution of vibrational line shapes and feature intensities.

A variety of modern theoretical works relate the vibrational line shape to the electron transmission probability through the junction [44, 193, 194]. For example, IET spectra at CO molecules on Cu(1 1 1) [195] were shown to exhibit peaks at positive voltages, which was attributed to low electron transmission. In contrast, high transmission probability through $\mathrm{H_2}$ molecules between Pt electrodes [177, 179] leads to vibrational dips.[5]

[5] In the low-transmission regime the transition of an electron to the other electrode is a rare event. At high transmission electron distributions in the leads may be disturbed, which leads to increased backscattering

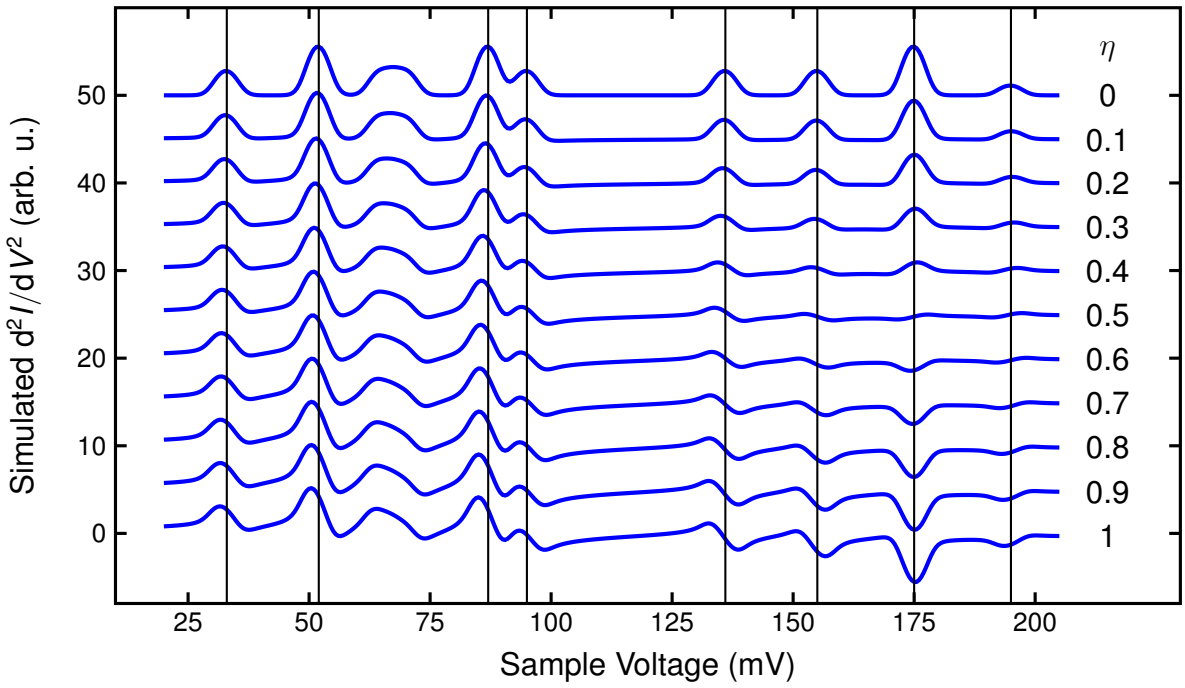

Figure 7.6 Simulated d^2I/dV^2 spectra (blue curves) from numerically differentiated and broadened Eq. (7.1) for varying molecule position parameter η (labeled to the right of each curve). $H_g(1)$–(8) modes (vertical lines) and $T_{1u}(1)$,(2) have been considered with energies at 33, 52, 65, 70, 87, 95, 136, 155, 175, 195 meV and intensities similar to experimental values. $E_M = 180$ meV and $\Gamma_M = 100$ meV, intensities and vibrational energies were kept constant for all curves. Broadening for $T = 6$ K and $V_{mod} = 4.24$ mV were assumed.

The peak-like appearance of all C_{60} vibrational modes in contact regime [Fig. 7.5] may be interpreted as a consequence from low electron transmission probability, as suggested previously for off-resonant IET spectra [26]. However, the coincidently measured energy-dependent electronic structure may obscure interpretations on the basis of transmission probability. Corresponding theories are based on the assumption of constant local density of states [193, 194]. In addition, related works show similar line shapes for all vibrational features [44], in contrast to our findings.

Finally, we comment on propensity rules of vibrational modes, which determine the appearance of vibrational features in IETS. Propensities of vibrational modes were linked to symmetry properties of the involved electronic wave functions [154, 195]. A recent study

at the onset of inelastic scattering [181].

addresses IETS of a CO-functionalized STM tip atop a CO molecule on Cu(1 1 1) [195]. The signature of the ν_β mode[6] was reported to vanish at a specific tip-sample distance. DFT calculations revealed, the molecules were aligned, such that one lobe of the CO state at the surface was aligned with a nodal plane of the molecule at the tip. In this configuration minimum inelastic signal is expected [154, 195]. For C_{60} on Pb(1 1 1) the rotational orientation of the molecule is likely to stay constant upon tip approach, since the conductance-distance curve [Fig. 7.3(b)] has a smooth shape. Sudden variations of the junction geometry were previously connected to changes in the number of conductance channels, which resulted in characteristic discontinuities [110]. However, the adsorption of C_{60} molecules onto a Au surface has been shown to lower the C_{60} icosahedral symmetry. This caused splits and shifts of vibrational modes as well as the relaxation of selection rules in surface-enhanced Raman spectroscopy [74]. Similar change of symmetry may be induced by approaching the tip towards the molecule in the present case, as bonding to a second lead is formed. These symmetry changes may be reflected in emerging or disappearing vibrational features at different tip-sample distances. Additional vibrational signatures in $\mathrm{d}^2I/\mathrm{d}V^2$ [Fig. 7.5] are found at 107 mV (T_{3g}(3)[80, 191] or G_u(3)[79]), 120 mV (G_u(4) [80, 191]), 125 mV (A_u [191]), and 165 mV (G_u(5) [79, 80, 191]). Features at 42 meV (T_{3u}(1) [92]) and 146 meV (T_{1u}(3) [92]) vanish. Further, a feature evolves at 180 meV (A_g(2) [80]) in the intermediate regime. The lower intensities of H_g vibrational features measured in contact regime [Fig. 7.5, $G_s \geq 0.43\,G_0$] may also be a consequence from the symmetry change, together with additional broadening [see above].

[6] ν_β describes the out-of-phase mode combining the hindered translations of two CO molecules in the surface-normal plane.

7.3 Conclusions

The site-dependent variation of $\mathrm{d}I/\mathrm{d}V$ and $\mathrm{d}^2I/\mathrm{d}V^2$ spectral features was examined for C_{60} molecules adsorbed to the Pb(1 1 1) surface. C_{60} molecules adsorbed to a step edge yielded higher LUMO energies than molecules well separated from steps. Vibrational features in IETS depended on the LUMO properties of the molecule, which supports the findings in Secs. 6.2,6.3. The observation of peaks at high vibrational energies supports previous reports about off-resonant spectra of C_{60} on Pb(1 1 1) [26].

In a second step tip-sample distance-dependent $\mathrm{d}I/\mathrm{d}V$ and $\mathrm{d}^2I/\mathrm{d}V^2$ spectra were acquired for a **5**-C_{60}. At increasing setpoint conductance the low-energy LUMO component broadened and shifted towards lower energies. Vibrational features in IET spectra varied with the tip-sample distance. In tunneling conditions vibrational dips were found in energetic proximity to the LUMO. In contact regime, all H_g vibrations were present as peaks, despite considerable variations of the $\mathrm{d}I/\mathrm{d}V$ spectrum in the energy range of molecular vibrations. Moreover, intensities of high-energy vibrational features (155–195 meV) vanished during the formation of mechanical tip-molecule contact. Vibrational feature variations were attributed to the changing junction geometry. In a qualitative model elastic contributions to the vibrational signatures were weighed by a parameter η, which accounted for the molecule position inside the junction. Corresponding simulated spectra exhibited remarkable similarities with the experimental data. The presented results stress the importance of molecule-tip interactions and molecule position in IETS. Moreover, the disappearance of vibrational modes is linked to geometric parameters of the junction. In future applications the molecule position may be used to deliberately remove vibrational features in current-voltage curves of single molecules.

8 Conclusions and Prospects

A scanning tunneling microscope was optimized to work at very low temperatures, and with high spectroscopic resolution. The state-of-the-art instrument was successfully deployed in scanning tunneling experiments. The experimental part of this work examines a selection of physical effects, that give rise to Fano-like line shapes in scanning tunneling experiments. The initially posed questions about aspects of the Kondo effect and inelastic electron tunneling spectroscopy are addressed in four chapters.

(I) Kondo effect of single Co atoms on Au(110)

The described experiment is the first published examination of the single-Co Kondo effect on Au(1 1 0). Two distinct adsorption sites were examined, for which an adsorption model was proposed. Spectra of the differential conductance revealed a peak close to zero voltage, which was attributed to the Kondo resonance. Peak-like line shapes were ascribed to strong tip-Co coupling. The Kondo amplitude is anisotropically distributed across an obliquely adsorbed Co adatom. This observation was ascribed to varying tip-substrate distance. The discovered topographic effect may be relevant to other systems where the tip-substrate distance varies across Kondo impurities. Such systems may include magnetic molecules on noble metals.

(II) Asymmetry parameter of peaked Fano line shapes

For peaked Fano line shapes the fit of the conventional Fano function to experimental data lead to difficulties in unambiguously extracting the asymmetry parameter, which may vary over orders of magnitude without degrading the quality of the fit. Using the newly discovered peak in $\mathrm{d}I/\mathrm{d}V$ Co on Au(1 1 0), the ambiguity of the extracted asymmetry parameter

was traced to the highly symmetric resonance profile combined with the inevitable scattering of experimental data. Moreover, the extracted asymmetry parameter depended on initially guessed values. An improved parameterization of the conventional Fano function was suggested that enabled the nonlinear optimization in a reduced parameter space. In addition, the presence of a global minimum in the sum of squared residuals, and thus the independence of start parameters, may conveniently be identified in a two-dimensional plot. An angular representation of the asymmetry parameter was suggested in order to reliably determine uncertainty margins via linear error propagation.

(III) Spectroscopic Line Shapes of Vibrational Quanta in the Presence of Molecular Resonances

Bare as well as C_{60}-terminated Pb tips of a scanning tunneling microscope and clean as well as C_{60}-covered Pb(111) surfaces were used in low-temperature experiments. Depending on the overlap of orbital and vibrational spectral ranges different spectroscopic line shapes of molecular vibrational quanta were observed. The energy range covered by the molecular resonance was altered by modifying the adsorption configuration of the molecule terminating the tip apex. Concomitantly, the line shapes of different vibrational modes were affected. The reported observations represent an experimental proof to theoretical predictions on the contribution from resonant processes to inelastic electron tunneling.

(IV) Impact of the Molecule Position on Vibrational Line Shapes

The lowest unoccupied molecular orbital of C_{60} on Pb(1 1 1) was examined at different adsorption sites. Collaterally, IET spectra were acquired atop the same molecules. The proposed connection between C_{60} vibrational features and the molecular electronic structure was substantiated. Further, $\mathrm{d}I/\mathrm{d}V$ and IET spectra were recorded as a function of the tip-molecule distance. At decreasing tip-sample distance the LUMO signature shifted towards the Fermi energy. In contact range IETS vibrational features were found independent from features in $\mathrm{d}I/\mathrm{d}V$Here, all H_g modes were present as peaks. This observation

was ascribed to a symmetric molecule position inside the junction. Our findings stress the importance of the junction symmetry in IETS. Future experiments may target IETS of molecule-substrate systems with electronic resonances close to the Fermi energy. Such systems could be used to control vibrational features. By changing the tip-sample distance vibrational signatures may be deliberately removed.

The optimized instrument will be deployed in future endeavors of the experimental group. High resolution and low temperatures enable experiments in a vast field of physics, including the Kondo effect, IETS, and superconductivity.

APPENDIX

A Optimization of a STM

A.1 Fitting the Superconducting Gap

The quasi-particle tunneling current may be described by [196]

$$I = \frac{4\pi M}{\hbar} \int_{-\infty}^{\infty} \rho_t(E - eV, T_t)\rho_s(E, T_s)[f(E - eV, T_t) - f(E, T_s)]\,dE. \tag{A.1}$$

T_s and T_t are the temperatures of the sample and the tip, respectively. The densities of states of the tip ρ_t or the sample ρ_s can be expressed as [6]

$$\rho_{t,s} = \mathrm{Re}\left(\frac{|E|}{\sqrt{E^2 - \Delta_{BCS}^2}}\right). \tag{A.2}$$

Δ_{BCS} describes the temperature-dependent Bardeen-Cooper-Schrieffer superconducting gap which may be approximated by [6]

$$\Delta_{BCS} \approx 3.07 k_B T_c \sqrt{1 - \frac{T}{T_c}} \tag{A.3}$$

for T just below the critical temperature of Pb $T_c = 7.2$K. The final differential conductance is extracted from Eq. (A.1) by numerical differentiation and subsequent convolution with the lock-in broadening function [Eq. (2.9)] and a normalized Gaussian, accounting for random fluctuations of the bias voltage [53]. In the least-squares fit to the experimental data sample and tip temperatures, gaussian width, a prefactor and an offset are free parameters.

A.2 Liquid Helium Consumption

For measuring the liquid helium level L, a probe (Cryogenics probe type 105) containing a superconducting element is inserted into the helium bath. Using a helium level gauge (Cryogenics HLG200) the liquid helium level is extracted. In order to estimate the remaining standing time, the level decrease per hour $D \approx -\mathrm{d}L/\mathrm{d}t$ was measured between two points in time t_1 and t_2

$$D = \frac{L(t_1) - L(t_2)}{t_2 - t_1}. \tag{A.4}$$

Figure A.1(a) shows, D is dependent on the filling level of the helium vessel. Assuming a linear increase of helium consumption with L (fit in Fig. A.1(a)), the level change with time may be estimated by the following differential equation

$$-\frac{\mathrm{d}L}{\mathrm{d}t} = \tilde{a}L + \tilde{b}. \tag{A.5}$$

Estimates for the parameters $\tilde{a} = 0.0122\,\mathrm{h}^{-1}$ and $\tilde{b} = 10.4\,\mathrm{mm/h}$ are extracted from the linear fit of the data shown in Fig.A.1(a). The solution of Eq. (A.5) results in the remaining standing time

$$t_{\mathrm{rs}} = \frac{1}{\tilde{a}} \ln\left(\frac{\tilde{a}L}{\tilde{b}} + 1\right). \tag{A.6}$$

$t_{\mathrm{rs}}(L)$ is depicted in Fig. A.1(b), showing significant deviation from a linear model obtained from the mean level decrease $\overline{D} = 13.6\,\mathrm{mm/h}$. Deviations may be as high as 2.6 h.
The modeled $t_{\mathrm{rs}}(L)$ accurately describes temporal level changes, assuming closed, well separated shields, turned off temperature diode and no sample transfer or material deposition during the respective time interval. The level gauge should be turned off between measurements.

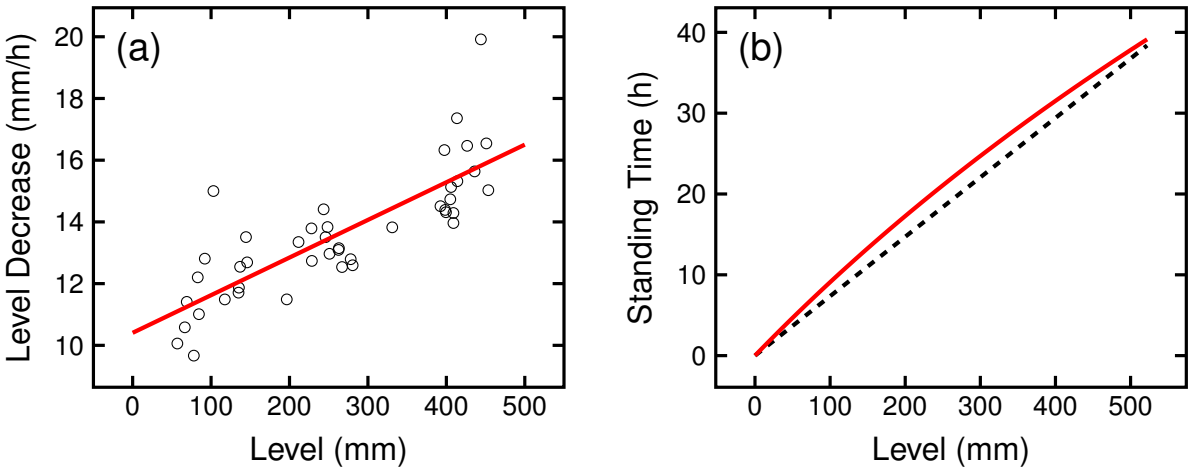

Figure A.1 (a) Hourly decrease of the liquid helium level D as a function of the filling level L between two measurements (black circles). The solid line represents the best linear fit to the data. **(b)** Remaining standing time t_{rs} as a function of the liquid helium level (red line) estimated from the fit in (a) compared with the estimate from a linear model (black dashed line) from the average level decrease in (a).

B Single-Co Kondo Effect

B.1 Adsorption of Single Co Adatoms

Determining the adsorption position of single Co atoms on Au(1 1 0) is challenging, since the exact Au atom positions are unknown. The reconstruction rows may help to determine the position of the topographic maximum in [0 0 1] direction. However, positions of the topographic maximum and the Co core are likely to differ, since the STM is sensitive to the electronic density of states. A convincing estimation of adsorption geometries can be obtained from manipulation experiments. Here, we shift Co atoms from f into mr sites, by applying a voltage pulse atop the atom. Occasionally, a shift occurs during the scan across an atom, as shown in Fig. B.2(a). A lateral offset δ between the topographic maxima in $[1\,\bar{1}\,0]$ direction is visible. The δ obtained in various manipulation experiments is scattered around 0.144 pm, which is half the distance between Au nearest neighbors [Fig. B.2(b)]. Some of the possible manipulation paths A–D are shown in Fig. B.2(c). Path A shows the most probable scenario. The distance between adsorption sites along $[1\,\bar{1}\,0]$ matches the observed adsorption shift. The other path B with equal displacement in $[1\,\bar{1}\,0]$

direction ends in a bridge site. This adsorption position has been predicted to exhibit a significant higher adsorption energy ($\approx 0.6\,\mathrm{eV}$) than the final site of path A [102]. For this reason, we exclude paths B and C. In some manipulation events [4 and 5 in Fig. B.2(b)] the uncertainty embraces zero displacement in $[1\,\bar{1}\,0]$ direction. For these events path D is a possible scenario. However, for all manipulated f-Co atoms apparent heights were essentially the same. The initial adsorption geometry of path D has further been predicted to exhibit higher adsorption energy and less diffusion stability than the initial position in A [102]. Thus, we tend to assign path A to all manipulation events.

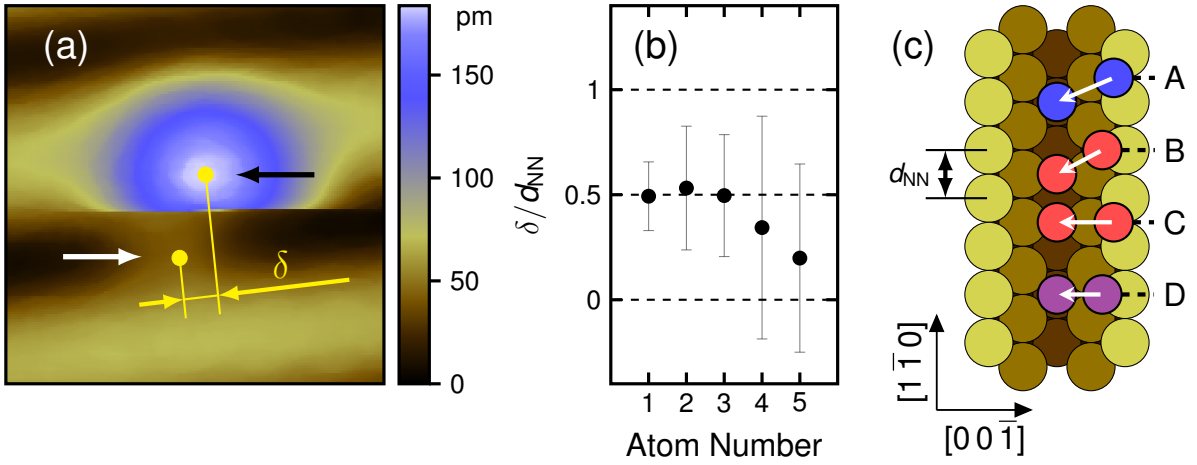

Figure B.2 (a) Topographic image ($1.7 \times 1.7\,\mathrm{nm}^2$, 1 nA, 50 mV) of a f-Co atom (black arrow), which moved to a mr position (white arrow) during the scan. Yellow arrows measure the distance δ along $[1\,\bar{1}\,0]$ between the topographic maxima (yellow dots) of the atom in f and in mr position. **(b)** Measured δ in distances of Au nearest neighbors ($d_{\mathrm{NN}} = 288\,\mathrm{pm}$) for various manipulation events. Horizontal dashed lines indicate distances between highly symmetric adsorption geometries along $[1\,\bar{1}\,0]$. **(c)** Sketch of the Au(1 1 0)-(1 × 2) surface Au atoms (yellow full circles) and adsorbed Co atoms (blue, red, violet full circles). The adsorption shift due to manipulation is indicated by white arrows. Each possible manipulation path is labeled (A–D). Crystallographic directions are indicated.

B.2 mr-Co Kondo Amplitude Distribution

Fig. B.3(a) shows the topographic map of a single mr-Co atom adsorbed inside a missing row of the reconstructed Au(1 1 0)–(1 × 2) surface. Along the [0 0 1] direction dI/dV spectra were acquired [Fig. B.3(b)]. The same procedure was carried out on another mr-Co

atom [Fig. B.3(c)], with spectra taken along $[1\,\bar{1}\,0]$ [Fig. B.3(d)]. Fits to the spectroscopic data [Fig. B.3(c),(d)] yielded amplitudes with similar spatial variation in both crystallographic directions [Fig. B.3(e)]. Since normalization with the tip-substrate coupling parameter is relevant for amplitude distributions of f-Co atoms, normalized amplitudes are shown [Fig. B.3(f)]. The tip–substrate distance variation was calculated from the difference of apparent heights at the spectrum position and at an equivalent position on the clean substrate. A gaussian fit to the data yields full width at half maximum of 0.43 ± 0.05 nm, similar to the normalized data shown for f-Co atoms (0.47 nm, see Fig. 4.6).

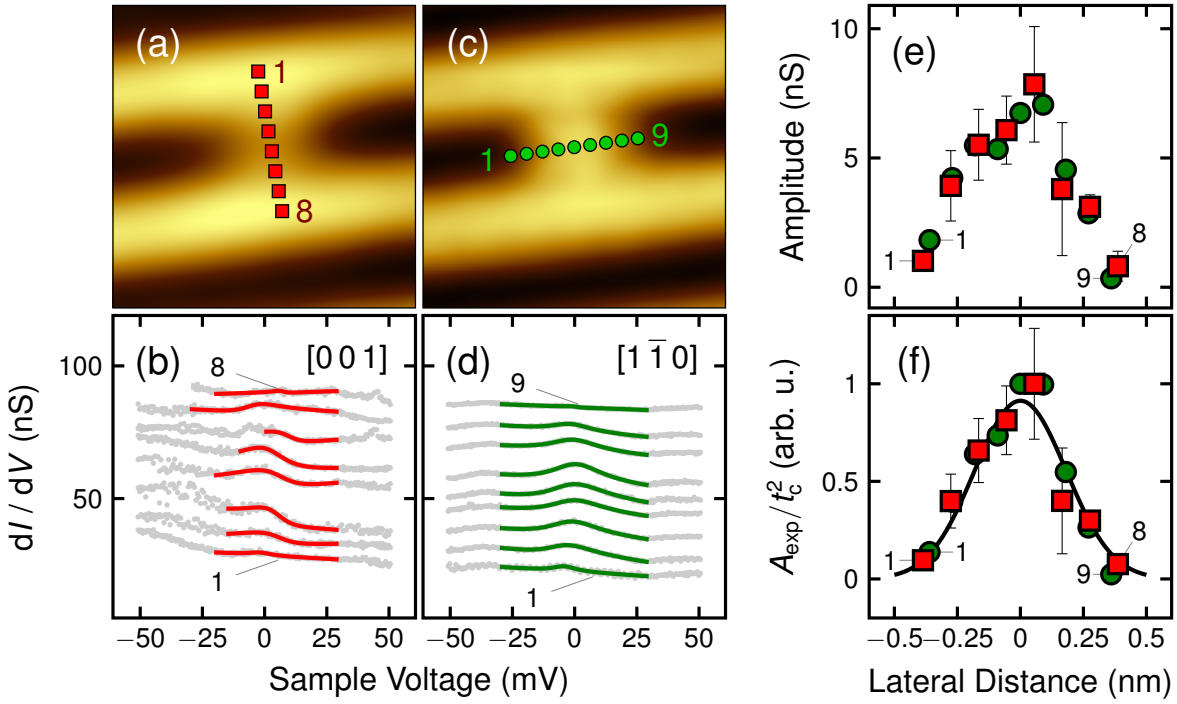

Figure B.3 (a) Topographic map of a single *mr*-Co atom (1 nA, 50 mV, $1.7 \times 1.7\,\mathrm{nm}^2$). Squares (a) indicate positions labeled 1–8 along [0 0 1] of acquired $\mathrm{d}I/\mathrm{d}V$ spectra shown in (b). **(b)** Set of $\mathrm{d}I/\mathrm{d}V$ spectra acquired (grey dots) at positions indicated in (a). Prior to spectroscopy the feedback loop had been disabled at 1 nA, 50 mV for each spectrum. Full lines represent Fano fits to the experimental data. **(c)** like (a) with spectra positions (dots) labeled 1–9 along $[1\,\bar{1}\,0]$. **(d)** like (b) at positions indicated in (c). **(e)** Amplitude values extracted from fits shown in (b) (squares) and (d) (dots). Labels correspond to the spectrum positions in (a), (c). **(f)** $A_{\mathrm{exp}}/t_{\mathrm{c}}^2$ for both data sets (b), (c) calculated from amplitude values in (e) and topography in (a), (c). The values were normalized to the maximum of the respective data set. The solid line indicates a gaussian fit to the data with full width at half maximum 0.43 nm.

B.3 Asymmetry parameter from Fits with Improved Parameterization

Fits of $\mathrm{d}I/\mathrm{d}V$ data across a f-Co adatom were carried out according to the improved parameterization described in Sec. 5.3. Figure B.4(a) shows the variation of $\alpha = 2\tan^{-1}(q)$ as a function of the lateral distance, r, to the Co atom at $r = 0\,\mathrm{nm}$.[1] At $r = 0$ the asymmetry parameter exhibits $\alpha \approx -\pi$ ($q \approx -\infty$), which is equivalent to a Lorentzian line shape. With increasing radial distance α increases and the line shape gradually becomes asymmetric. Towards the adjacent missing row (green dots, Fig. 4.5(a),(b)) determination of the angular line shape parameter is subject to higher uncertainty due to the faster decreasing amplitude. In this direction significant scattering of the data is observed at $r > 0.2\,\mathrm{nm}$ and large uncertainty margins are extracted. In the opposite direction (and along $[1\,\bar{1}\,0]$) uncertainties become large at $r > 0.5\,\mathrm{nm}$.

In most directions $q(r)$ approximately follows a gaussian distribution [black line, Fig. 4.5(a)]. Towards the missing row scattering of the data impedes unambiguous determination of the spatial evolution. Very close to the adatom ($r < 0.2\,\mathrm{nm}$) we expect $a_0(r)$ to deviate from a gaussian profile, since $q \to -\infty$ and t_c^2 as well as A_{exp} are finite. Such behavior may arise from varying hybridization across the adatom [96].

We have indicated the parameter estimates as extracted using the conventional Fano function (black crosses, Figs. B.4(a), (b)). These data coincide with the results from fitting with the improved parameterization. Only at $r = 0$ data deviates slightly, since the central point in Fig. 4.5 was estimated from the averaging of many spectra atop Co adatoms.

[1] We decided to use the angular representation of the line shape parameter, because it is advantageous for the discussion of peak-like line shapes [see Sec. 5.3].

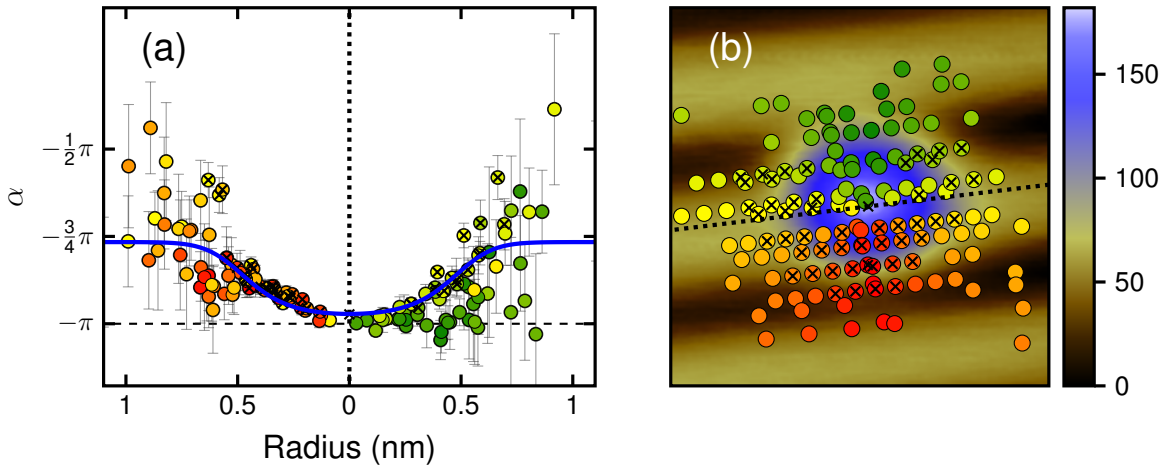

Figure B.4 (a) Asymmetry parameter $\alpha = 2\tan^{-1}(q)$ extracted from fits of $\mathrm{d}I/\mathrm{d}V$-spectra in the vicinity of a f-Co adatom at positions indicated in (b). Radial coordinates were split according to the lateral displacement in [0 0 1]-direction relative to the adatom at $r = 0$ (vertical dotted line). Uncertainty margins are given for a confidence level of 95%. The transformed gaussian distribution of q (blue solid line) as well as fit parameters extracted with the conventional parameterization (black crosses) are indicated indicated [see Fig. 4.5]. **(b)** Topographic map of a f-Co adatom (1 nA, 50 mV, $2 \times 2\,\mathrm{nm}^2$). Dots indicate the positions, where $\mathrm{d}I/\mathrm{d}V$ spectra were acquired from which asymmetry parameters in (a) were extracted. The dotted line divides the data shown in (a) according to their lateral [0 0 1]-coordinate with respect to the adatom. The color of each data point is the same in (a) and (b). Black crosses indicate the spectra positions from which asymmetry parameters were extracted using the conventional parameterization of the Fano function [see Fig. 4.5]

C Asymmetry Parameter of Peaked Fano Line Shapes

C.1 Optimization

The inner level of the two-level optimization consists of solving a linear least-squares problem. Each data point of an experimental spectrum is characterized by $E_i = eV_i$ and $y_i = \mathrm{d}I/\mathrm{d}V|_{V_i}$ with $1 \leq i \leq M$. With $\mathbf{y}^{\mathrm{T}} = (y_1, \ldots, y_M)$, $\boldsymbol{\beta}^{\mathrm{T}} = (k, l, m, n)$ one may write $\mathbf{y} = \mathbf{X}\boldsymbol{\beta} + \boldsymbol{\eta}$ with

$$\mathbf{X} = \begin{pmatrix} \frac{1}{1+\varepsilon_1^2} & \frac{\varepsilon_1}{1+\varepsilon_1^2} & \varepsilon_1 & 1 \\ \frac{1}{1+\varepsilon_2^2} & \frac{\varepsilon_2}{1+\varepsilon_2^2} & \varepsilon_2 & 1 \\ \vdots & \vdots & \vdots & \vdots \\ \frac{1}{1+\varepsilon_M^2} & \frac{\varepsilon_M}{1+\varepsilon_M^2} & \varepsilon_M & 1 \end{pmatrix}, \tag{C.7}$$

$\boldsymbol{\eta}^{\mathrm{T}} = (\eta_1, \ldots, \eta_M)$ the residuals and $\varepsilon_i = (E_i - E_0)/\Gamma$. The optimal parameter set for the inner optimization level, $\hat{\boldsymbol{\beta}} = (\mathbf{X}^{\mathrm{T}}\mathbf{X})^{-1}\mathbf{X}^{\mathrm{T}}\mathbf{y}$, reflects minimal $\chi^2 = \sum_i \eta_i^2$. The outer level yields Γ_{f}, $E_{0\mathrm{f}}$ for $\hat{\boldsymbol{\beta}}^{\mathrm{T}} = (k_{\mathrm{f}}, l_{\mathrm{f}}, m_{\mathrm{f}}, n_{\mathrm{f}})$, which optimizes the inner level. This two-dimensional nonlinear optimization problem may be solved using standard minimization algorithm, *e. g.*, *fminunc* in GNU Octave [197].

C.2 Optimality of the Angular Representation

For a monotonically increasing and twice differentiable parameterization $\Psi = \Psi(\alpha)$ the second-order term in the Taylor expansion reads

$$\mathbf{H}_\Psi = \nabla(\nabla\Psi)^{\mathrm{T}} = \Psi''\mathbf{G}_\alpha + \Psi'\mathbf{H}_\alpha \tag{C.8}$$

with $\Psi' = \mathrm{d}\Psi/\mathrm{d}\alpha$ and $\Psi'' = \mathrm{d}^2\Psi/\mathrm{d}\alpha^2$. The specific choice of $\alpha = 2\tan^{-1}(q)$ with q given by Eq. (5.6) yields

$$\mathbf{G}_\alpha = (\nabla\alpha)(\nabla\alpha)^{\mathrm{T}} = \frac{1}{(k^2+l^2)^2}\begin{pmatrix} l^2 & -kl \\ -kl & k^2 \end{pmatrix}, \tag{C.9}$$

$$\mathbf{H}_\alpha = \nabla(\nabla\alpha)^{\mathrm{T}} = \frac{1}{(k^2+l^2)^2}\begin{pmatrix} -2kl & k^2-l^2 \\ k^2-l^2 & 2kl \end{pmatrix} \tag{C.10}$$

with $\nabla\alpha = (\partial\alpha/\partial k, \partial\alpha/\partial l)$. The squared Frobenius norm of $(k^2+l^2)^2\mathbf{H}_\Psi$ then reads

$$A^4\sum_{i,j}(\mathbf{H}_\Psi)_{i,j}^2 = \Psi''^2 + 2\Psi'^2. \tag{C.11}$$

Equation (C.11) shows that the Frobenius norm is mimimized for $\Psi = \text{const}$, which shall be excluded as a trivial case. If Ψ were nonlinear then Ψ' would be nonzero almost everywhere. Moreover, at any α with $\Psi'' \neq 0$ a linear transformation with slope Ψ' would result in a smaller Frobenius norm. Since linear error propagation works equally well for all linear transformations we conclude that $\Psi(\alpha) = \alpha$ gives — for almost every α — an optimal parameterization of the asymmetry parameter.

C.3 Transformed Probability Density

According to Fig. 5.4(b) the probability density for α is approximately given by a (wrapped) normal distribution

$$\varrho_\alpha(\alpha) = \frac{1}{\sigma_\alpha\sqrt{2\pi}} \sum_{j=-\infty}^{\infty} \exp\left[-\frac{(\alpha-\alpha_g-2\pi j)^2}{2\sigma_\alpha^2}\right] \qquad \alpha \in [-\pi,\pi] \tag{C.12}$$

with the true value α_g and the standard deviation σ_α. The probability density for q reads [198]

$$\varrho_q(q) = \sum_{\alpha,q(\alpha)=q} \frac{\varrho_\alpha(\alpha)}{|q'(\alpha)|} \tag{C.13}$$

where $q' = \mathrm{d}q/\mathrm{d}\alpha$. The probability density is then expressed by

$$\varrho_q(q) = \frac{2}{\sigma_\alpha\sqrt{2\pi}(1+q^2)} \sum_{j=-\infty}^{\infty} \exp\left\{-\frac{2}{\sigma_\alpha^2}\left[\tan^{-1}(q)-\tan^{-1}(q_g)-\pi j\right]^2\right\}. \tag{C.14}$$

For practical purposes, the sum may be limited to $j = -1, 0, 1$, as the summands decrease very fast with j. Figure 5.2(b) shows the graph of $\varrho_q(q)$ as a full line. To this end a prefactor was used that was determined by the product of bin size and total number of values.

C.4 Error Propagation

The standard error of α,

$$s_\alpha = \sqrt{(\nabla\alpha)^{\mathrm{T}}\sigma^2\mathbf{C}\nabla\alpha}, \tag{C.15}$$

may be approximated *via* linear error propagation. To this end, $F(k,l,m,n,\Gamma,E_0)$ [Eq. (5.4)], is linearized at $(k_\mathrm{f}, l_\mathrm{f}, m_\mathrm{f}, n_\mathrm{f}, \Gamma_\mathrm{f}, E_{0\mathrm{f}})$ [199]. The variance-covariance matrix of the parameter

estimators $\sigma^2\mathbf{C} = \sigma^2(\tilde{\mathbf{X}}^{\mathrm{T}}\tilde{\mathbf{X}})^{-1}$ is determined with

$$\tilde{\mathbf{X}} = \begin{pmatrix} \frac{1}{1+\tilde{\varepsilon}_1^2} & \frac{\tilde{\varepsilon}_1}{1+\tilde{\varepsilon}_1^2} & \tilde{\varepsilon}_1 & 1 & u_1\tilde{\varepsilon}_1 & u_1 \\ \frac{1}{1+\tilde{\varepsilon}_2^2} & \frac{\tilde{\varepsilon}_2}{1+\tilde{\varepsilon}_2^2} & \tilde{\varepsilon}_2 & 1 & u_2\tilde{\varepsilon}_2 & u_2 \\ \vdots & \vdots & \vdots & \vdots & \vdots & \vdots \\ \frac{1}{1+\tilde{\varepsilon}_M^2} & \frac{\tilde{\varepsilon}_M}{1+\tilde{\varepsilon}_M^2} & \tilde{\varepsilon}_M & 1 & u_M\tilde{\varepsilon}_M & u_M \end{pmatrix}, \tag{C.16}$$

(C.17)

$$u_i = \frac{1}{\Gamma_{\mathrm{f}}}\left[\frac{2k_{\mathrm{f}}\tilde{\varepsilon}_i + l_{\mathrm{f}}(\tilde{\varepsilon}_i^2 - 1)}{(1+\tilde{\varepsilon}_i^2)^2} - m_{\mathrm{f}}\right], \tag{C.18}$$

(C.19)

$$\tilde{\varepsilon}_i = \frac{E_i - E_{0\mathrm{f}}}{\Gamma_{\mathrm{f}}}. \tag{C.20}$$

$(\nabla\alpha)^{\mathrm{T}}$ in the six-dimensional parameter space $(k, l, m, n, \Gamma, E_0)$ is given by

$$(\nabla\alpha)^{\mathrm{T}} = \frac{1}{k^2+l^2}(l, -k, 0, 0, 0, 0). \tag{C.21}$$

C.5 Asymmetric and Dip-Like Fano Line Shapes

The presented fit routine is applicable to all Fano line shapes. Two examples may serve as an illustration. Figure C.5(a) shows $\mathrm{d}I/\mathrm{d}V$ data obtained with a STM tip terminated by a single Co atom atop pristine Au(1 1 0). The spectroscopic feature is described by an asymmetric Fano profile and reflects the Abrikosov-Suhl resonance of the Co atom at the tip apex. The best fit (full line) to the data (dots) according to Eq. (5.4) yields $q_{\mathrm{f}} = 1.29$, $\Gamma_{\mathrm{f}} = 12.6\,\mathrm{meV}$, $E_{0\mathrm{f}} = -1.6\,\mathrm{meV}$ and a 95 % confidence interval of $1.14 < q < 1.46$. The χ^2 map [Fig. C.5(b)] shows a global minimum (asterisk) and, thus, the independence of the fit of initially guessed values.

Single Co atoms adsorbed on Cu(1 1 1) exhibit the Kondo effect with a dip-like Kondo resonance [Fig. C.5(c)]. The best fit to the data yields $q_{\mathrm{f}} = 0.024$, $\Gamma_{\mathrm{f}} = 4.5\,\mathrm{meV}$, $E_{0\mathrm{f}} = 1.9\,\mathrm{meV}$ and a 95 % confidence interval of $-0.016 < q < 0.064$, close to the previously reported values [54]. The χ^2 map is depicted in Fig. C.5(d) with the indicated global minimum.

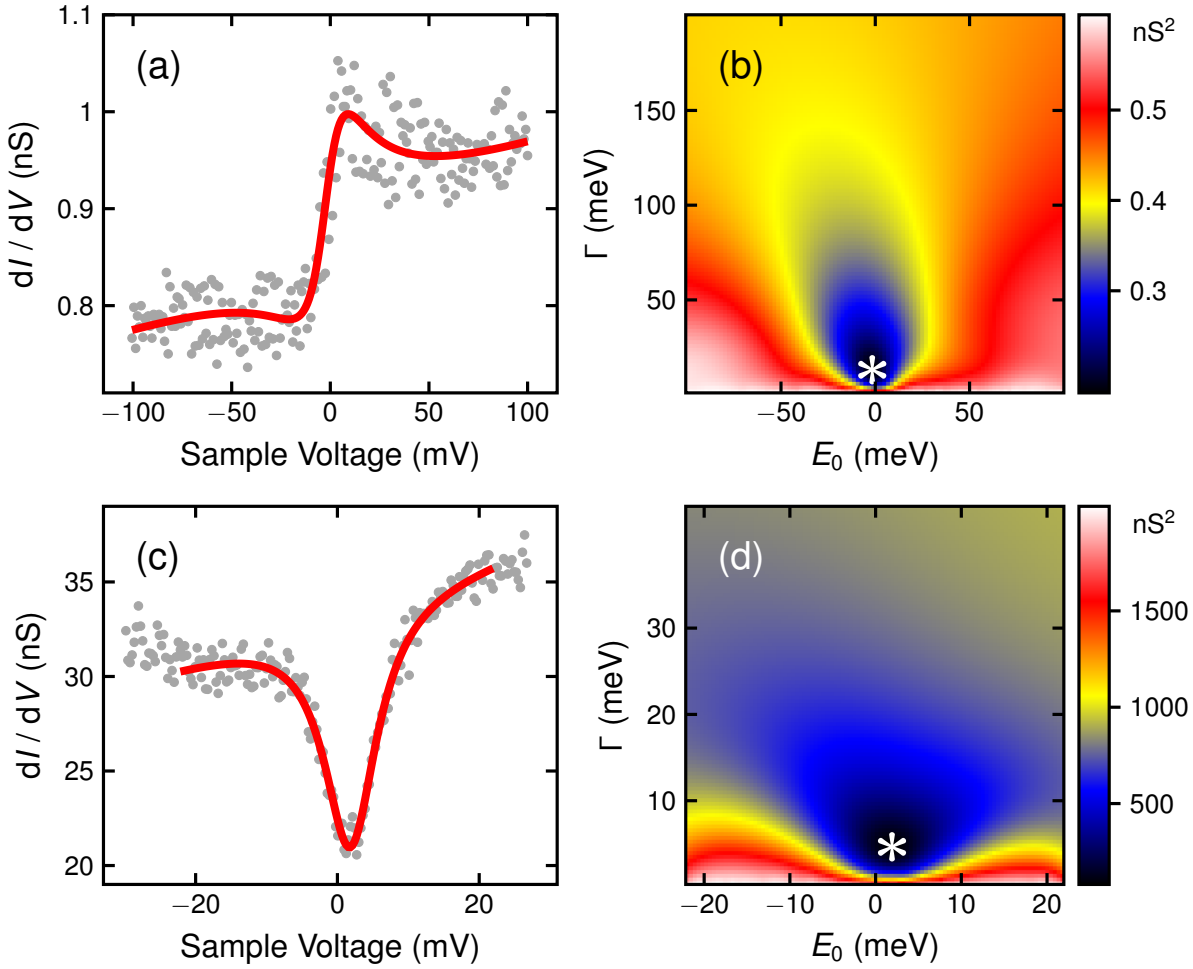

Figure C.5 (a) Spectrum of $\mathrm{d}I/\mathrm{d}V$ (dots) acquired with a STM tip terminated by a single Co atom atop pristine Au(1 1 0) (feedback loop parameters: 1 nA, 100 mV). The full line represents the best fit to the data using the improved parameterization of the fit function [Eq. (5.4)]. **(b)** Map of χ^2 for the data in (a). **(c)** Like (a) for a single Co atom adsorbed to Cu(1 1 1) (feedback loop parameters: 1 nA, 30 mV). **(d)** Like (b) for the data in (c). The asterisks in (b) and (d) indicate the global minimum of χ^2. *This figure was reproduced [91] with permission from AIP.*

D Line Shapes of Vibrational Quanta in IETS

D.1 Fit Procedure

Experimentally acquired $(\mathrm{d}^2I/\mathrm{d}V^2)_{\mathrm{exp}}$ spectra were divided by $(\mathrm{d}I/\mathrm{d}V)_{\mathrm{exp}}$ and then fit on the basis of Eq. (6.1). Numerical differentiation of Eq. (6.1)) with respect to the bias voltage V yielded $(\mathrm{d}^2I/\mathrm{d}V^2)_0$. Broadening due to the finite temperature and the bias voltage modulation were taken into account by convolution of $(\mathrm{d}^2I/\mathrm{d}V^2)_0$ with $\chi_{\mathrm{therm},2}$ [Eq. (2.7)] and $\chi_{\mathrm{mod},2}$ [Eq. (2.9)], *i. e.*, [52]

$$(\mathrm{d}^2I/\mathrm{d}V^2)_{\mathrm{exp}}/(\mathrm{d}I/\mathrm{d}V)_{\mathrm{exp}} = (\mathrm{d}^2I/\mathrm{d}V^2)_0 * \chi_{\mathrm{therm},2} * \chi_{\mathrm{mod},2}. \tag{D.22}$$

A linear background, $vV + w$, was further considered in the fit algorithm. The resulting function was then fit to the experimental data acquired at $T = 6.3\,\mathrm{K}$ and with $V_{\mathrm{mod}} = 4.24\,\mathrm{mV}$. The molecular resonance energy, E_{M}, and its full width at half maximum, Γ_{M}, served as input parameters, extracted from $\mathrm{d}I/\mathrm{d}V$ data. Therefore, the fit was performed with four fit parameters, *i. e.*, u, $\hbar\omega$ (Eq. (6.1)) and v, w (linear background). For all fits the cutoff energy was set to a fixed value of $\Delta = 1\,\mathrm{meV}$. In a wide range of cutoff energies, $0.01\,\mathrm{meV} \leq \Delta \leq 10\,\mathrm{meV}$, the four fit parameters ($\hbar\omega$,u, v, w) did not change. This is reasonable, since the term containing $\ln(\Delta)$ vanishes in the differentiation.

D.2 Vibrational Lines Shapes

Figure D.6 shows experimental data (circles) for those C_{60} vibrational modes that exhibit the transition from peak-like to dip-like line shapes. The data were obtained with a bare Pb tip atop the center of a **5**–C_{60} molecule. The full black lines reflect fits to the data on the basis of Eq. (6.1) and the additional broadening by $\chi_{\mathrm{therm},2}$, $\chi_{\mathrm{mod},2}$ [Eqs. (2.7), (2.9)]. The spectral range of the LUMO, $E_{\mathrm{M}} - \Gamma_{\mathrm{M}}/2 \leq \mathrm{e}V \leq E_{\mathrm{M}} + \Gamma_{\mathrm{M}}/2$, is indicated by the gray shaded area. The C_{60} vibrational modes that are well outside the LUMO spectral range exhibit dip-like [Figs. D.6(a)–(c), left panels] and peak-like [Fig. D.6(a), right panel] line shapes, as expected for non-resonant inelastic tunneling. The C_{60} vibrational modes with

appreciable spectral overlap with the LUMO [Figs. D.6(b), (c), right panels] exhibit an asymmetric [Fig. D.6(b)] or even a dip-like [Fig. D.6(c)] line shape.

Figure D.7 is analogous to Fig. D.6 and shows normalized $\mathrm{d}^2I/\mathrm{d}V^2$ spectra of C_{60} molecules terminating the Pb tip apex and acquired above bare Pb(1 1 1). In Fig. D.7(a) the C_{60} at the tip apex exhibits its LUMO at −197 mV with a FWHM of 236 mV in spectra of $\mathrm{d}I/\mathrm{d}V$. The resulting vibrational spectra are labeled *A* in the main text. Due to the spectral overlap of C_{60} vibrational modes with the LUMO their line shapes appear asymmetric at negative bias voltage (left panel). At positive voltage (right), *i. e.*, well separated from the LUMO spectral range, the vibrational modes adopt peak-like line shapes as expected for non-resonant inelastic tunneling. Shifting the LUMO spectral range away from vibrational energies [Fig. D.7(b), $E_\mathrm{M} = -506$ meV, $\Gamma_\mathrm{M} = 270$ meV, spectrum *B* in the main text] the line shapes of C_{60} vibrational quanta adopt dip-like and peak-like profiles at negative (left) and positive (right) bias voltages, respectively, which reflects the non-resonant case. In order to compare the vibrational energies extracted from the fit routine with previously reported values [26, 80] we have collected these data in Tables D.1, D.2.

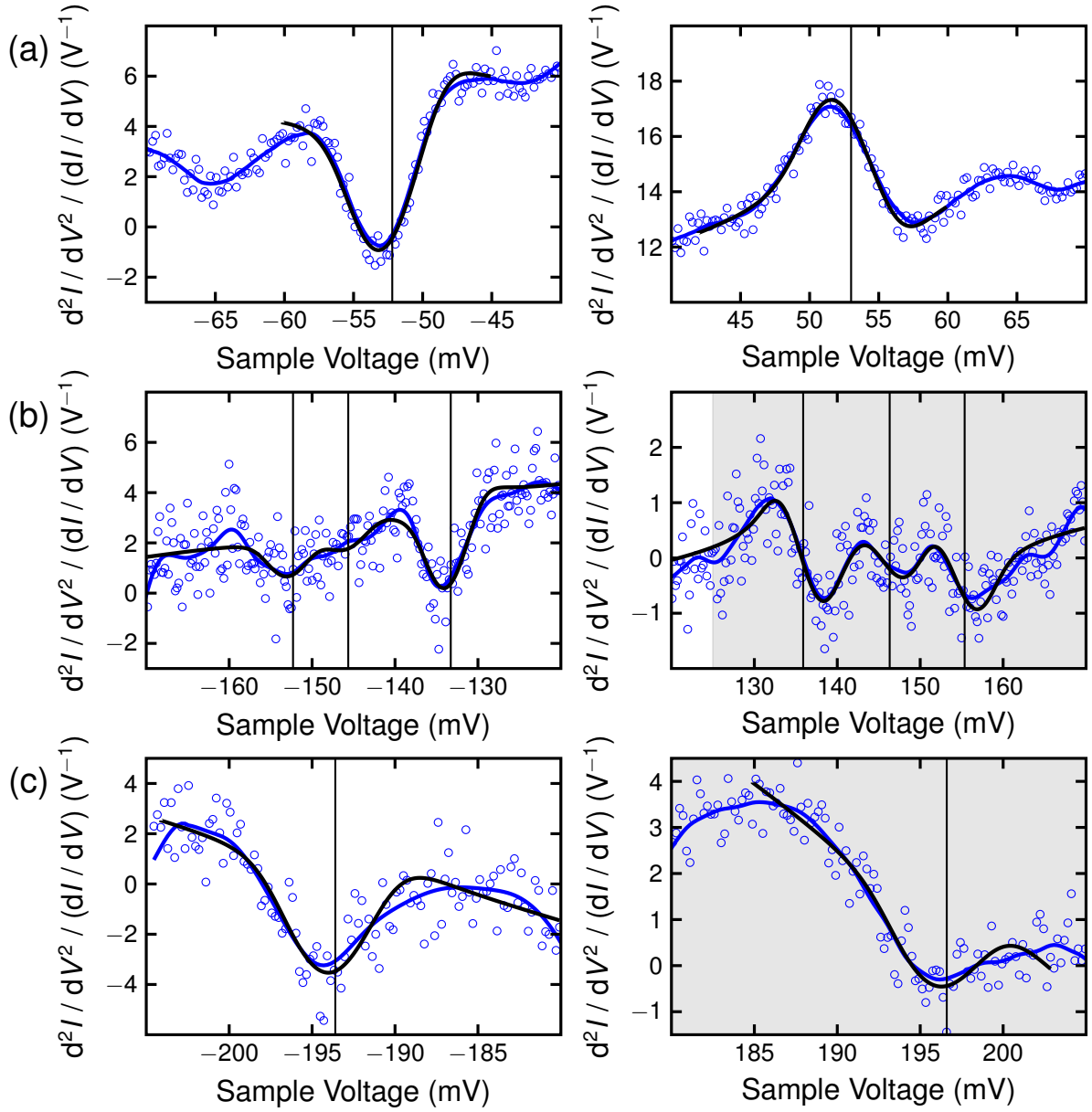

Figure D.6 Normalized d^2I/dV^2 spectra (circles) acquired with a Pb tip atop the center of a **5**-C_{60} molecule adsorbed on Pb(1 1 1) together with fits (black lines) on the basis of Eq.(6.1). **(a)** The $H_g(2)$ (52 meV) vibrational mode appears with a dip-like and peak-like line shape at −52 mV and 52 mV, respectively. **(b)** Vibrational spectra of $H_g(5)$ (134 meV), $T_{1u}(3)$ (146 meV), $H_g(6)$ (155 meV). At negative bias voltage (left), *i. e.*, well outside the LUMO spectral range, these modes appear with a dip-like line shape. At positive bias voltage (right) they adopt an asymmetric line shape. An additional background was subtracted to see the spectroscopic signatures of vibrational quanta most clearly. **(c)** d^2I/dV^2 spectrum of the $H_g(8)$ (195 meV) mode with dip-like line shapes at negative (left) and positive (right) bias voltage. For clarity smoothed experimental data are presented as blue lines. Vertical lines indicate the bias voltages corresponding to the vibrational energies extracted from the fit. The shaded areas depict the LUMO spectral range, as introduced in the main text. Acqusition parameters are given in Fig. 6.4. *This figure was reproduced [92] with permission from ACS.*

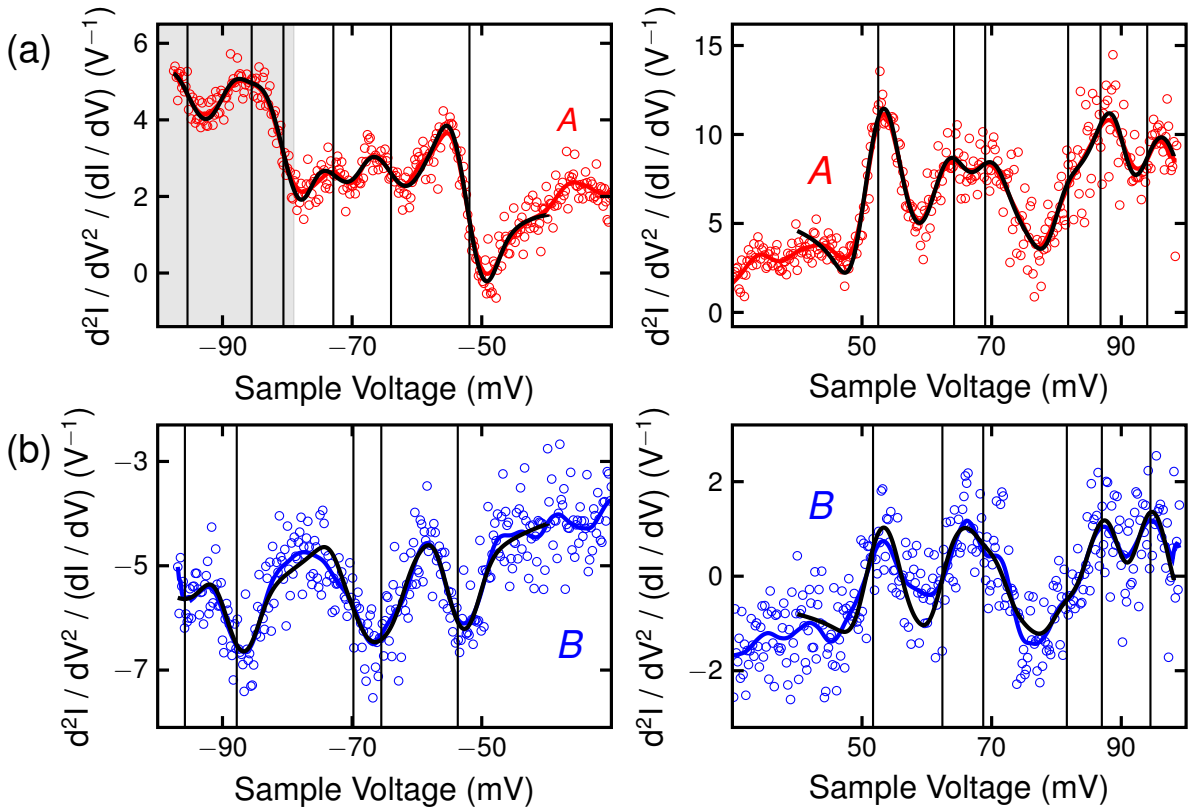

Figure D.7 Normalized d^2I/dV^2 spectra (circles) acquired with C_{60}-terminated Pb tips above bare Pb(1 1 1) together with fits (black lines) on the basis of Eq. (6.1). **(a)** Spectra obtained with a tip where the C_{60} LUMO is located at −197 mV with a FWHM of 236 mV. The C_{60} vibrational modes at negative bias voltage (left panel) fall well into the LUMO spectral range (gray shaded area) and exhibit asymmetric, rather than dip-like, line shapes. At positive bias voltage (right) the line shapes of the C_{60} vibrational modes adopt a peak-like profile. **(b)** Spectra obtained with a tip where the C_{60} LUMO is located at −506 mV with a FWHM of 270 mV. C_{60} vibrational modes appear as dips (peaks) at negative (positive) bias voltage. For clarity smoothed experimental data are presented as red (a) and blue (b) lines. Vertical lines indicate the bias voltages corresponding to the vibrational energies extracted from the fit. Acqusition parameters are given in Fig. 6.5. *This figure was reproduced [92] with permission from ACS.*

Mode	$\hbar\omega_+$	$\hbar\omega_-$	$\hbar\omega$ [26]	$\hbar\omega$ [80]
$H_g(2)$	53.1	52.2	52	53
$H_g(5)$	135.9	133.3	137	135
$H_g(6)$	155.4	152.3	155	155
$H_g(7)$	176.5	174.6	175	176
$H_g(8)$	196.6	193.7	196	197
$T_{1u}(3)$	146.3	145.6		147

Table D.1 Energies of C_{60} vibrational modes extracted from fits shown in Fig. D.6 and reported previously [26, 80]. $\hbar\omega_+$ ($\hbar\omega_-$) is the vibrational energy obtained from the fit of spectral data at positive (negative) bias voltage in this work. All energies are given in meV.

	A		*B*			
Mode	$\hbar\omega_+$	$\hbar\omega_-$	$\hbar\omega_+$	$\hbar\omega_-$	$\hbar\omega$[26]	$\hbar\omega$ [80]
$H_g(2)$	51.7	52.0	52.5	53.7	52	53
$H_g(3)$	87.1	85.5	86.9	87.8	87	88
$H_g(4)$	94.9	95.4	94.0	95.8	97	96
$T_{1u}(1)$	62.5	64.1	64.2	65.6		66
$T_{1u}(2)$	68.7	72.9	69.1	69.8		73
$T_{3u}(2)$	81.6	80.6	81.8			81

Table D.2 Like Table D.1 for vibrational spectroscopy data obtained with C_{60}-terminated Pb tips on Pb(1 1 1) [Fig. D.7]. *A* and *B* denote spectral data acquired with different C_{60} terminations (see main text). All energies are given in meV.

E Molecule Position in IETS

E.1 Deviations from Lorentzian LUMO

Figure E.8(A)–(H) shows maps of the sum of squared residuals χ^2 for fits y^{calc} of the experimental IET data $(V_i, y_i^{\mathrm{exp}})$ shown in Fig. 7.2(b). Maps are labeled according to the molecule labels (A–H). The LUMO parameters Γ_{M} and E_{M} were varied. For each dataset (E_{M}, Γ_{M}) the IET data was fitted on the basis of Eq. (6.1). Subsequently χ^2 was calculated from

$$\chi^2 = \sum_{i=1}^{M} \left| y_i^{\mathrm{exp}} - y^{\mathrm{calc}}(u, \Gamma_{\mathrm{M}}, E_{\mathrm{M}}, \hbar\omega, V_i) \right|^2, \tag{E.23}$$

with M experimental data points. Low values of χ^2 correspond to a good representation of the data by the fit. Minima of χ^2 in the maps [Fig. E.8(A)–(H)] spread out in lines, originating in ($E_{\mathrm{M}} = 175\,\mathrm{meV}$, $\Gamma_{\mathrm{M}} = 0$). This is equivalent with constant $\Gamma_{\mathrm{M}}/E_{\mathrm{M}}$. For some molecules more than one value of $\Gamma_{\mathrm{M}}/E_{\mathrm{M}}$ delivers reasonable fits. However, only for one of these values the prefactor u yields positive values (white line). LUMO parameters (E_{M}, Γ_{M}) acquired from $\mathrm{d}I/\mathrm{d}V$ data of the respective molecule [Fig. 7.2(a)] are shown as white dots. The smallest distance between these points and the adjacent minimum of χ^2 was calculated. The results are shown in Fig. E.8(i). Notably, for most of the data (molecules C–H) the experimental LUMO parameters lie close to the minimum. Larger deviations ($> 30\,\mathrm{meV}$) are found when the shape of the low-energy part of the LUMO deviates from a Lorentzian (molecules A, B). These results emphasize the applied model relies on Lorentzian shaped molecular resonances.

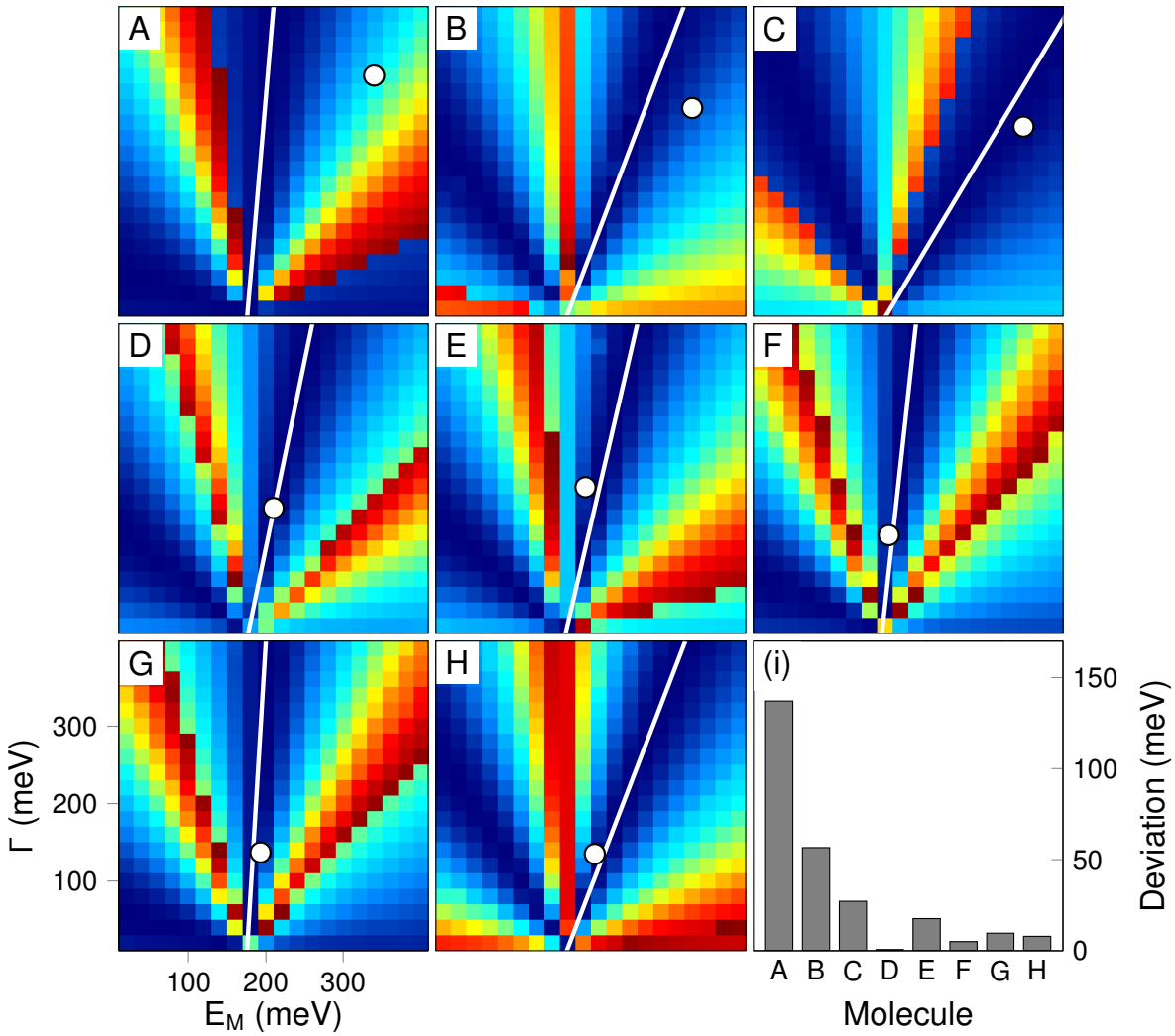

Figure E.8 (A–H) Maps of χ^2 (sum of squared residuals) for fits of the data shown in Fig. 7.2(b) with variable LUMO Parameters Γ_M and E_M. Low values (blue) indicate good representation of the data. Minima spread out from $E_M = 175\,\text{meV}$, $\Gamma_M = 0$ (white lines). Values extracted from Lorentzian fits of $\mathrm{d}I/\mathrm{d}V$ data recorded atop the corresponding molecule [Fig. 7.2(a)] are represented by white dots. Maps are labeled (A – H) according to the molecule, at which the data was recorded. **(i)** Smallest distances between the respective minimum in the maps of χ^2 (A–H) and the parameter set extracted from $\mathrm{d}I/\mathrm{d}V$ data.

E.2 High-Energy LUMO Peak

Determining the peak position of the high-energy LUMO component at increasing conductance is challenging, since the intensity vanishes quickly. Figure E.9(a) shows $\mathrm{d}I/\mathrm{d}V$ spectra at various conductances acquired atop a **5**-C_{60}molecule. In each spectrum a peak at $\approx$ 400 mV could be identified. Some of these peaks are barely visible due to the intense signature of the LE-LUMO component. An enhancement of the feature is obtained by differentiating the $\mathrm{d}I/\mathrm{d}V$ spectrum twice [Fig. E.9(b)]. A dip is found in $\mathrm{d}^3I/\mathrm{d}V^3$ at the position of the peak in $\mathrm{d}I/\mathrm{d}V$. The well-marked feature is situated at $\approx$ 390 meV, varying by less than 10 meV at changing conductance. No conductance-dependent shift comparable to the lower energetic peak is obtained.

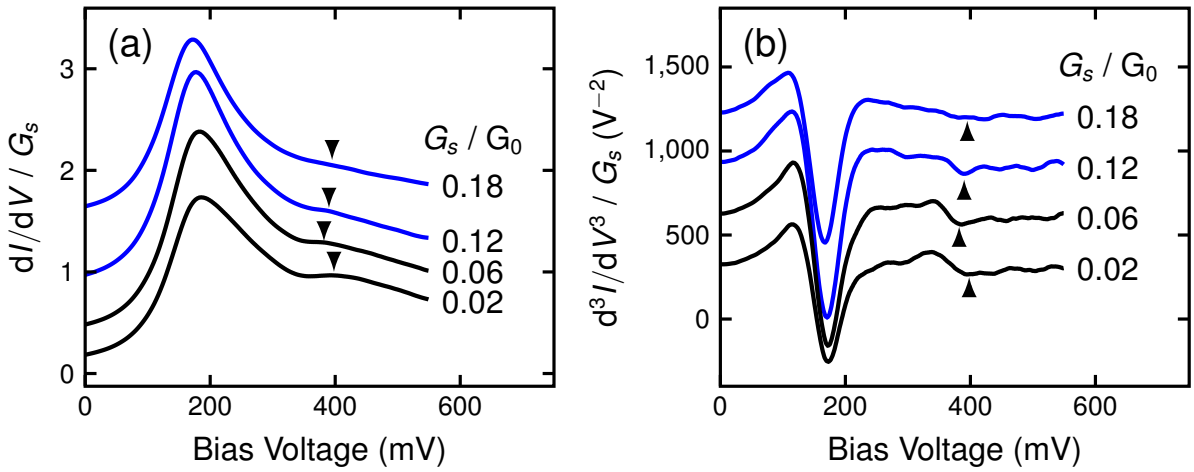

Figure E.9 (a) Normalized $\mathrm{d}I/\mathrm{d}V$ spectra at varying setpoint conductances (labeled to the right of each curve). Conductances are measured prior to opening the feedback loop at each spectrum. The high-energy LUMO peak position is marked for each curve (black triangles). Acqusition parameters are given in Fig. 7.4. **(b)** $\mathrm{d}^3I/\mathrm{d}V^3$ spectra calculated from the data shown in (a). Dips at marked voltages correspond to peak positions in $\mathrm{d}I/\mathrm{d}V$. Colors chosen according to Fig. 7.3(b)

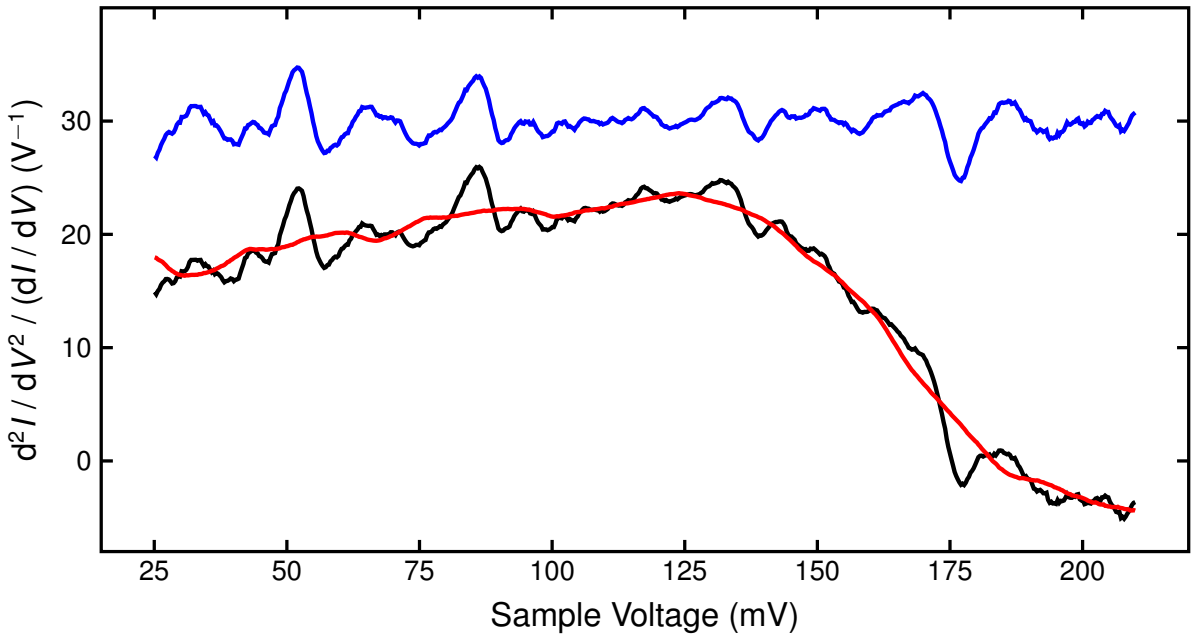

Figure E.10 d^2I/dV^2 spectrum (black line, 300 nA, 210 mV) recorded atop a C_{60} molecule embedded in a hexagonal island on top of a Pb(1 1 1) terrace. Heavily smoothed data serves as an estimation for the elastic background (red line). Background-subtracted data is shown (blue line) as used in Fig. 7.5.

E.3 Background Subtraction

To compare IETS data [Fig. 7.5] recorded at different setpoint conductances a respective background was subtracted in each spectrum. An example of the utilized background subtraction method is shown in Fig. E.10. The elastic background (red curve) was estimated from smoothing of the original data using a moving window average with a window size of 23 mV. The background was subsequently subtracted (blue line) from the original data. Due to the impact of vibrational features on the estimated background small errors can be expected in the background-subtracted result. However, the vibrational line shape (peak-like, dip-like, asymmetric) is essentially preserved.

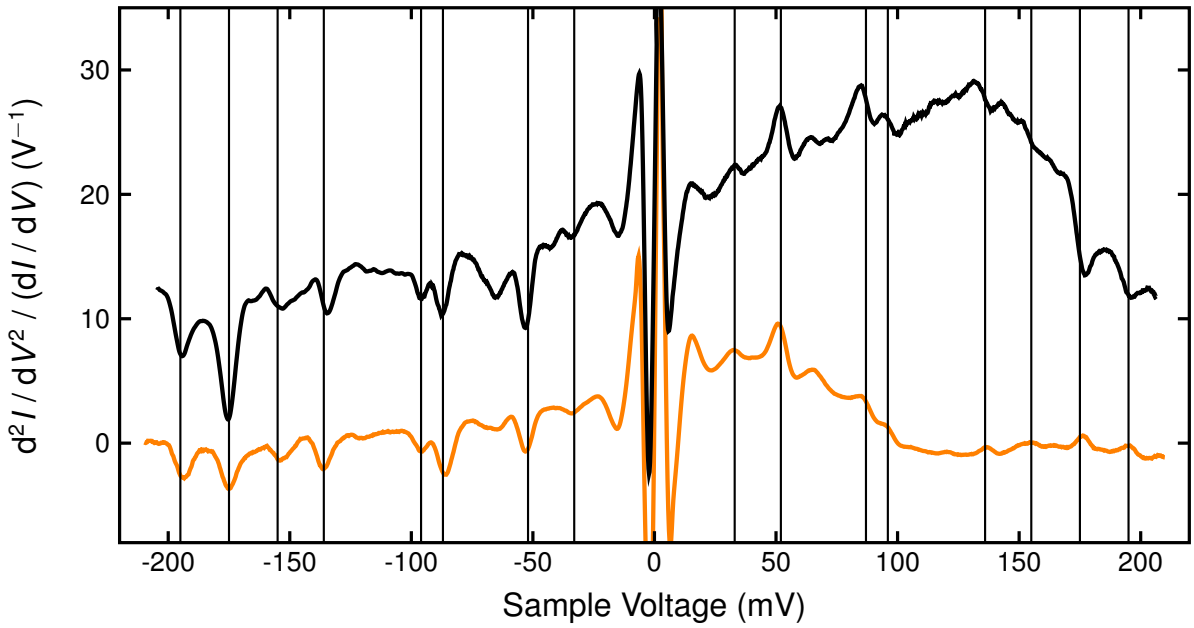

Figure E.11 $\mathrm{d}^2I/\mathrm{d}V^2/\mathrm{d}I/\mathrm{d}V$ spectra acquired atop **5**-C_{60} in tunneling regime (black line) and contact regime (orange line). The tunneling spectrum was composed of four individual spectra covering the voltage ranges $-200\,\mathrm{mV} \leq V \leq -100\,\mathrm{mV}$, $-100\,\mathrm{mV} \leq V \leq 0\,\mathrm{mV}$, $0\,\mathrm{mV} \leq V \leq 100\,\mathrm{mV}$, $100\,\mathrm{mV} \leq V \leq 200\,\mathrm{mV}$. The feedback loop had been disabled at, respectively, $-200\,\mathrm{mV}$, $-100\,\mathrm{mV}$, $100\,\mathrm{mV}$, $200\,\mathrm{mV}$ and 1 nA. The contact regime spectrum was composed of two spectra covering the voltage range $-200\,\mathrm{mV} \leq V \leq 0 \leq 200\,\mathrm{mV}$. The feedback loop was disabled at 8 µA, 210 mV ($G_s = 0.49\,\mathrm{G}_0$). Vertical lines indicate energies of all H_g modes. Spectra were offset for clarity.

E.4 IETS at Negative Voltages

The acquired $\mathrm{d}^2I/\mathrm{d}V^2$ spectra at negative voltages differed only slightly between tunneling and contact regime. Fig E.11 shows two spectra acquired in tunneling regime (black curve) and in contact regime (orange curve). The positive voltage parts are heavily influenced by the LUMO signature (broad background). In tunneling regime the LUMO affects the vibrational line shapes (dips at high voltages). Vibrational features in the contact regime spectrum remain unaffected at positive voltages, thus $\mathrm{d}^2I/\mathrm{d}V^2$ spectra show purely peaks. In negative voltage regime both spectra show purely dips at the voltages corresponding to H_g vibrational energies (vertical lines). Differences are found in intensity and width of the vibrational features. These observations may originate in lower propensity from symmetry changes and additional broadening from electron-hole pair generation through tip states.

E.5 Inelastic and Elastic Terms

The normalized differential conductance correction at positive voltages is given by [23]

$$\begin{aligned} \mathrm{d}I/\mathrm{d}V_{\mathrm{corr}} =& u\frac{\rho_a(0)}{\rho_a(\hbar\omega)}\Bigg[\left|\tilde{M}\right|^2 \Theta(eV-\hbar\omega) - \\ & 2\pi\rho_a(\hbar\omega)\left(\mathrm{Im}\left[\tilde{M}\right]\Theta(eV-\hbar\omega) + \frac{1}{\pi}\mathrm{Re}\left[\tilde{M}\right]\ln\left|\frac{eV-\hbar\omega}{\Delta}\right|\right)\Bigg]. \end{aligned} \tag{E.24}$$

With $\tilde{M} = i\pi\rho_a(\hbar\omega) + \mathscr{P}\int \rho_a(E)(E-\hbar\omega)^{-1}\mathrm{d}E$ and $\mathscr{P}$ the principal value. The positive step accounts for inelastic tunneling processes, the other terms are elastic contributions. For a Lorentzian density of states $\rho_a(E) = \Gamma_{\mathrm{M}}(2\pi[(\Gamma_{\mathrm{M}}/2)^2 + (E-E_{\mathrm{M}})^2)])^{-1}$, the inelastic contribution can be expressed as

$$\mathrm{d}I/\mathrm{d}V_{\mathrm{in}} = \frac{u}{\left(\frac{\Gamma_{\mathrm{M}}}{2}\right)^2 + (E_{\mathrm{M}})^2}\Theta(eV-\hbar\omega) \tag{E.25}$$

and the elastic correction reads

$$\mathrm{d}I/\mathrm{d}V_{\mathrm{el}} = -u\frac{2\left(\frac{\Gamma_{\mathrm{M}}}{2}\right)^2\Theta(eV-\hbar\omega) + (\hbar\omega-E_{\mathrm{M}})\frac{\Gamma_{\mathrm{M}}}{\pi}\ln\left|\frac{eV-\hbar\omega}{\Delta}\right|}{\left[\left(\frac{\Gamma_{\mathrm{M}}}{2}\right)^2 + (E_{\mathrm{M}})^2\right]\left[\left(\frac{\Gamma_{\mathrm{M}}}{2}\right)^2 + (\hbar\omega-E_{\mathrm{M}})^2\right]}. \tag{E.26}$$

List of Figures

List of Tables

List of Publications (2014–2016)

Peer-Reviewed Journal Publications

* S. Meierott, T. Hotz, N. Néel, and J. Kröger:
Asymmetry parameter of peaked Fano line shapes,
Rev. Sci. Instr. **87**, 103901 (2016)

* S. Meierott, N. Néel, and J. Kröger:
Spectroscopic Line Shapes of Vibrational Quanta in the Presence of Molecular Resonances,
J. Phys. Chem. Lett. **7**, 2388-2393 (2016)

* S. Meierott, N. Néel, and J. Kröger:
Kondo effect of single Co atoms on Au(110),
Phys. Rev. B **91**, 201111 (2015)

* T. Kreuch, S. Meierott, N. Néel, W. J. D. Beenken, and J. Kröger:
Atom-by-Atom Dehalogenation of a Porphyrin Molecule Adsorbed on Ag(111),
J. Phys. Chem. C **118**, 30162-30169 (2014)

* T. Sachse, N. Néel, S. Meierott, R. Berndt, W. A. Hofer, and J. Kröger:
Electronic and magnetic states of Mn_2 and Mn_2H on Ag(111),
New Journal of Physics **16**, 063021 (2014)

Given Talks

* S. Meierott, N. Néel and J. Kröger:
Line shapes of C60 vibrational modes in inelastic electron tunnelling spectroscopy,
80. DPG-Jahrestagung und DPG-Frühjahrstagung, O17.5
(Regensburg, Germany, 2016)

* S. Meierott, N. Néel and J. Kröger:
Single-Co Kondo effect on Au(110),
79. DPG-Jahrestagung und DPG-Frühjahrstagung, TT 98.6
(Berlin, Germany, 2015)

* S. Meierott, N. Néel and J. Kröger:
Kondo Effect at Single Co Atoms on Au(110),
Seminar of the Institute of Physics
(Ilmenau, Germany, 2014)

BIBLIOGRAPHY

[1] C. J. Chen, *Introduction to Scanning Tunneling Microscopy* (Oxford Univ. Press, Oxford, 2008).

[2] S. Hüfner, *Photoelectron spectroscopy : principles and applications* (Springer, Berlin, 1996).

[3] P. Larkin, *Infrared and Raman Spectroscopy* (Elsevier, Oxford, 2011).

[4] H. Ibach, *Electron Energy Loss Spectrometers: The Technology of High Performance*, Series in Optical Sciences, Vol. 63 (Springer, Berlin, 1991).

[5] H. Ibach and D. L. Mills, *Electron Energy Loss Spectroscopy and Surface Vibrations* (Academic Press, New York, 1982).

[6] J. Bardeen, L. N. Cooper, and J. R. Schrieffer, Phys. Rev. **108**, 1175 (1957).

[7] S. Nadj-Perge, I. K. Drozdov, J. Li, H. Chen, S. Jeon, J. Seo, A. H. MacDonald, B. A. Bernevig, and A. Yazdani, Science **346**, 602 (2014), http://science.sciencemag.org/content/346/6209/602.full.pdf .

[8] S. Heinze, K. von Bergmann, M. Menzel, J. Brede, A. Kubetzka, R. Wiesendanger, G. Bihlmayer, and S. Blügel, Nat Phys **7**, 713 (2011).

[9] C. Blumenstein, J. Schafer, S. Mietke, S. Meyer, A. Dollinger, M. Lochner, X. Y. Cui, L. Patthey, R. Matzdorf, and R. Claessen, Nat Phys **7**, 776 (2011).

[10] J. Li, W.-D. Schneider, R. Berndt, and B. Delley, Phys. Rev. Lett. **80**, 2893 (1998).

[11] V. Madhavan, W. Chen, T. Jamneala, M. F. Crommie, and N. S. Wingreen, Science **280**, 567 (1998), http://science.sciencemag.org/content/280/5363/567.full.pdf .

[12] M. Ternes, A. J. Heinrich, and W.-D. Schneider, Journal of Physics: Condensed Matter **21**, 053001 (2009).

[13] N. Knorr, M. A. Schneider, L. Diekhöner, P. Wahl, and K. Kern, Phys. Rev. Lett. **88**, 096804 (2002).

[14] M. A. Schneider, L. Vitali, N. Knorr, and K. Kern, Phys. Rev. B **65**, 121406 (2002).

[15] P. Wahl, L. Diekhöner, M. A. Schneider, L. Vitali, G. Wittich, and K. Kern, Phys. Rev. Lett. **93**, 176603 (2004).

[16] V. Madhavan, W. Chen, T. Jamneala, M. F. Crommie, and N. S. Wingreen, Phys. Rev. B **64**, 165412 (2001).

[17] A. Gumbsch, G. Barcaro, M. G. Ramsey, S. Surnev, A. Fortunelli, and F. P. Netzer, Phys. Rev. B **81**, 165420 (2010).

[18] A. F. Otte, M. Ternes, K. von Bergmann, S. Loth, H. Brune, C. P. Lutz, C. F. Hirjibehedin, and A. J. Heinrich, Nat Phys **4**, 847 (2008).

[19] J. Ren, H. Guo, J. Pan, Y. Y. Zhang, X. Wu, H.-G. Luo, S. Du, S. T. Pantelides, and H.-J. Gao, Nano Letters **14**, 4011 (2014), http://dx.doi.org/10.1021/nl501425n .

[20] J. Henzl and K. Morgenstern, Phys. Rev. Lett. **98**, 266601 (2007).

[21] H. C. Manoharan, C. P. Lutz, and D. M. Eigler, Nature **403**, 512 (2000).

[22] M. Plihal and J. W. Gadzuk, Phys. Rev. B **63**, 085404 (2001).

[23] B. N. J. Persson and A. Baratoff, Phys. Rev. Lett. **59**, 339 (1987).

[24] K. J. Franke and J. I. Pascual, Journal of Physics: Condensed Matter **24**, 394002 (2012).

[25] A. Stróżecka, J. Mysliveček, and B. Voigtländer, Applied Physics A **87**, 475 (2007).

[26] K. J. Franke, G. Schulze, and J. I. Pascual, The Journal of Physical Chemistry Letters **1**, 500 (2010).

[27] H. I. Li, K. J. Franke, J. I. Pascual, L. W. Bruch, and R. D. Diehl, Phys. Rev. B **80**, 085415 (2009).

[28] G. Schull, T. Frederiksen, M. Brandbyge, and R. Berndt, Phys. Rev. Lett. **103**, 206803 (2009).

[29] N. Hauptmann, F. Mohn, L. Gross, G. Meyer, T. Frederiksen, and R. Berndt, New Journal of Physics **14**, 073032 (2012).

[30] B. C. Stipe, M. A. Rezaei, and W. Ho, Science **280**, 1732 (1998), http://science.sciencemag.org/content/280/5370/1732.full.pdf .

[31] Y. Wang, E. Kioupakis, X. Lu, D. Wegner, R. Yamachika, J. E. Dahl, R. M. K. Carlson, S. G. Louie, and M. F. Crommie, Nat Mater **7**, 38 (2008).

[32] A. Stróżecka, K. Muthukumar, J. Larsson, A. Dybek, T. S. Dennis, J. Mysliveček, and B. Voigtländer, Phys. Rev. B **83**, 165414 (2011).

[33] N. Okabayashi, A. Gustafsson, A. Peronio, M. Paulsson, T. Arai, and F. J. Giessibl, Phys. Rev. B **93**, 165415 (2016).

[34] C. Xu, C.-l. Chiang, Z. Han, and W. Ho, Phys. Rev. Lett. **116**, 166101 (2016).

[35] J. R. Hahn, H. J. Lee, and W. Ho, Phys. Rev. Lett. **85**, 1914 (2000).

[36] J. R. Hahn and W. Ho, Phys. Rev. B **80**, 165428 (2009).

[37] J. Hihath, C. Bruot, H. Nakamura, Y. Asai, I. DÃ⬡ez-Pérez, Y. Lee, L. Yu, and N. Tao, ACS Nano **5**, 8331 (2011), http://dx.doi.org/10.1021/nn2030644 .

[38] L.-L. Lin, C.-K. Wang, and Y. Luo, ACS Nano **5**, 2257 (2011), http://dx.doi.org/10.1021/nn103522k .

[39] M. Tsutsui and M. Taniguchi, Journal of Applied Physics **113**, 084301 (2013), http://dx.doi.org/10.1063/1.4792048 .

[40] N. Okabayashi, Y. Konda, and T. Komeda, Phys. Rev. Lett. **100**, 217801 (2008).

[41] L. Vitali, R. Ohmann, K. Kern, A. Garcia-Lekue, T. Frederiksen, D. Sanchez-Portal, and A. Arnau, Nano Letters **10**, 657 (2010), http://dx.doi.org/10.1021/nl903760k .

[42] N. L. Schneider, N. Néel, N. P. Andersen, J. T. Lü, M. Brandbyge, J. Kröger, and R. Berndt, Journal of Physics: Condensed Matter **27**, 015001 (2015).

[43] L. C. Davis, Phys. Rev. B **2**, 1714 (1970).

[44] M. Paulsson, T. Frederiksen, H. Ueba, N. Lorente, and M. Brandbyge, Phys. Rev. Lett. **100**, 226604 (2008).

[45] G. Wentzel, Zeitschrift für Physik **38**, 518 (1926).

[46] H. A. Kramers, Zeitschrift für Physik **39**, 828 (1926).

[47] M. L. Brillouin, Comptes Rendus de l'Academie des Sciences **183**, 24 (1926).

[48] C. J. Chen, Journal of Vacuum Science & Technology A **6**, 319 (1988), http://dx.doi.org/10.1116/1.575444 .

[49] J. Li, W.-D. Schneider, and R. Berndt, Phys. Rev. B **56**, 7656 (1997).

[50] C. J. Chen, *Introduction to scanning tunneling microscopy* (Oxford Univ. Press, Oxford, 2008).

[51] J. Lambe and R. C. Jaklevic, Phys. Rev. **165**, 821 (1968).

[52] J. Klein, A. Léger, M. Belin, D. Défourneau, and M. J. L. Sangster, Phys. Rev. B **7**, 2336 (1973).

[53] A. Roychowdhury, M. A. Gubrud, R. Dana, J. R. Anderson, C. J. Lobb, F. C. Wellstood, and M. Dreyer, Review of Scientific Instruments **85**, 043706 (2014).

[54] N. Néel, J. Kröger, R. Berndt, T. O. Wehling, A. I. Lichtenstein, and M. I. Katsnelson, Phys. Rev. Lett. **101**, 266803 (2008).

[55] T. Kreuch, S. Meierott, N. Néel, W. J. D. Beenken, and J. Kröger, The Journal of Physical Chemistry C **118**, 30162 (2014).

[56] J. A. Stroscio and D. M. Eigler, Science **254**, 1319 (1991), http://science.sciencemag.org/content/254/5036/1319.full.pdf .

[57] L. Kouwenhoven and L. Glazman, Physics World **14**, 33 (2001).

[58] W. D. Haas and G. V. D. Berg, Physica **3**, 440 (1936).

[59] J. Kondo, Progress of Theoretical Physics **32**, 37 (1964), http://ptp.oxfordjournals.org/content/32/1/37.full.pdf+html .

[60] P. W. Anderson, Phys. Rev. **124**, 41 (1961).

[61] O. Újsághy, J. Kroha, L. Szunyogh, and A. Zawadowski, Phys. Rev. Lett. **85**, 2557 (2000).

[62] A. A. Abrikosov, Physics **2**, 5 (1965).

[63] A. A. Abrikosov, Physics **2**, 61 (1965).

[64] H. Suhl, in *Theory of Magnetism in Transition Metal*, edited by W. Marshall (Academic, London, 1967) pp. 116–205.

[65] A. Karton, B. Chan, K. Raghavachari, and L. Radom, The Journal of Physical Chemistry A **117**, 1834 (2013), http://dx.doi.org/10.1021/jp312585r .

[66] R. S. Ruoff and A. L. Ruoff, Nature (London) **350**, 663 (1991).

[67] M. Berninger, A. Stefanov, S. Deachapunya, and M. Arndt, Phys. Rev. A **76**, 013607 (2007).

[68] A. F. Hebard, M. J. Rosseinsky, R. C. Haddon, D. W. Murphy, S. H. Glarum, T. T. M. Palstra, A. P. Ramirez, and A. R. Kortan, Nature **350**, 600 (1991).

[69] R. C. Haddon, A. F. Hebard, M. J. Rosseinsky, D. W. Murphy, S. J. Duclos, K. B. Lyons, B. Miller, J. M. Rosamilia, R. M. Fleming, A. R. Kortan, S. H. Glarum, A. V. Makhija, A. J. Muller, R. H. Eick, S. M. Zahurak, R. Tycko, G. Dabbagh, and F. A. Thiel, Nature **350**, 320 (1991).

[70] M. Schlüter, M. Lannoo, M. Needels, G. Baraff, and D. Tománek, Journal of Physics and Chemistry of Solids **53**, 1473 (1992).

[71] D. S. Bethune, G. Meijer, W. C. Tang, H. J. Rosen, W. G. Golden, H. Seki, C. A. Brown, and M. S. de Vries, Chemical Physics Letters **179**, 181 (1991).

[72] P. Bowmar, M. Kurmoo, M. A. Green, F. L. Pratt, W. Hayes, P. Day, and K. Kikuchi, Journal of Physics: Condensed Matter **5**, 2739 (1993).

[73] B. Chase, N. Herron, and E. Holler, The Journal of Physical Chemistry **96**, 4262 (1992), http://dx.doi.org/10.1021/j100190a029 .

[74] Y. Fang, Q.-J. Huang, P. Wang, X.-Y. Li, and N.-T. Yu, Chemical Physics Letters **381**, 255 (2003).

[75] Y. Zhang, G. Edens, and M. J. Weaver, Journal of the American Chemical Society **113**, 9395 (1991), http://dx.doi.org/10.1021/ja00024a070 .

[76] O. Gunnarsson, H. Handschuh, P. S. Bechthold, B. Kessler, G. Ganteför, and W. Eberhardt, Phys. Rev. Lett. **74**, 1875 (1995).

[77] R. L. Cappelletti, J. R. D. Copley, W. A. Kamitakahara, F. Li, J. S. Lannin, and D. Ramage, Phys. Rev. Lett. **66**, 3261 (1991).

[78] G. Gensterblum, J. J. Pireaux, P. A. Thiry, R. Caudano, J. P. Vigneron, P. Lambin, A. A. Lucas, and W. Krätschmer, Phys. Rev. Lett. **67**, 2171 (1991).

[79] J.-L. Brousseau, K. Tian, S. Gauvin, R. Leblanc, and P. Delhaés, Chemical Physics Letters **202**, 521 (1993).

[80] S. Nolen and S. Ruggiero, Chemical Physics Letters **300**, 656 (1999).

[81] G. Schull, N. Néel, M. Becker, J. Kröger, and R. Berndt, New Journal of Physics **10**, 065012 (2008).

[82] F. Penning, Physica **3**, 873 (1936).

[83] M. Pivetta, M. Ternes, F. Patthey, and W.-D. Schneider, Phys. Rev. Lett. **99**, 126104 (2007).

[84] F. Natterer, F. Patthey, and H. Brune, Surface Science **615**, 80 (2013).

[85] G. Binnig, H. Rohrer, C. Gerber, and E. Weibel, Phys. Rev. Lett. **49**, 57 (1982).

[86] N. Néel, J. Kröger, L. Limot, T. Frederiksen, M. Brandbyge, and R. Berndt, Phys. Rev. Lett. **98**, 065502 (2007).

[87] M. Kunz, *Aufbau eines Rastertunnelmikroskops für Messungen bei tiefen Temperaturen*, Master's thesis, Technische Universität Ilmenau, Ilmenau (2011).

[88] S. Meierott, *Optimierung und Inbetriebnahme eines Ultrahochvakuum-Tieftemperatur-Rastertunnelmikroskops und erste Messungen an der Ag(111)-Oberfläche*, Master's thesis, Technische Universität Ilmenau, Ilmenau (2013).

[89] D. R. Smith and F. R. Fickett, J. Res. Natl. Inst. Stand. Technol. **100**, 119 (1995).

[90] S. Meierott, N. Néel, and J. Kröger, Phys. Rev. B **91**, 201111 (2015).

[91] S. Meierott, T. Hotz, N. Néel, and J. Kröger, Review of Scientific Instruments **87**, 103901 (2016).

[92] S. Meierott, N. Néel, and J. Kröger, The Journal of Physical Chemistry Letters **7**, 2388 (2016).

[93] H. Prüser, M. Wenderoth, P. E. Dargel, A. Weismann, R. Peters, T. Pruschke, and R. G. Ulbrich, Nat Phys **7**, 203 (2011).

[94] H. Prüser, M. Wenderoth, A. Weismann, and R. G. Ulbrich, Phys. Rev. Lett. **108**, 166604 (2012).

[95] P. Wahl, A. P. Seitsonen, L. Diekhöner, M. A. Schneider, and K. Kern, New Journal of Physics **11**, 113015 (2009).

[96] J. Merino and O. Gunnarsson, Phys. Rev. B **69**, 115404 (2004).

[97] C.-Y. Lin, A. H. Castro Neto, and B. A. Jones, Phys. Rev. Lett. **97**, 156102 (2006).

[98] C.-Y. Lin, A. H. Castro Neto, and B. A. Jones, Phys. Rev. B **71**, 035417 (2005).

[99] A. Schiller and S. Hershfield, Phys. Rev. B **61**, 9036 (2000).

[100] Y. Jiang, Y. N. Zhang, J. X. Cao, R. Q. Wu, and W. Ho, Science **333**, 324 (2011), http://science.sciencemag.org/content/333/6040/324.full.pdf .

[101] D. Nečas and P. Klapetek, Central European Journal of Physics **10**, 181 (2012).

[102] T. Jasper-Tönnies, *Dichtefunktionalrechnungen zur Struktur und Dynamik der Wechselwirkung von Co- und Au-Atomen mit Au(110)*, Master's thesis, University of Kiel, Kiel (2010).

[103] W. A. Hofer, G. Teobaldi, and N. Lorente, Nanotechnology **19**, 305701 (2008).

[104] F. Donati, Q. Dubout, G. Autès, F. Patthey, F. Calleja, P. Gambardella, O. V. Yazyev, and H. Brune, Phys. Rev. Lett. **111**, 236801 (2013).

[105] W. A. Hofer, K. Palotás, S. Rusponi, T. Cren, and H. Brune, Phys. Rev. Lett. **100**, 026806 (2008).

[106] L. Liu, K. Yang, Y. Jiang, B. Song, W. Xiao, L. Li, H. Zhou, Y. Wang, S. Du, M. Ouyang, W. A. Hofer, A. H. Castro Neto, and H.-J. Gao, Scientific Reports **3**, 1210 (2013).

[107] T. Sachse, N. Néel, S. Meierott, R. Berndt, W. A. Hofer, and J. Kröger, New Journal of Physics **16**, 063021 (2014).

[108] S. D. Borisova, S. V. Eremeev, G. G. Rusina, V. S. Stepanyuk, P. Bruno, and E. V. Chulkov, Phys. Rev. B **78**, 075428 (2008).

[109] N. Quaas, M. Wenderoth, A. Weismann, R. G. Ulbrich, and K. Schönhammer, Phys. Rev. B **69**, 201103 (2004).

[110] N. Néel, J. Kröger, L. Limot, K. Palotas, W. A. Hofer, and R. Berndt, Phys. Rev. Lett. **98**, 016801 (2007).

[111] L. Vitali, R. Ohmann, S. Stepanow, P. Gambardella, K. Tao, R. Huang, V. S. Stepanyuk, P. Bruno, and K. Kern, Phys. Rev. Lett. **101**, 216802 (2008).

[112] N. Néel, R. Berndt, J. Kröger, T. O. Wehling, A. I. Lichtenstein, and M. I. Katsnelson, Phys. Rev. Lett. **107**, 106804 (2011).

[113] D.-J. Choi, M. V. Rastei, P. Simon, and L. Limot, Phys. Rev. Lett. **108**, 266803 (2012).

[114] A. C. Hewson, *The Kondo Problem to Heavy Fermions* (Cambridge Univ. Press, Cambridge, 1993).

[115] M. A. Schneider, P. Wahl, L. Diekhöner, L. Vitali, G. Wittich, and K. Kern, Japanese Journal of Applied Physics **44**, 5328 (2005).

[116] A. E. Miroshnichenko, S. Flach, and Y. S. Kivshar, Rev. Mod. Phys. **82**, 2257 (2010).

[117] E. Majorana, Il Nuovo Cimento (1924-1942) **8**, 78 (1931).

[118] E. Majorana, Il Nuovo Cimento (1924-1942) **8**, 107 (1935).

[119] U. Fano, Il Nuovo Cimento (1924-1942) **12**, 154 (1935).

[120] U. Fano, Phys. Rev. **124**, 1866 (1961).

[121] D. L. Rousseau and S. P. S. Porto, Phys. Rev. Lett. **20**, 1354 (1968).

[122] A. Nitzan and J. Jortner, Molecular Physics **24**, 109 (1972).

[123] L. A. O. Nunes, L. Ioriatti, L. T. Florez, and J. P. Harbison, Phys. Rev. B **47**, 13011 (1993).

[124] Y. J. Chabal, Phys. Rev. Lett. **55**, 845 (1985).

[125] J. Kröger, S. Lehwald, and H. Ibach, Phys. Rev. B **55**, 10895 (1997).

[126] J. Kröger, D. Bruchmann, S. Lehwald, and H. Ibach, Surface Science **449**, 227 (2000).

[127] J. Kröger, Reports on Progress in Physics **69**, 899 (2006).

[128] F. S. Tautz, M. Eremtchenko, J. A. Schaefer, M. Sokolowski, V. Shklover, and E. Umbach, Phys. Rev. B **65**, 125405 (2002).

[129] S. Kohler, J. Lehmann, and P. Hänggi, Physics Reports **406**, 379 (2005).

[130] V. Y. Aleshkin, A. V. Antonov, L. V. Gavrilenko, and V. I. Gavrilenko, Phys. Rev. B **75**, 125201 (2007).

[131] A. Christ, S. G. Tikhodeev, N. A. Gippius, J. Kuhl, and H. Giessen, Phys. Rev. Lett. **91**, 183901 (2003).

[132] J. Aizpurua, T. Taubner, F. J. G. de Abajo, M. Brehm, and R. Hillenbrand, Opt. Express **16**, 1529 (2008).

[133] W. Chen, T. Jamneala, V. Madhavan, and M. F. Crommie, Phys. Rev. B **60**, R8529 (1999).

[134] T. Jamneala, V. Madhavan, and M. F. Crommie, Phys. Rev. Lett. **87**, 256804 (2001).

[135] P. Wahl, P. Simon, L. Diekhöner, V. S. Stepanyuk, P. Bruno, M. A. Schneider, and K. Kern, Phys. Rev. Lett. **98**, 056601 (2007).

[136] T. Uchihashi, J. Zhang, J. Kröger, and R. Berndt, Phys. Rev. B **78**, 033402 (2008).

[137] N. Néel, J. Kröger, and R. Berndt, Phys. Rev. B **82**, 233401 (2010).

[138] Y.-h. Zhang, S. Kahle, T. Herden, C. Stroh, M. Mayor, U. Schlickum, M. Ternes, P. Wahl, and K. Kern, Nature Communications **4**, 2110 (2013).

[139] K. Levenberg, Q. Appl. Math. **2**, 164 (1944).

[140] D. W. Marquardt, Journal of the Society for Industrial and Applied Mathematics **11**, 431 (1963), http://dx.doi.org/10.1137/0111030 .

[141] R. W. Cunningham, Computers in Physics **7**, 570 (1993).

[142] B. W. Shore, J. Opt. Soc. Am. **57**, 881 (1967).

[143] J. Repp, G. Meyer, S. M. Stojković, A. Gourdon, and C. Joachim, Phys. Rev. Lett. **94**, 026803 (2005).

[144] C. Weiss, C. Wagner, C. Kleimann, M. Rohlfing, F. S. Tautz, and R. Temirov, Phys. Rev. Lett. **105**, 086103 (2010).

[145] C. Wagner, M. F. B. Green, P. Leinen, T. Deilmann, P. Krüger, M. Rohlfing, R. Temirov, and F. S. Tautz, Phys. Rev. Lett. **115**, 026101 (2015).

[146] R. Zhang, Z. Hu, B. Li, and J. Yang, The Journal of Physical Chemistry A **118**, 8953 (2014), http://dx.doi.org/10.1021/jp5018218 .

[147] I. Suominen, J. Nieminen, R. S. Markiewicz, and A. Bansil, Phys. Rev. B **84**, 014528 (2011).

[148] B. W. Heinrich, M. V. Rastei, D.-J. Choi, T. Frederiksen, and L. Limot, Phys. Rev. Lett. **107**, 246801 (2011).

[149] M. Bode, Reports on Progress in Physics **66**, 523 (2003).

[150] R. Wiesendanger, Rev. Mod. Phys. **81**, 1495 (2009).

[151] M. Ziegler, N. Ruppelt, N. Néel, J. Kröger, and R. Berndt, Applied Physics Letters **96**, 132505 (2010), http://dx.doi.org/10.1063/1.3377917 .

[152] K. Palotás, W. A. Hofer, and L. Szunyogh, Phys. Rev. B **83**, 214410 (2011).

[153] N. Lorente and M. Persson, Phys. Rev. Lett. **85**, 2997 (2000).

[154] N. Lorente, M. Persson, L. J. Lauhon, and W. Ho, Phys. Rev. Lett. **86**, 2593 (2001).

[155] A. Gagliardi, G. C. Solomon, A. Pecchia, T. Frauenheim, A. Di Carlo, N. S. Hush, and J. R. Reimers, Phys. Rev. B **75**, 174306 (2007).

[156] G. Teobaldi, M. Peñalba, A. Arnau, N. Lorente, and W. A. Hofer, Phys. Rev. B **76**, 235407 (2007).

[157] L. Bartels, G. Meyer, and K.-H. Rieder, Surface Science **432**, L621 (1999).

[158] F. Moresco, G. Meyer, and K. H. Rieder, Modern Physics Letters B **13**, 709 (1999), http://www.worldscientific.com/doi/pdf/10.1142/S0217984999000890 .

[159] J. R. Hahn and W. Ho, Phys. Rev. Lett. **87**, 196102 (2001).

[160] A. Garcia-Lekue, D. Sanchez-Portal, A. Arnau, and T. Frederiksen, Phys. Rev. B **83**, 155417 (2011).

[161] A. Baratoff and B. N. J. Persson, Journal of Vacuum Science & Technology A **6**, 331 (1988), http://dx.doi.org/10.1116/1.575407 .

[162] B. N. J. Persson, Physica Scripta **38**, 282 (1988).

[163] M. Alducin, D. Sánchez-Portal, A. Arnau, and N. Lorente, Phys. Rev. Lett. **104**, 136101 (2010).

[164] S. Monturet, M. Alducin, and N. Lorente, Phys. Rev. B **82**, 085447 (2010).

[165] H. Song, Y. Kim, Y. H. Jang, H. Jeong, M. A. Reed, and T. Lee, Nature **462**, 1039 (2009).

[166] I. D. Hands, J. L. Dunn, and C. A. Bates, Phys. Rev. B **81**, 205440 (2010).

[167] A. J. Lakin, C. Chiutu, A. M. Sweetman, P. Moriarty, and J. L. Dunn, Phys. Rev. B **88**, 035447 (2013).

[168] K. F. Kelly, D. Sarkar, S. Prato, J. S. Resh, G. D. Hale, and N. J. Halas, Journal of Vacuum Science & Technology B **14**, 593 (1996), http://avs.scitation.org/doi/pdf/10.1116/1.589141 .

[169] F. Negri, G. Orlandi, and F. Zerbetto, Chemical Physics Letters **190**, 174 (1992).

[170] W. Ho, The Journal of Chemical Physics **117**, 11033 (2002), http://dx.doi.org/10.1063/1.1521153 .

[171] N. Lorente, R. Rurali, and H. Tang, Journal of Physics: Condensed Matter **17**, S1049 (2005).

[172] S.-W. Hla, Journal of Vacuum Science & Technology B **23**, 1351 (2005), http://avs.scitation.org/doi/pdf/10.1116/1.1990161 .

[173] K. Morgenstern, N. Lorente, and K.-H. Rieder, Physica Status Solidi B **250**, 1671 (2013).

[174] C. Silien, N. A. Pradhan, W. Ho, and P. A. Thiry, Phys. Rev. B **69**, 115434 (2004).

[175] G. Schulze, K. J. Franke, and J. I. Pascual, New Journal of Physics **10**, 065005 (2008).

[176] D. R. Daughton and J. A. Gupta, Applied Physics Letters **98**, 133303 (2011), http://dx.doi.org/10.1063/1.3569719 .

[177] O. Tal, M. Kiguchi, W. H. A. Thijssen, D. Djukic, C. Untiedt, R. H. M. Smit, and J. M. van Ruitenbeek, Phys. Rev. B **80**, 085427 (2009).

[178] R. H. M. Smit, Y. Noat, C. Untiedt, N. D. Lang, M. C. van Hemert, and J. M. van Ruitenbeek, Nature **419**, 906 (2002).

[179] D. Djukic, K. S. Thygesen, C. Untiedt, R. H. M. Smit, K. W. Jacobsen, and J. M. van Ruitenbeek, Phys. Rev. B **71**, 161402 (2005).

[180] N. Agraït, C. Untiedt, G. Rubio-Bollinger, and S. Vieira, Phys. Rev. Lett. **88**, 216803 (2002).

[181] M. Galperin, M. A. Ratner, and A. Nitzan, The Journal of Chemical Physics **121**, 11965 (2004), http://dx.doi.org/10.1063/1.1814076 .

[182] W. Wang, T. Lee, I. Kretzschmar, and M. A. Reed, Nano Letters **4**, 643 (2004), http://dx.doi.org/10.1021/nl049870v .

[183] J. Guo, J.-T. Lü, Y. Feng, J. Chen, J. Peng, Z. Lin, X. Meng, Z. Wang, X.-Z. Li, E.-G. Wang, and Y. Jiang, Science **352**, 321 (2016), http://science.sciencemag.org/content/352/6283/321.full.pdf .

[184] K. J. Franke, G. Schulze, N. Henningsen, I. Fernández-Torrente, J. I. Pascual, S. Zarwell, K. Rück-Braun, M. Cobian, and N. Lorente, Phys. Rev. Lett. **100**, 036807 (2008).

[185] J. Tersoff and D. R. Hamann, Phys. Rev. B **31**, 805 (1985).

[186] J. Hihath, C. Bruot, and N. Tao, ACS Nano **4**, 3823 (2010), http://dx.doi.org/10.1021/nn100470s .

[187] J. Hihath, C. R. Arroyo, G. Rubio-Bollinger, N. Tao, and N. AgraÃŕt, Nano Letters **8**, 1673 (2008), http://dx.doi.org/10.1021/nl080580e .

[188] R. Frisenda, M. L. Perrin, and H. S. J. van der Zant, Beilstein Journal of Nanotechnology **6**, 2477 (2015).

[189] A. J. Lupinetti, S. Fau, G. Frenking, and S. H. Strauss, The Journal of Physical Chemistry A **101**, 9551 (1997), http://dx.doi.org/10.1021/jp972657l .

[190] M. Endlich, A. Michl, J. Hildisch, S. Müller, and J. Kröger, The Journal of Physical Chemistry C **120**, 11490 (2016), http://dx.doi.org/10.1021/acs.jpcc.6b01399 .

[191] A. V. Tuchin, L. A. Bityutskaya, and E. N. Bormontov, The European Physical Journal D **69**, 87 (2015).

[192] Y. Huang, D. F. R. Gilson, and I. S. Butler, The Journal of Physical Chemistry **95**, 5723 (1991), http://dx.doi.org/10.1021/j100168a005 .

[193] M. Paulsson, T. Frederiksen, and M. Brandbyge, Phys. Rev. B **72**, 201101 (2005).

[194] M. Paulsson, T. Frederiksen, and M. Brandbyge, Journal of Physics: Conference Series **35**, 247 (2006).

[195] Z. Han, G. Czap, C. Xu, C.-l. Chiang, D. Yuan, R. Wu, and W. Ho, Phys. Rev. Lett. **118**, 036801 (2017).

[196] J. Bardeen, Phys. Rev. Lett. **6**, 57 (1961).

[197] S. H. John W. Eaton, David Bateman and R. Wehbring, *GNU Octave version 4.0.0 manual: a high-level interactive language for numerical computations* (2015) http://www.gnu.org/software/octave/doc/interpreter.

[198] J. Hoffman-Jørgensen, *Probability with a view towards statistics*, Vol. 2 (Chapman and Hall / CRC, New York, 1994).

[199] D. Bates and D. Watts, *Nonlinear Regression Analysis and Its Applications*, Âğ2.3 (John Wiley & Sons, New York, 1988).